SOLID-STATE NMR STUDIES OF PROTON DYNAMICS IN NAFION / INORGANIC COMPOSITE MEMBRANES FOR FUEL CELL APPLICATIONS

SOLID-STATE NMR STUDIES OF PROTON DYNAMICS IN NAFION / INORGANIC COMPOSITE MEMBRANES FOR FUEL CELL APPLICATIONS

By

CHUAN-YU MA,

M.Sc., B.Sc.

A Thesis

Submitted to the School of Graduate Studies

in Partial Fulfillment of the Requirements

for the Degree

Master of Science

McMaster University

MASTER OF SCIENCE (2010) McMaster University
(Department of Chemistry) Hamilton, Ontario

TITLE: Solid-State NMR Studies of Proton Dynamics in Nafion / Inorganic Composite Membranes for Fuel Cell Applications

AUTHOR: Chuan-Yu Ma, M.Sc., B.Sc.

SUPERVISOR: Professor G.R. Goward

NUMBER OF PAGES: xvi, 119

ABSTRACT

The demand of energy is always increasing with continued growth of the human population. As mankind relies on oil as the main source of energy, which is finite and yet produces toxic by-products. The importance of alternative green energy sources cannot be underestimated. Fuel cells are an alternative source of green energy due to its high efficiency, without compromising the environment. In particular, polymer electrolyte membrane fuel cells (PEMFCs) are one of the most highly sought-after fuel cells as a result of their application in the automobile industry reduce exhaust emissions.

However, the life span and performance of PEMFCs are currently hampered by polymer degradation and high operating temperatures. In order to overcome these problems, various inorganic materials have been selected to be incorporated into the polymer electrolyte membrane. Nafion® is the polymer electrolyte investigated in this thesis.

This thesis documents the work involved in two separate projects with the common goals of enhancing overall Nafion performance: 1) doping of Nafion with Ce/ Mn oxides in order to improve Nafion durability and lifetime and 2) doping of Nafion with PWA to improve Nafion conductivity. Solid state NMR is the main technique used throughout the investigation of these studies.

ACKNOWLEDGEMENTS

First and foremost, I would like to express my sincerest gratitude to my supervisor, Dr. Gillian R. Goward, for her guidance throughout my learning journey. I knew that coming to Canada to pursue my second MSc degree as an international student, with English as my second language, would be a challenge, however, I did not foresee that it would end up being such a positive, rewarding and memorable experience. Dr. Goward, without your support, encouragement and advice, I would not be at this point in my life, where I am feeling confident of my abilities and ready to embark on the next chapter of my life in Canada. I am also very lucky to have had you as my supervisor, because not only did you show your enthusiasm and passion about conducting NMR and fuel cell research, but you were a supervisor who showed that you genuinely cared about your students just as much. From being a student of yours, I am fortunate to be one of those few international ESL students who can honestly say that their transition to studying and working in Canada was a smooth and pleasant one. Thank you, Dr. Goward, for accepting me as your student thereby allowing me to work with you, for having the faith in me and last but not least, for supporting and guiding me to the finish line.

Secondly, I would like to thank Dr. Gianluigi Botton and Dr. Peter Kruse for attending my committee meetings, allowing me to present my research to them, and most of all, for taking the time to understand my research in order to give me helpful advice, suggestions and constructive feedback. As well, I must thank the kind assistance of those whom I have met along the way, including Fred Pearson (TEM assistance), Dr. Steve

Koprich (SEM assistance) and NMR facility staff, including Dr. Bob Berno, Dr. Steve Kornic and the late Dr. Don Hughes.

Finally, I would like to thank all of my past and present group members - in particular I would like to thank Eric, Lindsay, Jason, Linda, Leigh, Nicole and Terry, for providing me with such a comfortable, friendly and supportive working atmosphere; and for contributing to stimulating group discussions in which you offered fresh ideas. Also, I would like to thank all of my friends both in Canada and outside of Canada for always listening and being my cheerleaders. Last but not least, I cannot even begin to thank my family, especially my parents and my brother– for their unconditional love for me, for being so supportive and proud of my endeavors, and for always being there for me, no matter what. To my girlfriend, Karen Lam, and her family, for taking care of me and making Canada my second home.

TABLE OF CONTENTS

Preliminaries **Page**

LIST OF FIGURES

Chapter 1

Chapter 2

Chapter 3

Chapter 4

LIST OF TABLES

Chapter 1

Chapter 3

Chapter 4

LIST OF ABBREVIATIONS AND SYMBOLS

Å	Angstrom
BaBa	Back-to-Back pulse sequence
EXSY	Exchange Spectroscopy
F	Faraday's constant
DQF	Double Quantum Filter
FID	Free induction decay
FTIR	Fourier Transform Infrared Spectroscopy
HPAs	Heteropolyacids
K	Kelvin (unit of temperature)
NMR	Nuclear magnetic resonance
MAS	Magic Angle Spinning
PWA	$H_3PW_{12}O_{40}$
SiWA	$H_4SiW_{12}O_{40}$
RF	Radiofrequency
SEM	Scanning Electron Microscope
SI	Selective Inversion
2D	Two Dimensions
Ω	Larmor frequency
TEOS	$Si(OC_2H_5)_4$
T_1	Longitudinal relaxation time
T_2	Transverse relaxation time

B_o	Static magnetic field
σ	Conductivity
s	Second
T	Temperature
ΔG	Gibbs free energy

Chapter 1

Introduction

This chapter is a brief survey of fuel cells, as well as the progress and development of the proton exchange membrane (PEM). This chapter concludes with a description of the goals for this thesis and the significance of the work to extend the lifetime of proton exchange membranes and maintain sufficient proton conductivity under anhydrous fuel cell operational environment.

1.1 Fuel Cells

Today, the global environment and shortage of fossil fuels are of great concern. Establishing cost effective green energy sources is becoming a more significant challenge for humankind. Hydrogen fuel cells are considered to be a prospective source of green energy because they are able to generate electricity with high efficiency, no pollutants, quiet operation and reliability.

The fuel cell is an electrochemical device, which turns chemical energy of the fuel to electricity. The principles of fuel cell were discovered in 1839 by Sir William Grove [1]. However, it took nearly a century to create the first practical fuel cell which was developed by Francis T, Bacon in the 1950's at Cambridge University. The US space program provided an opportunity to apply the first fuel cells. The fuel cell was installed in the

Apollo spacecraft to provide both electricity and drinking water for the astronauts during their mission. After the 1960's, fuel cells were introduced into the automobile industry by General Motors and Ballard Power Systems [1].

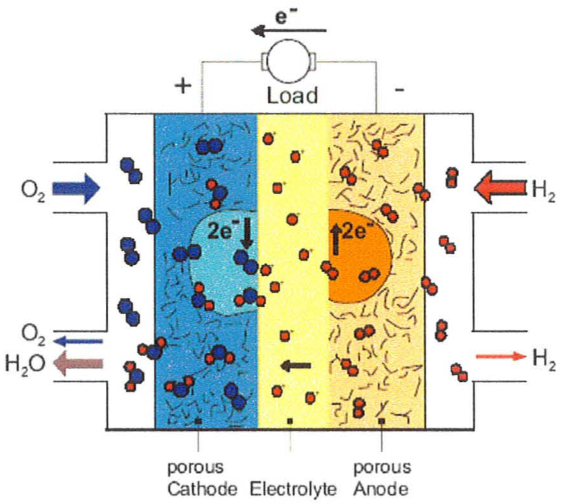

Figure 1-1. Schematic detailing the operating process of hydrogen fuel cell [2]

The difference between traditional chemical batteries and fuel cells is that the fuel and oxidant is not stored in the fuel cell itself. The continuous supply of hydrogen and oxygen from the external container is necessary. For instance, polymer electrolyte membrane fuel cells (PEMFCs) use hydrogen as the fuel at the anode and oxygen as the oxidizing reagent at the cathode to generate power, with water and heat. When hydrogen diffuses to the anode catalyst, the hydrogen is oxidized. The result of this reaction causes hydrogen to lose two electrons, thereby becoming 2 H^+.

This oxidation half-cell reaction is represented as:

$$H_2 \rightarrow 2H^{+} + e^{-} \qquad \text{(Eq. 1-1)}$$

The protons will pass through the ion-exchange membrane to the cathode, while the electrons will travel through the external circuit, thus providing electricity. After the electrons reach the cathode catalyst, the electrons react with protons (2 H^{+}) and the supplied oxygen to form water. This reduction half-cell reaction is represented as:

$$\tfrac{1}{2} O_2 + 2H^{+} + 2e^{-} \rightarrow H_2O \qquad \text{(Eq. 1-2)}$$

Water is the only product of fuel cell operation. However, traditional combustion engines produce different types of exhaust including nitrous oxide (N_2O), carbon oxide (CO_2) and hydrocarbons (C_xH_y). These gases are of environmental concern. Although replacing internal combustion engines with fuel cells will reduce total poisonous emissions from vehicles, finding sources of energy to create and store H_2 still remains a problem.

Nowadays, the internal combustion engines dominate the automobile engine market. Compared to internal combustion engines, fuel cells convert chemical energy to electricity directly with higher energy conversion efficiency. The theoretical fuel cell efficiency is 83%. However, it is impossible to achieve 83% fuel cell efficiency due to electrolyte resistance, reduction of [H_2] and [O_2], fuel (hydrogen) crossover and activation loss [1]. The theoretical potential of fuel cell is calculated as 1.23 V at 25°C, according to Eq. 1-3, where ΔG is the Gibbs free energy with a value of 237.34 J/mol, n is number of electrons with a value of 2 and F is Faraday's constant, with a value of 96485 Coulombs/ electron-mol.

$$E = \frac{-\Delta G}{nF} = 1.23 Volts \qquad \text{(Eq. 1-3)}$$

1.2 Types of Fuel Cells

In general, fuel cells are classified into six different types, which are based on the type of electrolyte that is being used: Alkaline Fuel Cell (AFC), Polymer Electrolyte membrane Fuel Cell (PEMFC), Phosphoric Acid Fuel Cell (PAFC), Molten Carbonate Fuel Cell (MCFC), Direct Methanol Fuel Cell (DMFC) and Solid Oxide Fuel Cell (SOFC). Their features are listed in Table 1-1 and Figure 1-2.

Table 1-1. Comparison of different types of fuel cells [3, 4]

	MCFC	SOFC	PEMFC	DMFC	PAFC	AFC
Electrolyte	LiK/LiNa carbonate	Ceramic(ZrO_2, CeO_2)	Polymer membrane	Polymer membrane	Liquid H_3PO_4	Liquid KOH
Charge carrier	CO_3^{2-}	O^{2-}	H^+	H^+	H^+	OH^-
Catalyst	Nickel	Perovshites	Platinum	Platinum	Platinum	Platinum
Operating Temperature	600-800 °C	600-1000 °C	60-120 °C	60-120 °C	200 °C	60-220 °C
Fuel	H_2, CH_4	H_2, CH_4,CO	H_2	CH_3OH	H_2	H_2

PEMFC may be the most studied and investigated fuel cell system because of its versatility in different applications (eg. transportation and energy storage systems). It has a high power to weight ratio and short start-up time, which satisfies the requirements for automotive applications. In 1993, Energy Partners developed the first passenger car, which was run by PEMFC [5].

Due to the aforementioned advantages, the focus of this thesis is the membrane of PEMFCs. The proton exchange membrane plays a critical role as the electrolyte in these particular fuel cells and thus warrants detailed characterization. Polystyrene sulfonate (PSS) was used as a membrane electrolyte for PEMFCs in the Gemini space program. However, this type of electrolyte is not stable and membrane degradation is known to occur, thereby contaminating the drinking water supply of the spacecraft and limiting the lifetime of the fuel cells to a few hundred hours. For this reason, the PEMFCs were substituted by AFCs until the chemical company, Dupont, invented the Nafion® membrane (Perfluorosulfonic Acid) in the 1970's, bringing PEMFCs back to the fuel cell industry [2]. Owing to the great success of Nafion applications, other companies such as Dow, Gore, Asahi Chemicals and Asahi Glass have developed other perfluorocarbon sulfonic membranes (Dow®, Gore-select®, Flemion® and Aciplex®, respectively) [6], with the main difference between them being the length of the side chain. This thesis will focus on Nafion® in particular and its optimization.

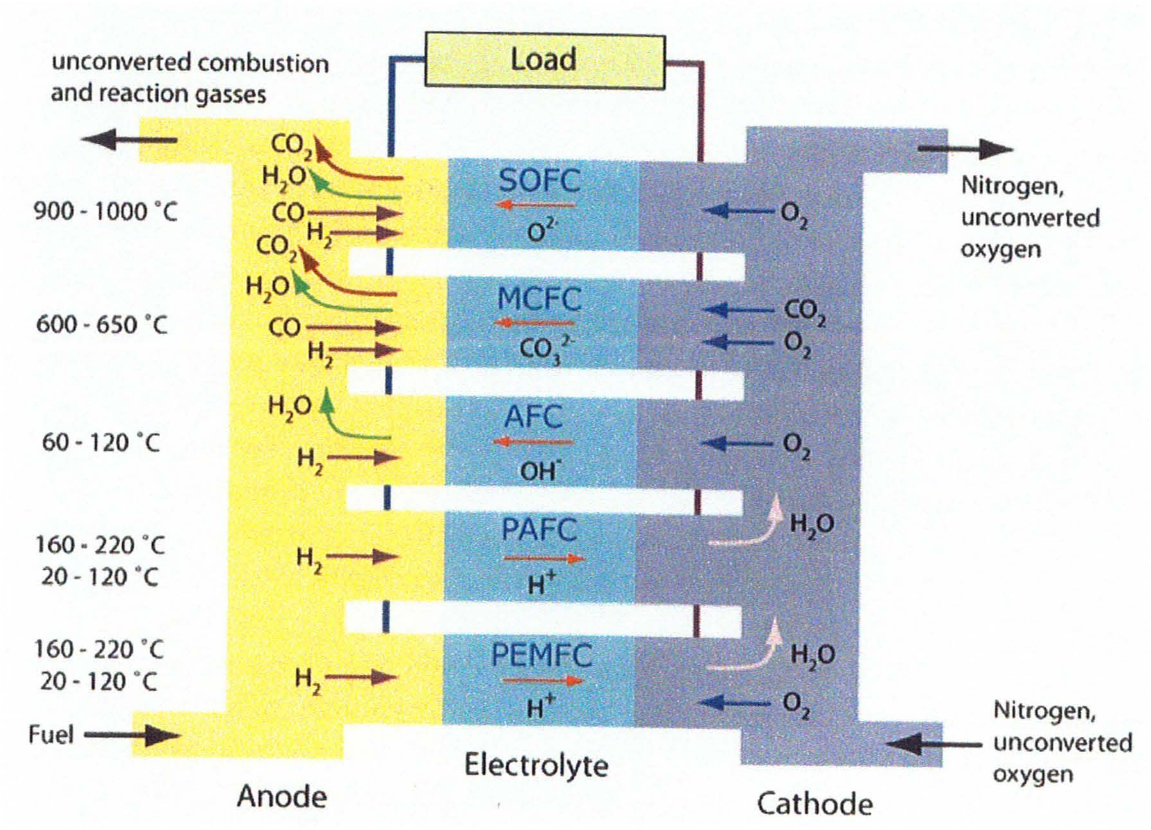

Figure 1-2. Different types of fuel cells [7].

1.3 Polymer electrolyte

Nafion®, the most prevalent ion exchange membrane, has been studied extensively by many authors since its discovery in the 1970s. It was initially made as a membrane for chlor-alkali cells [8]. More recently, it has been adapted as an electrolyte membrane for hydrogen fuel cells.

The rigid perfluorinated backbone of Nafion® imparts the thermal, physical and chemical stability to the Nafion®, while the proton at the sulfonic acid group (SO_3H)

contributes to high proton conductivity (0.1 Scm^{-1}). This is achieved by the protons moving through the abundant sulfonic acid groups along the main chain under high levels of hydration at a temperature range of 30-90°C. The backbone (CF_2-CF-CF_2) is strongly hydrophobic while the sulfonic acid (SO_3^-) found at the end of the side chain is hydrophilic. Figure 1-3 shows the structure of Nafion®.

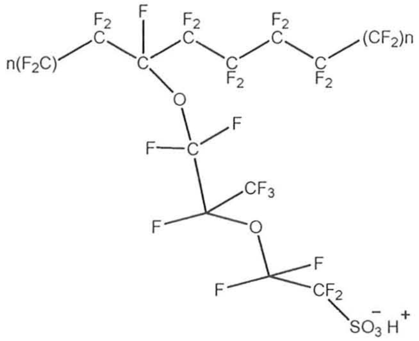

Figure 1-3. Structure of Nafion®

Due to the morphology of the hydrophilic region, large amounts of water can be absorbed into the hydrated Nafion® by the SO_3H cluster. The water content (λ) in the membrane is usually expressed as the number of water molecules per sulfonic acid group:

$$\lambda = \text{\# of } H_2O \text{ molecules / \# of } SO_3H \text{ molecules} \qquad \text{(Eq.1- 4)}$$

A Nafion® membrane saturated by liquid water can absorb 22 water molecules per sulfonate group, while a Nafion® membrane saturated by water vapor absorbs only 14 water molecules. The water uptake of membrane dramatically decreases when Nafion® is dried at 105 °C, compared to drying under room temperature conditions. In a fully hydrated membrane ($\lambda > 14$), water channels are formed automatically in the pores of Nafion®.

Hydronium ions can then migrate freely in the built-in water channels in Figure 1-4. This form of proton migration, via the movement of hydronium ions, occurs through what is referred to as the vehicle mechanism [9]. Therefore, the proton mobility of a fully hydrated membrane is one order of magnitude lower than that of sulfuric acid solution. When λ is equal to 22, the conductivity is 0.1 Scm^{-1}. But when λ drops to 14, the conductivity decreases to 0.06 Scm^{-1} [1].

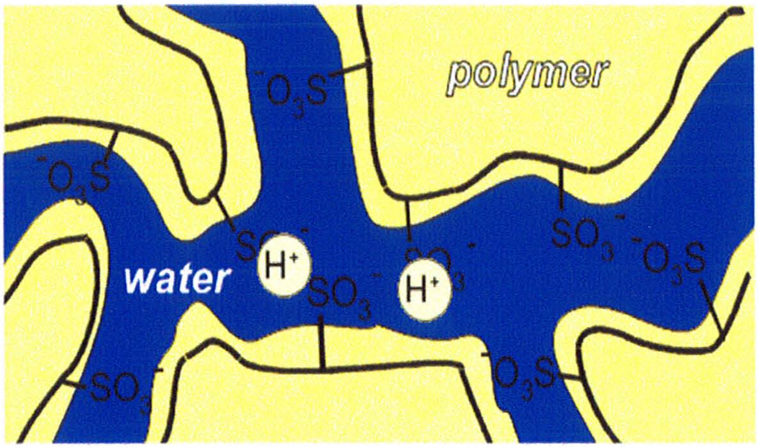

Figure 1-4. Schematic of water channels present in Nafion [1]

This demostrates that the proton conductivity is proportional to the amount of water uptake of Nafion®, which is also seen in the data in Figure 1-5.

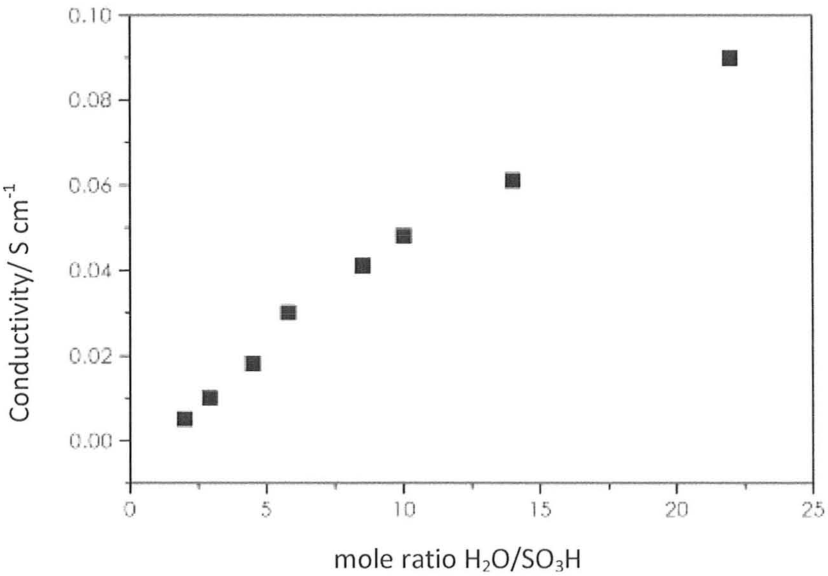

Fig 1-5 The influence of water content on the conductivity of Nafion [2]

1.4 Nafion® Degradation

Fuel cells are not yet fully commercialized due to obstacles of durability, temperature/ relative humanity dependence and cost. For example, the durability of Nafion® currently imposes a strong restriction on the maximum working hours of the fuel cell. The durability of Nafion® is compromised by hydrogen peroxide, which is formed during fuel cell operation [10-12]. Secondly, proton conductivity of Nafion® is strongly dependent on Nafion® water uptake. Hydrated Nafion® obtains high conductivity (ie. 0.1 S/ cm) while that of anhydrous Nafion® dramatically drops to 1x 10^{-6} S/cm [13].

Aside from Nafion® being an electrolyte, it functions as a gas separator. A gas separator helps to keep H_2 at the anode and O_2 at the cathode. However, it is not 100% effective. Fuel (H_2) crossover can occur which leads to loss of the fuel without electrons being released, thereby decreasing the efficiency of the fuel cell. Hydrogen crossover means hydrogen gas traverses the membrane without being oxidized at the anode.

The loss of performance in PEMFCs during extended operation is attributed to thermal, mechanical and chemical degradation of Nafion®. It is believed that this chemical degradation is mainly caused by the formation of hydrogen peroxide within the PEMFC, motivating a search for means to remove this reactive species.

1.4.1 Sources of Chemical Degradation

Formation of hydrogen peroxide has been detected in an operating fuel cell and in the outlet stream [11,14]. Due to the degree of permeability of Nafion® to H_2, there is hydrogen crossover within the cell. For example, hydrogen gas across membrane electrode Asssemble (MEA) with Nafion® 111 is 1.61×10^{-8}mol $(cm^2s)^{-1}$. When molecular hydrogen gas from the anode crosses over and reacts with the platinum catalyst at the cathode, two protons are produced at the cathode:

$$H_2 \text{ (Pt catalyst)} \rightarrow 2\,H^+ \qquad \text{(Eq. 1-5)}$$

Secondly, upon incomplete reduction of oxygen at the cathode, hydrogen peroxide is produced as a side product:

$$2H^+ + O_2 + 2e^- \rightarrow H_2O_2 \qquad \text{(Eq. 1-6)}$$

Hydrogen peroxide then decomposes into the hydroxyl (HO•) and peroxyl (HOO•) radical species. This decomposition of hydrogen peroxide is catalyzed by the existence of certain metal ions (iron, copper and titanium), as demonstrated by T. Kinumoto and L. Merlo [15, 16]. Of these catalytic ions, iron ions have been discovered on the fuel cell end plate [17].

The formation of free radicals inevitably leads to the decomposition of the Nafion® membrane. The reactive oxygen species (ROS) include both the hydroxyl (HO•) and hydroperoxyl (HOO•) radicals, and H_2O_2. All ROS induce damage to Nafion® but at different levels of degradation. The hydroxyl radical has a very short lifetime as it also reacts with H_2O_2, thereby converting it to the less destructive hydroperoxyl radical (3.3×10^7 $M^{-1}s^{-1}$). Moreover, the reduction potential for the hydroxyl half cell reaction,

$$HO\bullet + H^+ + e^- \rightarrow H_2O \qquad E_{red}=2.59\ V \qquad \text{(Eq. 1-7)}$$

is the highest of the three ROS at 2.59 V, and therefore, it is the most likely to react in the Nafion® side chain and backbone upon formation of the hydroxyl radical [18] .

Another radical is peroxyl radical, which is less aggressive than the hydroxyl radical, because its reduction potential for the half cell reaction

$$HOO\bullet + H^+ + e^- \rightarrow H_2O \qquad E_{red}=1.48\ V \qquad \text{(Eq. 1-8)}$$

is only 1.48 V. Nafion® degradation can also be triggered by existence of H_2O_2 itself, since H_2O_2 has a strong oxidation ability [19]:

$$H_2O_2 + 2H^+ + 2e \rightarrow 2H_2O \qquad E_{red}=1.77\ V \qquad \text{(Eq. 1-9)}$$

Since the hydroxyl radical is the most aggressive oxidant out of the three ROS and is the primary cause of Nafion® degradation, the present work aims to mitigate Nafion® degradation from hydroxyl radical attack.

1.4.2 Mechanism of Chemical Degradation

Nafion® degradation may be determined by different techniques, including X-ray diffraction (XRD), X -Ray Photoelectron Spectroscopy (XPS) [20] , Fourier Transform Infrared Spectroscopy (FTIR) [15, 21, 22], ion chromatograohy [21, 23], Electron Spin Resonance (ESR) [23], and fluoride ion selective electrode [24]. So far, three different mechanisms of degradation have been proposed and are described below.

1.4.2.1 Unzipping Reaction

The unzipping reaction [25] is considered to be the main Nafion® degradation mechanism. It starts at the end group (carboxylic group) of the backbone. This type of end group is formed during the polymer manufacturing process. Hydroxyl radicals are very powerful radicals so the rate of hydrogen atom abstraction by hydroxyl radical from the carboxylic group is very rapid. In the process of Nafion® degradation, RCOOH is formed as a by-product.

$$R\text{-}CF_2COOH + HO\bullet \rightarrow RCF_2\bullet + CO_2 + H_2O\ (k=1.0\times10^{6}\ M^{-1}s^{-1}) \quad \text{(Eq. 1-10)}$$

$$RCF_2\bullet + HO\bullet \rightarrow RCF_2OH \rightarrow RCOF + HF \quad \text{(Eq. 1-11)}$$

$$R\text{-}COF + H_2O \rightarrow RCOOH\ (\text{by-product}) + HF \quad \text{(Eq.1-12)}$$

In 2006, Healy and Zhoug confirmed the structure of the by-product (Fig. 1-6) using ^{19}F solution state NMR and mass spectrometry [17]. Unzipping from the carboxylic acid end group is more than 500 times faster than both the degradation mechanisms resulting from free radical cleavage at ether groups and the scission of main chains [26]. This had motivated Dupont to manufacture a new Nafion polymer, in which COOH is replaced by CF_3 [25]. Unfortunately, this material is yet more costly than the original Nafion itself.

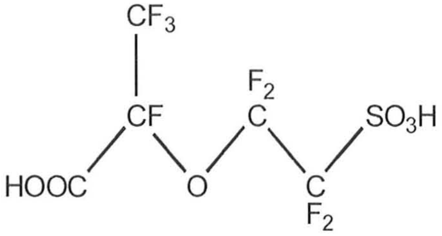

Fig 1-6. By-product of Nafion degradation

1.4.2.2 Free radical cleavage at ether groups and scission of main chains [27]

Solid state NMR has been introduced to study Nafion® structure before and after fuel cell durability tests [28]. ^{19}F and ^{13}C spectra of Nafion® have been assigned based on the results of Chen and Schmidt [29]. Each resonance from the ^{19}F spectrum represents a different fluorine environment. For example, the ^{19}F NMR resonance at -144 ppm was assigned to the side chain $R\text{-}OCF_3C\underline{F}CF_3\text{-}(CF_2)_2\text{-}SO_3H$ and the resonance at -138 ppm was assigned to the main chain $CF_2\text{-}C\underline{F}(CF_2\text{-}CF_2)_{6.5}$ $-OC_5O_2F_{10}SO_3H$. Ghassemzadeh *et al.*[28] found that the intensities of the side chain resonances in both ^{19}F and ^{13}C spectra decrease following durability tests. The resonance intensity at -144 ppm (side chain) reduces while that at -138 ppm (main chain) remains at the same level after durability tests. This indicates that degradation takes place at the side chains and is clear evidence that free radical cleavage at the ether groups occur. The degradation of Nafion® may also occur when the radical species attack the C-C bond ($CF_2\text{-}CF_2$) at the backbone [21].

Ultimately, the consequence of Nafion® degradation is the failure of the fuel cell. The membrane from the cathode becomes thinner after degradation, as shown by scanning electron microscopy (SEM) [30] and confirmed in our own work in Figure 1-7 and Figure 1-8. In some serious cases, pinholes are formed, as can be seen in Fig. 1-8. The presence of pinholes accelerates the H_2 and O_2 crossover rate, and exacerbates Nafion® degradation. Thus, it is crucial to investigate methods that may help in slowing down or inhibiting Nafion® degradation.

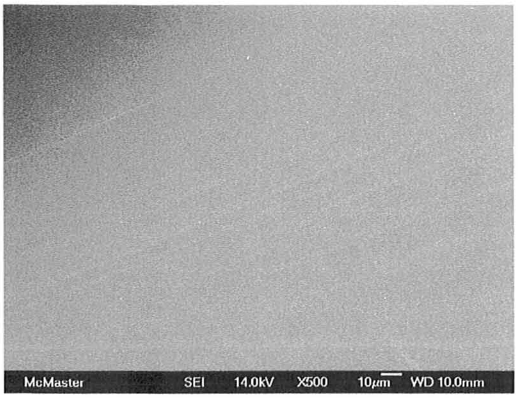

Fig 1-7. A scanning electron micrograph (SEM) of fresh Nafion (500x magnification)

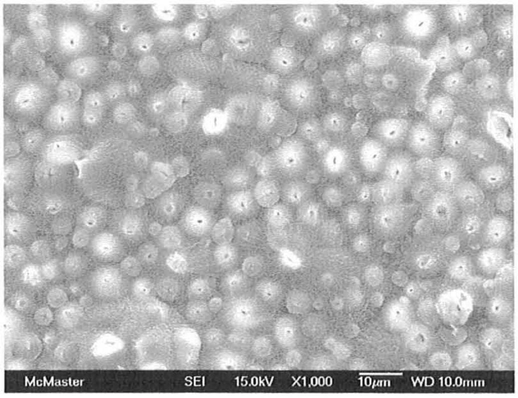

Fig 1-8. SEM of Nafion following 3-day free radical attack (1000x magnification)

1.4.3 Solution to Nafion® Degradation

More than 6000 hours for operation time in vehicle applications is needed. In order to enhance the stability and durability of Nafion® and to further commercialize PEMFC, the issue of radical attack on the Nafion® needs to be resolved. There are several patents [31-33] that suggest that additives (eg. manganese oxide, cerium oxide and platinum metal) may be radical scavengers that work by reducing the amount of free radicals as well as the hydrogen peroxide decomposition catalyst. In cases where formation of H_2O_2 is inevitable, an additional transition metal is used to deactivate the radical. Danilczuk *et al.*[34] have shown that a Nafion® based membrane electrode assembly (MEA), neutralized by 10% Ce^{3+}, has good stabilization. In their research, electron spin resonance (ESR) was used to detect different types of radical fragments (hydroxyl (HO•), hydroperoxyl (HOO•) and carbon centered radical (•CCR)) responsible for Nafion® degradation. The hydroxyl radicals were generated by UV irradiation of hydrogen peroxide solution and were subsequently trapped by 5,5-dimenthyl-pyrroline-N-oxide (DMPO) to form DPMO/OH adducts, which were detected by ESR. The absence of HO• and •CCR and the presence of HOO• prove that Ce^{3+} from the processed Nafion® react with HO• to form less aggressive HOO•. The HOO• is not able to degrade Nafion® to generate •CCR [35]. Trogdas *et al.* reported that Nafion®ceria composite membrane possesses better durability than pure Nafion® by Fluoride emission rate (FER) measurements [36]. The former membrane can mitigate the degradation rate by more than an order of magnitude. The MnO_2 is also found to be a qualified hydrogen peroxide scavenger by Zhao *et al* [37]. These and other studies to date, have shown promising results, but with minimal detail regarding mechanism, and optimization strategies [36].

1.5 Operation Fuel Cell Under Low-Humidity Conditions

Another main challenge preventing the commercialization of fuel cells is the high operating temperature requirement of fuel cells, which results in poor performance of the electrolyte conductor. The reason to operate fuel cells at high temperature is to avoid CO poisoning. When fuel cells run at low temperatures, the use of high-purity hydrogen is essential, since low amounts (20 ppm) of CO present as trace impurities is sufficient to cause deactivation of the Pt catalyst [38]. In this case, greater than 100 °C is considered high temperature. However, due to the loss of humidity at high temperatures, proton conductivity of the polymer membrane drops dramatically. In anhydrous conditions, proton transport in the membrane is based on the Grotthuss mechanism [39], which involves the simultaneous formation and cleavage of hydrogen bonds between water molecules and hydronium ions [40, 41].

The water channels in the hydrated membrane disappear due to the evaporation of water. Furthermore, there is no molecular vehicle to diffuse the protons in the anhydrous membrane. Instead, protons have to hop to the nearest site to contribute proton conductivity. Additionally, the sizes of the water clusters shrink causing the gap to enlarge between adjoining clusters, thereby making the proton-hopping between adjacent sites more difficult. Thus, higher activation energies are required to complete the proton transportation while the vehicular mechanism needs relatively low activation energies. The activation energy of the Grotthuss mechanism mainly depends on the distance between sites and the number of protonic carriers.

The two common methods to maintain high conductivity for Nafion are explained as below. Metal oxides such as SiO_2 , TiO_2, ZrO_2, and WO_3 have been used to form membrane composites to retain water in Nafion at over 100 °C [42-44]. Due to the existence of water in the Nafion, protons can move freely to achieve high conductivity at high temperatures. Another common strategy to maintain desired conductivity at high temperatures is using inorganic membrane composites to replace pure Nafion® in fuel cells [44, 45]. Heteropolyacids includes phosphotungstic (PWA), silicotungstic acid (SiWA) and phosphomolybdic acid (PMA), which have been used to prepare Nafion composites to enhance Nafion conductivity [46-48]. The selected inorganic materials in this research are silica and heteropolyacids (HPA).

1.5.1 Heteropolyacids

Heteropoloyacids (HPA) are a class of inorganic proton conducting materials, possessing high proton conductivity at room temperature. Heteropolyacids, such as 12-tungstophosphoric (PWA) and 12-tungstosilicic acid (SiWA), are strong Bronsted acids and have been widely used in acid-catalyzed reactions. Recently, there is much emphasis on utilizing heteropoly acids as catalysts in fuel cell applications. HPAs have been considered as candidate particle electrolytes in high temperature fuel cells due to their thermal stability and high proton conductivity [49]. Furthermore, HPAs possess multiple proton sites that act as good proton donors. For instance, PWA and SiWA possess 3 and 4 protons, respectively.

HPAs possess super acid properties, meaning that their protons are easily dissociated. These delocalized protons stay on the surface of PWA particles, linking with bridge or terminal oxygen, which is the reason why HPAs provide good proton conductivity [50]. The most common heteropoly acids used in fuel cells are silicotungstic acid (SiWA), and phosphotungstic acid ($H_3W_{12}O_4 \cdot XH_2O$, PWA) – the latter which will be the main focus of this thesis work. PWA has high protonic conductivity at room temperature (0.02-0.1 S/cm) and possesses electrochromic and photochromic properties [51]. In addition, Staiti *et al* found out that Phosphotungstic acid-base Nafion® membrane exhibits better proton conductivity than silicotungstic ($H_4SiW_{12}O_{40}$), acid-base Nafion® membrane and pure Nafion® [46, 48], even though silicotungstic provides an additional proton. Based on these results, the focus of this thesis is on PWA-Nafion® composites.

PWA is the strongest acid out of all Keggin-type HPAs, whether in solution-state or solid-state [52]. Keggin-type HPAs refer to those HPAs whose structure consists of a central XO_4 tetrahedron (X= P or Si) surrounded by 12 MO_6 (M= Mo^{6+} or W^{6+}) groups linked together through oxygen atoms. There are four different types of oxygen atoms present in Keggin ions. The central oxygen is located between X-O_C-M. The edge-sharing oxygen atom bridges two tungsten of the same set M-O_b-M. The corner-sharing oxygen atom bridges two tungsten of the different set M-O_c-M. The terminal oxygen atom is associated with only one tungsten atom M=O. The last three types of oxygen are located on the surface of the structure. In solution, the bridging oxygen atoms have higher electron density than the terminal oxygen atoms. Therefore, these oxygen atoms have a greater affinity for protons and water, thus forming hydrates. The $H_5O_2^+$ is created when the H^+ is associated with two water molecules between two Keggin units [53]. One advantage stemming from this property is the ability of HPAs to absorb large quantities of water. The level of hydration is a dominant factor in influencing HPA conductivity. Fully hydrated HPAs (with 29 - 30 H_2O / Keggin structure unit) can even provide excellent conductivity up to 0.17 S/cm [54]. Furthermore, these structures are capable of being stable at temperatures up to 400 °C [51].

A host material is necessary to hold an HPA electrolyte and prevent its complete dissolution in water. Without a host material, the high solubility of HPAs in polar solution becomes a limitation in fuel cell operation [55]. Electrochemically produced water will tend to dissolve HPAs and, which will then leak out through the gas outlet lowering the lifetime of HPA fuel cells. Several papers have been published which discuss this issue [56]. A key point to overcome this drawback is using an adequately supported matrix. However, choice of an appropriate host material must be made with caution. For example, some inorganic materials such as Al_2O_3 and MgO decompose the heteropoly acids [57]. Acidic and neutral host materials are most suitable. For example, silica and active carbon are generally good host materials that are compatible with heteropoly acids [57].

The interaction between PWA and the OH group from the SiO_2 surface has been detected at low loading level by ^{1}H NMR [59]. The interaction between the Keggin units and the supported material occurs through the hydrogen atom. Staiti *et al.* [48] have shown that the Keggin unit of PWA interacts with silica most likely through the bridge-shared oxygen (M-O_b-M) – a finding that has been supported by quantum chemical calculations [59] and NMR analysis [60]. This interaction suggests that HPAs can be incorporated with inorganic material to prevent its dissolution in aqueous media. The stability of this compound incorporated into supported matrix (silica) is crucial to preserve its multifunctional properties in the membrane. Furthermore, Stangar *et al* [51] discovered that using isocyanatopropyl-triethoxysilane-poly(propylene glycol) -(ICS-PPG) as a host matrix is able to increase PWA/ SiWA uptake to 70 wt % as a result of electrostatic interactions between positively and negatively charged Keggin ions [51, 59].

The focus of this research is to use heteropoly acids as proton donors to bridge SO_3H groups of Nafion® in order to increase Nafion®'s proton conductivity under relatively low humidity fuel cell operation environments. Characterization of the structure and dynamic features of this composite will be accomplished using solid state NMR.

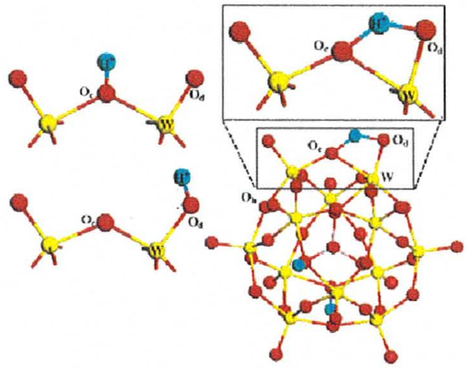

Fig 1-9 Keggin structure of PWA. [61]

1.6 Goals of Thesis

To summarize, the main goals of the first project in this thesis are to use NMR to understand the local proton mobility at the molecular level and determine the level of protection that metal oxide additives can provide to the Nafion composite as radical scavengers. As the additives are not good ionic conductors, the amount of additives in the Nafion composite are kept at low levels in order to maintain the excellent proton conductivity of Nafion. These Nafion composites are studied by variable temperature ^{1}H NMR experiments which provide dynamic information and allow for the investigation of local proton environments before and after exposure to free radicals. However, since this piece of information is usually absent in the literature, this thesis documents a first-time investigation of the dynamics of proton transport following exposure to free radicals, which is highly significant since proton dynamics are known to be strongly correlated to overall fuel cell performance. Moreover, solution-state ^{19}F NMR is used to identify and quantify Nafion® degradation by-products as a function of preparative method, particle size, protective agent, oxidation state and Nafion® morphology, in order to allow for the screening of potential radical scavengers. The combination of information obtained from both variable temperature ^{1}H MAS NMR and solution-state ^{19}F NMR experiments reveal which additives function as the best radical scavenger, while having minimal negative impact on Nafion proton conductivity.

The main goals of the second project in this thesis are to introduce PWA, a multiple-proton donor, into Nafion to increase the proton conductivity. ^{1}H MAS NMR is subsequently used to understand the local proton environment and proton mobility, as well as to determine the proton exchange mechanism. This is the first time that the proton exchange mechanism is studied for PWA-Nafion composites. Multiple mobile protons sites are expected to be present in Nafion-PWA composites. 2D-Exchange Spectroscopy (EXSY) is used to study the proton exchange. Furthermore, solution-state and solid-state ^{31}P NMR is used to identify the amount of PWA leaching out from Nafion® composites, as a function of preparation method, which has proven the inability of PWA to reside permanently in Nafion. Fourier Transform Infrared Spectroscopy is used as an alternate confirmatory technique to measure changes in the amount of PWA in the Nafion composites pre- and post- Nafion-purification procedures.

1.7 References

1. F. Barbir., PEM Fuel Cells: Theory and Practice. 2005: Elsevier Academic Press.

2. L.P.L. Carrette, F.K., Huber M, Stimming U Fuel Cells Fundamentals and application. Fuel cells, 2001. 1(1): p. 5.

3. K.D. Kreuer, in Handbook of Fuel Cell Fundamentals, Technology, and Applications;. Vol. 3. 2003, Chichester. UK: John Wiley

4. R.P. O'hayre, S.W.C., W. Colella, F.B Prinz, Fuel Cell Fundamentals 2006, New York: John Wiley 11.

5. M. Nadal, F.B., Development of Hybride Fuel cell/ Battery Powered Electric Vehicle, in Hydrogen Energy Progress X, T.N.v. D.L Block, Editor. 1994: Coral Gables,FL. p. 1427.

6. M. Wakizoe, O.A.V., S. Srinivasan, Electrochimica Acta, 1995. 40: p. 335.

7. N. Rajalakshmi, K.S.D., Present Trends in Fuel Cell Technology Development, in Progress IN FUEL CELL RESEARCH, P.V. Alemo, Editor. 2007, Nova Science Publishers, Inc: New York. p. 58.

8. Gort, Perfluorinated cation exchange polymers. Chemie-Ing.-Techn, 1975. MS260/75.

9. K.D. Kreuer, A.R., W. Weppner, Amgrew. Chem. Intel. Ed. Engl.,, 1982. 21: p. 208.

10. K. Teranishi, K.K., S. Tsushima, S. Hirai, , Electrochem. Solid-State Lett., 2006. 9: p. A475.

11. W.Liu, D.Z., In situ detection of hydrogen peroxide in PEM fuel cells. Journal of the Electrochemical Society, 2005. 152(6): p. A1165.

12. M. Inaba, T.K., M. Kiriake, R. Umebayashi, A. Tasaka, Z. Ogumi, , 2006. Electrochimica Acta. 51: p. 5746.

13. J. J. Sumner, S.E.C., J. J. Ma D. D. DesMarteau Proton Conductivity in Nation117 and in a Novel Bis[(perfluoroalkyl)sulfonyl]imide Ionomer Membrane. J of Electrochemical Society, 1998. 145: p. 107.

14. G.G. Scherer, Polymer Membranes for Fuel-Cells. Berichte Der Bunsen-Gesellschaft-Physical Chemistry Chemical Physics, 1990. 94(9): p. 1008.

15. T. Kinumoto, et al., Durability of perfluorinated ionomer membrane against hydrogen peroxide. Journal of Power Sources, 2006. 158(2): p. 1222.

16. L. Merlo, et al., Resistance to peroxide degradation of Hyflono (R) Ion membranes. Journal of Power Sources, 2007. 171: p. 140-147.

17. J. Healy, et al., Aspects of the chemical degradation of PFSA ionomers used in PEM fuel cells. Fuel Cells, 2005. 5(2): p. 302-308.

18. Coms, F.D., The Chemistry of Fuel Cell Membrane Chemical Degradation ECS Transactions, 2008. 16(2): p. 235-255.

19. F. D. Coms, H.L., Jeanette E. Owejan, Mitigation of Perfluorosulfonic Acid Membrane Chemical Degradation Using Cerium and Manganese Ions ECS Transactions, 2008. 16 (2): p. 1735-1747.

20. C.D. Huang, et al., XRD and XPS analysis of the degradation of the polymer electrolyte in H_2-O_2 fuel cell. Chemical Physics Letters, 2003. 371(1-2): p. 80-85.

21. S. Hommura, et al., Development of a method for clarifying the perfluorosulfonated membrane degradation mechanism in a fuel cell environment. Journal of the Electrochemical Society, 2008. 155: p. A29-A33.

22. W.E Liu, D.W., Use of FTIR to Analyze Ex-Situ and In-Situ Degradation of Perfluorinated Fuel Cell Ionomers ECS Transactions, 2007. 11 p. 1093.

23. M. Aoki, H. Uchida, and M. Watanabe, Novel evaluation method for degradation rate of polymer electrolytes in fuel cells. Electrochemistry Communications, 2005. 7(12): p. 1434-1438.

24. L. Pozio, A.S., R. F.De Francesco, M.Giorgi, Nafion degradation in PEFCs from end plate iron contamination. Electrochimica Acta, 2003. 48(11): p. 1543-1549.

25. D.E. Curtin, et al., Advanced materials for improved PEMFC performance and life. Journal of Power Sources, 2004. 131(1-2): p. 41-48.

26. C. M. Zhou, A.G., Z. M. Qiu, T. A. Zawodzinski, D. A. Schiraldi, , Chemical durability studies of perfluorinated sulfonic acid polymers and model compounds under mimic fuel cell conditions. Macromolecules, 2007. 40: p. 8695-8707.

27. D.A. Stevens, et al., Ex situ and in situ stability studies of PEMFC catalysts. Journal of the Electrochemical Society, 2005. 152(12): p. A2309-A2315.

28. L. Ghassemzadeh, M.M., R.Barrera, K.D. Kreuer, J. Maie, K. Müllerb, Chemical degradation of proton conducting perflurosulfonic acid ionomer membranes studied by solid-state nuclear magnetic resonance spectroscopy. Journal of Power Sources 2009. 186: p. 334-338.

29. Q. Chen, K. Schmidt-Rohr, F-19 and C-13 NMR signal assignment and analysis in a perfluorinated ionomer (Nafion) by two-dimensional solid-state NMR. Macromolecules, 2004. 37(16): p. 5995-6003.

30. S. Kundu, Development and Application of a Chemical Degradation Model for Reinforced Electrolyte Menbranes in Polymer Electrolyte Membrane Fuel Cells, in Chemical Enginnering. 2008, Waterloo University Waterloo,ON Canada.

31. N.R.Andrews, S.D.K., K.A. Murray, S.J. Mcdermid,S.M. Mackinnon, S. Ye,, Reduced Degradation of ion-Exchange Membranes in Electrochemical Fuel Cells, B.P.S. Inc, Editor. 2003.

32. H. Kawazoe, Liquid composition. Method for producing same, and method for producing a membrane electrode assembly for a solid polymer fuel cell, A.G. company, Editor. 2005: United States of America

33. G. Wakefield, et al., Metal Oxide Particles Useful As Free Radical Scavengers In Sunscreen And Cosmetic Compositions, O. LTD, Editor. 2005: UK.

34. M. Danilczuk, A.J. Perkowski, and S. Schlick, Ranking the Stability of Perfluorinated Membranes Used in Fuel Cells to Attack by Hydroxyl Radicals and the Effect of Ce(III): A Competitive Kinetics Approach Based on Spin Trapping ESR. Macromolecules, 2010. 43(7): p. 3352-3358.

35. M. Danilczuk, S. Schlick, and F.D. Coms, Cerium (III) as a Stabilizer of Perfluorinated Membranes Used in Fuel Cells: In Situ Detection of Early Events in the ESR Resonator. Macromolecules, 2009. 42(22): p. 8943-8949.

36. P. Trogadas, J. Parrondo, and V. Ramani, Degradation mitigation in polymer electrolyte membranes using cerium oxide as a regenerative free-radical scavenger. Electrochemical and Solid State Letters, 2008. 11(7): p. B113-B116.

37. D. Zhao, B.L.Y., H.M. Zhang, H.M.Yu, MnO_2/SiO_2-SO_3H nonocomposite as hydrogen peroxide scavenger for durability improvement in proton exchange membranes. Journal of Membrane Science, 2010. 346: p. 143-151.

38. H.F. Oetjen, V.M.S., U. Stimming, and F. Trila, Performance Data of a Proton Exchange Membrane Fuel Cell Using H_2/CO as Fuel Gas. J of Electrochemical Society, 1996. 143: p. 3838.

39. de Grotthuss, C.J.T., Sur la décomposition de l'eau et des corps qu'elle tient en dissolution à l'aide de l'électricité galvanique. Ann. Chim, 1806. 58: p. 54-73.

40. B. E. Conway, J.O.B., H. Linton,, J. Chem. Phys., 1956. 24: p. 834.

41. N. Agmon, Chem. Phys. Lett., 1995. 244: p. 456.

42. B.Mecheri, A.D.E., M.L.D. Vona, E. Tchicaya, G.Alberti, Journal of Electrochem Scoiety, 2006. 153: p. A463.

43. H. Wang, B.A.H., L. Hunag, Z. Wang, A. Mitra, J.M. Norbeck, Y. Yan, J.Mater. Chem, 2002. 12.

44. M. Watanabe, H.U., Y. Seki, M. Emori, P. Stonehart, J of Electrochemical Society, 1996. 143: p. 3847.

45. B. Tazi, O.S., J. New Mater. Electrochem. Syst., 2001. 4: p. 187.

46. P. Staiti, A.S.A., V. Baglio, F Lufrano, E Passalacqua, V. Antonucci, Hybrid Nafion-silica membranes doped with heteropolyacids for application in direct methanol fuel cells. Solid state Ionics, 2001. 145: p. 101-107.

47. P. Staiti, S. Freni, S. Hocevar, Synthesis and characterization of proton- conducting materials containg dodecatungstophosphoric and dodecatungstosilic acid supported on silca. Jounral of Power Sources, 1999. 79: p. 250-255.

48. P. Staiti, S. Hocevar, and N. Giordano, Fuel cells with $H_3PW_{12}O_{40}$ -29H_2O as solid electrolyte. International Journal of Hydrogen Energy, 1997. 22(8): p. 809-814.

49. U. Mioc, M.D., N. Tjapkin, Ph. Colomban, A. Novak, Solid State Ionics, 1991. 46: p. 103.

50. Y.S. Kim, F.W., M. Hickner, T.A. Zawodzinski, J.E. McGrath, , Fabrication and characterization of heteropolyacid ($H_3PW_{12}O_{40}$)/directly polymerized sulfonated poly(arylene ether sulfone) copolymer composite membranes for higher temperature fuel cell applications, Journal of Membrane Science, 2003. 212: p. 263.

51. U.L. Stangar, et al., Structure of and interactions between P/SiWA keggin nanocrystals dispersed in an organically modified electrolyte membrane. Chemistry of Materials, 2000. 12(12): p. 3745-3753.

52. I.V. Kozhevnikov., Russ. Chem. Rev, 1987. 56: p. 881.

53. G.M. Brown, M.-R.N.-S., W.R. Busing, H.A. Levt, Dodecatungstophosphoric acid hexahydrate, $(H_5O_2^+)_3(PW_{12}O_{40}^{3-})$. The true structure of Keggin's pentahydrate from single-crystal X-ray and neutron diffraction data. Acta Crystallographica Section B, 1977. 33: p. 1038.

54. O. Nakamura., T.K., I. Ogino., Y. Miyake., Chem Lett Chem Soc of Jap, 1979: p. 17.

55. Serguei D. Mikhailenko, S.K., John B. Moffat, Electrical impedance studies of the ammonium salt of 12-tungstophosphoric acid in the presence of liquid water. Solid state Ionics, 1999. 99(3-4): p. 281.

56. T.N. Nakanishi, et al., Studies on Microscopic Structure of Sol-Gel Derived Nanohybrids Containing Heteropolyacid. Macromolecules, 2007. 40: p. 4165.

57. I.V. Kozhevnikov, Catalysis by heteropoly acids and multicomponent polyoxometalates in liquid-phase reactions. Chemical Reviews, 1998. 98(1): p. 171-198.

58. V.M. Mastikhin, S.M.K., A.V. Nosov, I.V. Kozhevnikov, I.L. Mudrakovsky, M.N. Timofeeva, ^1H and ^{31}P MAS NMR studies of solid heteropolyaicds and $H_3PW_{12}O_{40}$ supported on SiO_2. Journal of Molecular Catalysis, 1990. 60: p. 65-70.

59. B.B. Bardin, et al., Acidity of Keggin-type heteropolycompounds evaluated by catalytic probe reactions, sorption microcalorimetry, and density functional quantum chemical calculations. Journal of Physical Chemistry B, 1998. 102(52): p. 10817-10825.

60. W.H. Knoth, R.L. Harlow, Derivatives of Heteropolyanions .3. O-Alkylation of $Mo_{12}PO_4$03- and $W_{12}PO_4$03. Journal of the American Chemical Society, 1981. 103(14): p. 4265-4266.

61. J. Michael, R.J.D.Janik, M. Neurock, Anhydrous and water Assisted Proton Mobility in Phosphotungstic Acid. Journal of the American Chemical Society, 2005. 127: p. 5238.

Chapter 2

Experimental Technique

This section describes the basic principles of the experimental methods used to investigate the polymer electrolyte membrane composites, which include NMR, SEM-EDS, FTIR and conductivity tests. In particular, the background relevant to the solid-state NMR experiments used in this thesis will be provided.

2.1 Application of solid-state nuclear magnetic resonance on materials

Structural information and proton dynamics are of significance when studying polymer electrolyte membrane composites. Small-angle X-ray scattering (SAXS) and wide-angle x-ray diffraction had been used to investigate the morphology of Nafion in the 1980`s by Gierke and co-workers, who had proposed the cluster network model to explain the morphology of hydrated Nafion [1-3]. Thus, these techniques provide useful structural information on these materials. However, as these materials do not crystallize, detection by by conventional X-ray or neutron scattering is made more difficult. In addition, proton dynamics cannot be probed by XRD studies or interpreted by morphological information. Therefore, alternative techniques to acquire the structural information and proton dynamics of the polymer electrolyte are needed.

Solid state nuclear magnetic resonance (SSNMR) has been executed to probe local structures and determine proton dynamics. Use of solid state NMR in materials chemistry is growing as result of improving technical capabilities. Studies of organic-inorganic hybrid materials [4], proton conductor [5], polymer [6] and H bond of systems have become readily available. This thesis focuses on influences of paramagnetic centers on ^1H spectra of composites materials as well as on studies of proton dynamics in such composites.

2.2 Brief theory of NMR [7, 8]

There are four fundamental properties of a nucleus: mass, charge, magnetism and spin. The nuclei with spin possess spin angular momentum. The spin angular momentum is quantized using the quantum number, I. The value of spin quantum number depends on the particular nucleus and it can be zero, whole integer or multiple of half-integer. The nucleus with zero spin quantum number does not have a magnetic moment and is therefore not observable by NMR spectroscopy. Nuclei whose spin quantum number is not equal to zero are considered to be NMR-active nuclei. The nuclear spin is not perfectly aligned with the external magnetic field but resonates in a conical motion around the direction of external magnetic field and generates a magnetic field by its magnetic moment. The magnetic moment of a nucleus is proportional to the spin through the gyromagnetic ratio, γ, which has a unique value to every NMR active isotope. The total number of spin states for an isolated nuclear spin in a magnetic field can be calculated by $2I + 1$. The orientation of the spin is random and the energy is identical in the absence of external magnetic field. In the external magnetic field (B_o), the hydrogen nucleus ($I=1/2$) will have 2 states ($2(1/2)+1$)).

Two energy states are created corresponding to the two different orientations of nuclear magnetic moments. One magnetic moment is parallel to the direction of B_o and is considered as the low energy spin state; while another magnetic moment anti-parallel to the direction of B_o is considered as the higher spin energy spin state. The energy for the lower energy spin state is given by:

$$E_{1/2} = \frac{\gamma h}{4\pi} B_o \quad \text{Eq. 2-1}$$

The energy for the higher energy spin state is given by:

$$E_{-1/2} = -\frac{\gamma h}{4\pi} B_o \quad \text{Eq. 2-2}$$

The energy difference between the two states is:

$$\Delta E = \frac{\gamma h}{2\pi} B_o \quad \text{Eq. 2-3}$$

The Planck relationship is applied to simplify Eq. 2-3, which yields the following equation:

$$v_o (Hz) = \frac{\gamma}{2\pi} B_o \quad \text{Eq. 2-4}$$

$$\text{Where} \quad \gamma B_o = \omega (rad \quad s^{-1}) \quad \text{Eq. 2-5}$$

v_o is a frequency of electromagnetic radiation, ω is the rate of precession, γ is the gyromagnetic ratio, and B_o is the strength of the external magnetic field in Tesla (T).

The magnetic field strength of an NMR is commonly 11.74 T, which is used in this project. The Larmor frequency of a proton in this field is calculated to 500.12 Hz according to Eq 2-4. Therefore, the radio frequency radiation of 500.12 MHz is applied in order to change the alignment of the magnetic moment of proton from the lower energy spin state to the higher energy spin state.

2.2.1 Solid state NMR

Although solution state NMR is by far the more popular NMR tool in the broad chemistry community, solid-state NMR is a powerful technique for the study of ordered and disordered materials in the solid state, as it can provide not only structural but also dynamic information. For example, using solid state NMR, the structure of Nafion itself has been elucidated by 2D ^{19}F -^{13}C by Chen *et al.* [9], and proton environment and dynamics have been investigated in several papers [10, 11]. Meanwhile, the by-products of Nafion deterioration have been identified by ^{19}F solution NMR [12]. Thus, NMR has been selected for the work in this thesis as the principal technique.

In solution state NMR, rapid molecular tumbling is capable of averaging anisotropic interactions to acquire well-resolved NMR spectra. In static solid state NMR spectra, broad line shapes are attributed to the full effects of anisotropic or orientation-dependent interactions. In this thesis, the anisotropic interaction mainly refers to dipole-dipole coupling among the protons in the solid-state. The difference between solution-state and solid-state NMR is that the weak scalar J coupling is not revealed in solid state NMR. Instead the dipole-dipole coupling through the space is the dominant interaction in the solid- state NMR [13].

The heteronuclear Hamiltonian for a dipolar coupling is shown in Equation 2-6.

The higher the gyromagnetic ratio of the pair of nuclei, the larger the dipolar coupling interaction between them. Hydrogen has high natural abundance and a high gyromagnetic ratio, which causes strong dipolar interaction. In solid state ^{1}H NMR, line broadening is contributed by strong dipolar interactions, which is due to gyromagnetic ratio and high natural abundance of hydrogen.

$$H_{dd} = -\frac{\mu_o \hbar \gamma_i \gamma_j}{4\pi \gamma_{ij}}(3\cos\theta^2 - 1) \qquad \text{Eq. 2-6}$$

Due to anisotropic interactions, the acquisition of well-resolved solid-state NMR spectra is a challenge. Magic angle spinning (MAS) is required in solid state NMR in order to average anisotropic interactions. The dipolar coupling constant contains the ($3\cos^2\theta$-1) term (Eq. 2-6) [14]. θ is the angle between the vector connecting the spins and the magnetic field. The axis of the sample rotor is positioned at the magic angle (54.74°) with respect to B_0. When applying MAS to the sample, the $3\cos^2\theta$-1 term equals to zero [15]. The dipole-dipole coupling interaction is decoupled and the presence of narrow resonance is achieved. The quality of the resolution is proportional to the spinning speed, and dependent on the complexity of the sample (namely, the number of unique protons, and their couplings).

All the solid state NMR experiments were performed under high magic angle spinning rate (25 kHz) in this thesis. The nature of the additives (Manganese oxide) which is the unpaired electron causes the poor resolution of the ^{1}H MAS spectra. Due to the paramagnetic effect, the peak in the spectra becomes relatively wide.

2.2.2 Paramagnetic effect

It is not as simple to acquire Manganese oxide/ Nafion composite spectra using ^1H solid state NMR as for other Nafion composites. The reason for this is due to the paramagnetic effect, which is caused by the existence of unpaired electrons, leading to broader peak widths – an obstacle to achieving high resolution of NMR spectra [13]. The paramagnetic effect is proportional to the magnetic field, the number of unpaired electrons and the gyromagnetic ratio. For example, $LiMn_2O_4$ contains Mn^{3+} and Mn^{4+} ions, which possess 4 and 3 unpaired *d* electrons, respectively. The gyromagnetic ratio of those unpaired electrons is roughly 642 times that of a proton, thereby leading to strong dipolar coupling with protons. The wide peaks at the same time increase the degree of difficulty in analyzing peaks.

In addition to changes in line width, the presence of unpaired electron spin density also influences the spin lattice relaxation times (T_1) [8]. The spin lattice relaxation times for pure Nafion are on the order of seconds, but those of Nafion composites are expected to be on the order of 10^{-6} seconds, which limits the length of the pulse sequences. Electron-Nuclear relaxation becomes more efficient because of the strong magnetic moment of the electrons. Even at very low concentrations of the paramagnetic 0.5 Wt% $LiMn_2O_4$, the influence of unpaired electrons on relaxation time is able to be detected. Further details are explained in Chapter 3. Inversion-Recovery pulse sequences are used to measure spin lattice relaxation times [13]. The relaxation times to be observed in $LiMn_2O_4$

or $K_{0.54}Mn_2O_4$ Nafion composites are expected to show a dramatic decrease in the time scale from seconds to milliseconds, compared to those of pure Nafion.

2.3 Measurement of Proton Dynamics

2.3.1 1-D proton Variable Temperature Experiments

Proton dynamics can be evaluated using ^{1}H NMR variable temperature experiments in fast exchange. Line widths (FWHM – Full Width at Half Maximum) change with temperature, as a result of protons becoming more mobile at higher temperatures. As shown by Eq. 2-7, full width at half maximum (FWHM) is equal to $1/\pi T_2^*$ [13]. T_2^* is the spin-spin relaxation time, which is influenced by homogeneous and inhomogeneous

$$\Delta v_{FWHM} = \frac{1}{\pi T_2^*} \quad \text{(Eq.2-7)}$$

$$\frac{1}{T_2^*} = \frac{1}{T_2} + \gamma \frac{\Delta B_0}{2} \quad \text{(Eq. 2-8)}$$

$$\frac{1}{T_2^*} \approx \tau_c = \tau_\infty \exp\left(\frac{-E_a}{RT}\right) \quad \text{(Eq. 2-9)}$$

contributions (Eq. 2-8). $\triangle B_0$ is the inhomogeneity. Proton conductivity is proportional to proton mobility and the number of protons. Proton mobility can be observed through variable temperature experiments. Eq. 2-9 offers important information activation energy for proton transport. The line width trends of the protons can be determined using the Arrhenius equation. From Eq. 2-7, the change of line width is proportional inversely to T_2*. Eq. 2-8 shows how to calculate E_a from change of line width. The activation energy value is not only helpful to estimate the conductivity of proton but also to show evidence that

Nafion is under protection, by comparing to pristine Nafion sample, as will be seen in Chapter 3.

2.3.2 ^{1}H 2D Exchange Spectroscopy (EXSY) NMR and 1D Selective Inversion

Another method to investigate proton dynamics is achieved using 2D EXSY because the correlation time of the proton motion can be measured. The EXSY pulse sequence is shown in Figure 2-1. After the first 90° pulse excitation, the magnetization along Z axis turns to transverse magnetization and magnetization evolves under its characteristic frequency during the evolution period, t_1. The evolution period is incremented to produce the indirectly detected time domain. At end of the evolution period, a second 90° pulse is applied. The transverse magnetization then is converted to z axis. During the mixing period, the z magnetization of a spin can be transferred to another spin due to site exchange. The transfer of information between spins is accomplished during this period. Owing to the site exchange, the frequency of the spins changes in the mixing time which creates cross peaks (shown in the Figure 2-2) in EXSY spectra. The intensity of cross peaks is proportional to the amount of exchange. The cross peaks will not appear in the spectra if there is no exchange during the mixing time. The magnetization is returned to observable transverse magnetization after the third 90° pulse and is recorded as free induction decay (FID). The variable-temperature EXSY experiments can provide the value of activation energy from the hopping protons by build-up curves of relative normalized cross peak intensity as function of mixing time at different temperatures.

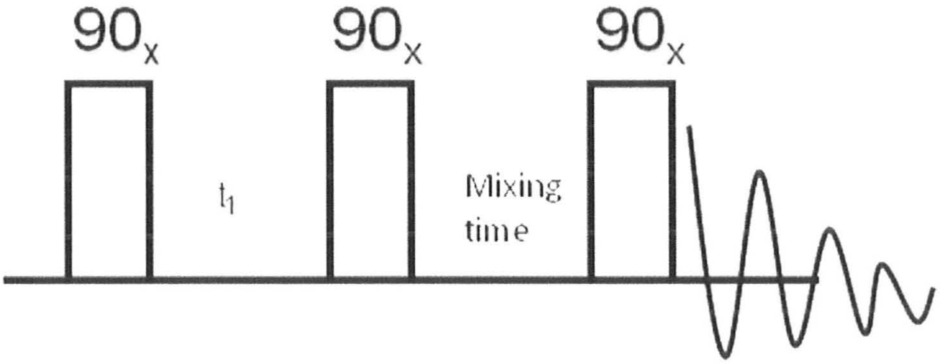

Figure 2-1 The EXSY pulse sequence

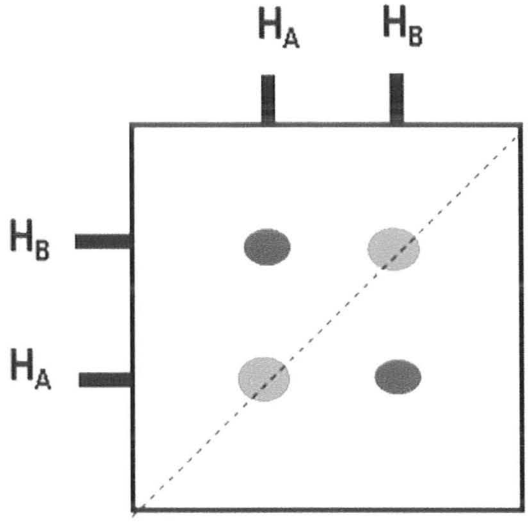

Figure.2-2 An example of 2D EXSY spectroscopy. The green circles represent cross peaks while those in purple represent diagonal peaks.

The variable mixing time allows the magnetization between multiple sites to exchange. However, the value of the mixing time is limited by the T_1 of exchanged resonances [16]. If the mixing time is longer than the T_1, the magnetization is fully relaxed and the intensity of the cross peak decreases. In this case, the complete relaxation of magnetization results in changes in the cross peak intensities. Thus, the proton exchange mechanism is not the only factor that can lead to intensity changes in the cross peaks. As such, the data acquired in this case are not able to provide an accurate value of correlation time of proton exchange. Therefore, a 1D selectively-inverted experiment was performed.

The pulse sequence of a 1D selectively-inverted experiment is described in Figure 2-3. The transmitter is placed on the peak which aims to be inverted and t_1 is equal to $\frac{1}{2}(\Delta V)$. The ΔV is the frequency difference between two different exchanging sites which is shown in Figure 2-4.

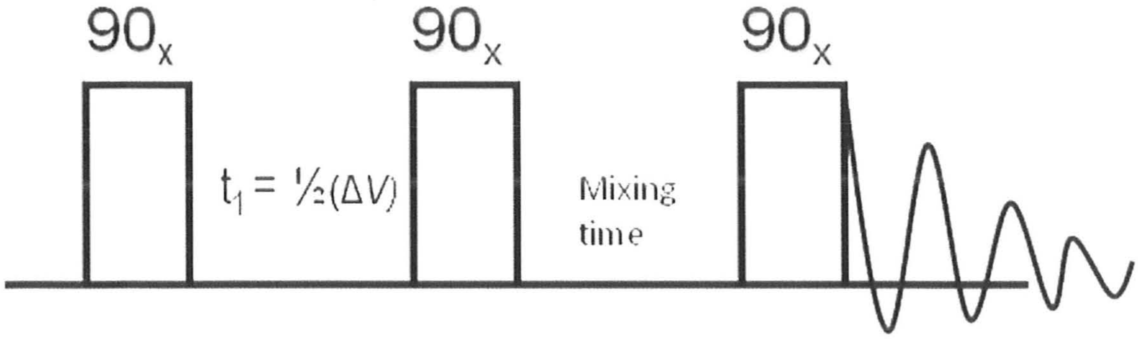

Figure 2-3 Selective Inversion experiment pulse sequence

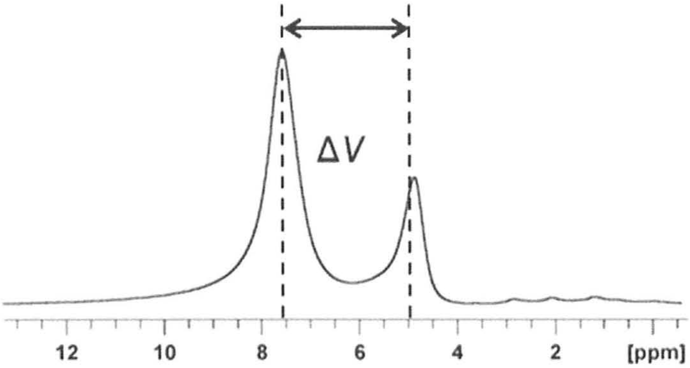

Figure 2-4 Identification of ΔV

The magnetization of two resonances converts to the xy-plane with the first 90° pulse, which allows the magnetization to evolve during the t_1, which is set as the value of $1/2\Delta V$. The second 90 ° pulse reconverts the magnetization back to the Z axis which is shown in Figure 2-5 (d). The different values of mixing time are provided to allow the exchanging interaction between two proton sites which is shown in Figure 2-5 (e). At the end, the magnetizations of the two resonances are brought to observable xy plane and recorded as FID signal.

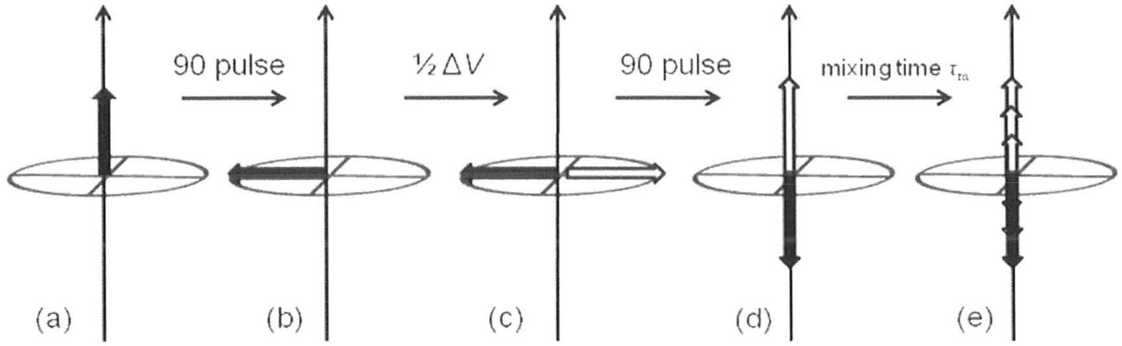

Figure 2-5 Vector representation of pulse for selectively inverted experiment of two resonances.

2.3.3 Dipolar Recoupling Using Double Quantum Filter

Solid-state nuclear magnetic resonance (SS-NMR) can provide information of proton mobility from polymer conductors due to its ability to probe local proton environment. In SS-NMR, Magic Angle Spinning (MAS) is applied in order to reach high spectral resolution of the solid-state sample. In solid-state samples, such as powder samples, the random orientations of molecular and strong homonuclear dipolar couplings contribute to broad peaks, impairing the resolution of solid-state NMR spectra. Executing MAS in solid-state samples can average the dipolar coupling and narrow the line width of broad peaks. The high resolution solid state NMR is achieved with loss of important dynamic information inherent to the dipolar coupling. The dipolar coupling interaction between protons, which carries valuable information of the relative proton mobility, is removed by MAS at same time. Having a method to retrieve information of dipolar coupling in order to understand the mobility of protons is significant [17]. The double quantum filtering pulse sequence has been used to refocus the homonuclear dipolar coupling to obtain the proton dynamic based information such as DRAMA and C7. The dipolar coupling is recoupled by using a back to back (BaBa) [18-20] pulse sequence in this thesis and the pulse sequence is shown in the Figure 2-6. During the excitation period in the BaBa pulse sequence, a double quantum coherence (DQC) is excited by flipping the two spins with parallel spin states (↑↑ and ↓↓) simultaneously. The transition is from M=1 and M= -1, which creates double quantum coherence. The DQC evolves during t_1, before it is reconverted into zero quantum coherence. Following that, the DQC is transferred to observable single quantum coherence (SQC) by a 90° pulse to enable its detection during the acquisition time (t_2). The transition between $M_I = 1/2$ and $M = -1/2$ is referred to as single quantum coherence. The coherence transfer pathway diagram for the BaBa pulse sequence is shown in Figure 2-6. The phase cycles is employed during the t_1 to suppress the higher order coherence. In this case, double quantum coherences remains.

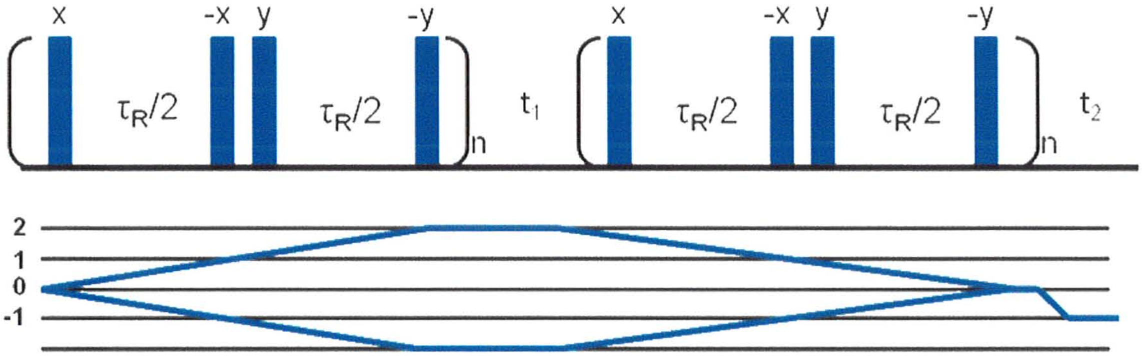

Figure 2-6 Back to Back (BaBa) pulse sequence and coherence transfer pathway diagram for a ^{1}H DQ MAS experiment.

BaBa recouples resonances which have a strong dipolar coupling on the timescale of the rotor period. The intensity of the double quantum coherence is proportional to the strength of the dipolar coupling, excitation time and distance between spins for an individual pair of spins. The immobile protons have relatively strong dipolar coupling interactions compared to mobile protons, which show weak or no dipolar coupling interaction. It means that in the DQF NMR spectra, the resonance of the immobile protons should be revealed in the short excitation time while the resonances of mobile protons are absent. The method to acquire the weak dipolar coupling is by expanding the excitation time. The longer excitation time is able to excite weak dipolar interaction more efficiently than shorter excitation times. Therefore, comparison of MAS NMR with DQF MAS NMR provides the opportunity to distinguish between the relative proton motilities at the molecular level.

2.4 Electron Microscopy

2.4.1 Morphology analysis [21, 22]

Scanning electron microscope (SEM) was used in this project to measure the size and determine the elemental composition of particles and Nafion composites. SEM is a powerful technique that also provides information on the morphology of samples. Due to simple SEM sample preparation, high resolution and wide range of depth of focus, SEM is the most prominent analytical technique in determining morphology.

In this project, the electron gun used to generate an electron beam was a field-emission (FE) electron gun. The diameter of the electron beam from an FE electron gun is limited to 5-10 nm, resulting in high resolution SEM images. Condenser lens and objective lens are able to adjust escaped electrons are then detected. Therefore, it has been seen that the topography of a sample is correlated closely with the amount of secondary electrons detected. From this, morphological information of the specimen can be obtained. The SEM in this thesis is utilized to determine the size of the additives and the distribution of additives in the Nafion composite and the morphology of Nafion following the chemical degradation. the diameter of the incident electron beam. After the interaction between primary electrons of the electron beam and the specimen, secondary electrons (less than

50 eV) are excited. Since secondary electrons are relatively weak in energy, those secondary electrons which are in the deep regions of the specimen (> 500 Å) are not able to escape from the bulk of the specimen. Instead they are absorbed by the specimen. On the other hand, those secondary electrons located at the specimen's surface (within 50-500 Å) escape from the specimen's surface after being bombarded by high-energy electrons. The

2.4.2 Chemical analysis [23]

In SEM, primary electrons from the incident electron beam may interact with the specimen to produce X-ray. An electron in an inner atomic shell is emitted from the sample due to interaction with a high energy incident electron. The ejected electron is in an excited state. Another electron from outer shell drops down to fill the vacant orbits at lower energy level to replace the ejected electron and emits X-rays. Each drop leads to the loss of a specific amount of energy which is corresponding to the energy difference between the outer and inner shells. The X-rays are called characteristic X-rays because the energy of the X-rays can be used to identify the element. Therefore, it is used for chemical analysis. If an ejected electron is from the K shell and the filling electron is from an adjacent lower-energy K shell, the X-ray is called K line (K_α and K_β) X-ray. K_α X-rays usually have the highest energy. On the other hand, if the ejected electrons are from L and M shells, the X-rays are referred to as the L and M lines, respectively. Energy-dispersive X-ray spectroscopy (EDS) is one common X-ray detection technique that allows for identifying chemical composition by detecting the energies of the X-rays.

2.5 Fourier Transform Infrared Radiation [24]

Infrared spectroscopy is typically used to identify the presence of different classes of functional groups by observing different types of vibrations in the characteristic group frequency region (4000-1300 cm^{-1}). However, in this project, the focus is on the fingerprint region (1300-600 cm^{-1}). The energy of infrared photons is not high enough to trigger electronic transitions, but is able to cause bonds in a molecule possessing a net dipole moment to vibrate. Bonds in the molecules absorb certain wavelengths and frequencies from infrared radiation. The operating wavelength region of infrared radiation sits between the visible light and microwave regions, ranging from 10^{-5} and 10^{-2} cm. In addition, some molecules do not absorb infrared radiation because of the absence of a net dipole moment in the bond. Bonds capable of absorbing infrared radiation are IR active [25, 26]. The heteropolyacid ($H_3PW_{12}O_{40}$) Nafion composite is chosen to be characterized by FTIR in this work in order to confirm the presence of low concentrations of heteropolyacid in Nafion composite. By looking for stretching vibrations of P-O and W=O bonds in the fingerprint region of FTIR, the existence of heteropolyacid can be proven [27].

2.6 Conductivity Test

An insightful technique to determined membrane's conductivity is impedance spectroscopy, which is a technique regularly applied to fuel cell membranes [28, 29]. Ideally, Ohms law applies and shows that voltage (v) is equal to current (I) times resistance (R).

$$IR = V \qquad \text{(Eq 2-10)}$$

However, the system is not ideal and the Ohm's law is applied into electrochemical impedance spectroscopy. The ratio revealed in Eq. 2-11 is called impedance of the system which depends on the frequency of the signal. Therefore, the impedance of an electrolyte as a function of frequency can be acquired by varying the frequency. Basically, the known amplitude (current or voltage) and chosen range of frequency of an AC sinusoidal excitation signal is sent to the cell and the phase change of amplitude (current or voltage, correspondingly) is recorded. The Bode plot (Figure 2-7) is a very clear method to present the impedance data. The absolute value of impedance (log|Z|) is recorded while the phase difference is zero. At low frequency range, the phase is close to zero and the impedance of the sample shows the independence on frequency change. In this case, the impedance (log|Z|) is given in the bode plot.

$$Z(\omega) = \frac{V \exp(i\omega t)}{I \exp(i\omega t - i\theta)} \qquad \text{(Eq 2-11)}$$

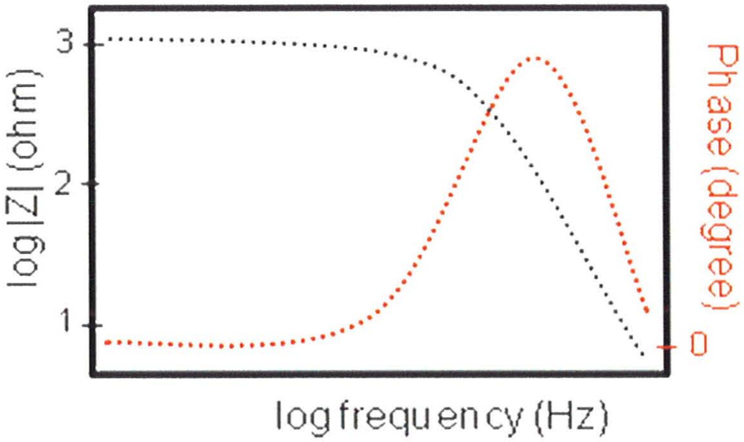

Figure 2-7 An example of a bode plot.

The conductivity of the membrane can be calculated by Eq. 2-12 [30]. *d* is the distance that the ions travel between the two inner electrodes, R is the real component of the impedance, l is the width of the membrane, and h is the thickness of the membrane and σ is ionic conductivity.

$$\sigma = d / R \cdot l \cdot h \qquad \text{(Eq 2-12)}$$

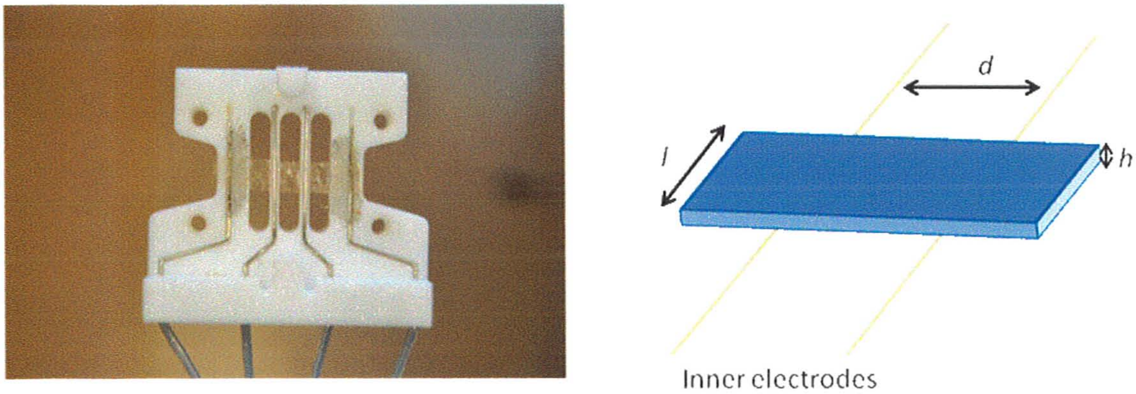

Figure 2-8 Membrane geometry in the 4 probe conductivity cell.

The connections consist of four different electrodes (a counter electrode, a working electrode and two reference electrodes). Two outer electrodes (the counter and working electrodes) are used to apply a constant current across the sample while two inner electrodes (the reference electrodes) are used to record the voltage. The four probe method was selected to measure the proton conductivity of Nafion and the composites presented in this thesis. This method is useful to avoid the internal resistance, which is contributed by the electrodes, because this method is insensitive to the contact impedance of electrode. Therefore, the resistance acquired from the four probe method is mainly contributed by ionic conductance. The advantage of using four-probe method is to measure low impedance devices. The geometry of the four-probe method is shown in Figure 2-8.

2.7 References

1. W. Y. Hsu, T.D.G., Ion transport and clustering in nafion perfluorinated membranes Journal of Membrane Science, 1983. 13: p. 307.

2. T.D. Gierke, G.E.M., F.C. Wilson, J. Polym. Sci. Polym. Phys, 1981. 19: p. 1687.

3. W. Y. Hsu, T.D.G., Macromolecules, 1982. 15: p. 101.

4. S. M. De Paul, J.W.Z., R. Ulrich, U. Wiesner, and H. W. Spiess, Structure, Mobility, and Interface Characterization of Self-Organized Organic-Inorganic Hybrid Materials by Solid-State NMR Journal of the American Chemical Society, 1999. 121: p. 5727.

5. G. R. Goward, M.F.H.S., Daniel Sebastiani, Ingo Schnell, and Hans Wolfgang Spiess, High-Resolution Solid-State NMR Studies of Imidazole-Based Proton Conductors: Structure Motifs and hemical Exchange from ^{1}H NMR Journal of Physical Chemistry B, 2002. 106: p. 9322.

6. Ümit Akbey, R.G., Yuan G. Peng, Peter P. Chu, Hans W. Spiess, Solid-State NMR investigations of anhydrous proton-conducting acid–base poly(acrylic acid)–poly(4-vinyl pyridine) polymer blend system: A study of hydrogen bonding and proton conduction. J of polymer science B, 2009. 47: p. 138.

7. P.J. Hore, in Nuclear Magnetic Resonance 1995, Oxford Science Publications: New York.

8. R.K. Harris, in Nuclear Magnetic Resoance Spectroscopy. 1983, Potman Publishing Inc. p. 68,81.

9. Q. Chen, and K. Schmidt-Rohr, F-19 and C-13 NMR signal assignment and analysis in a perfluorinated ionomer (Nafion) by two-dimensional solid-state NMR. Macromolecules, 2004. 37(16): p. 5995.

10. G. Ye, C.A. Hayden, and G.R. Goward, Proton dynamics of nafion and Nafion/SiO2 composites by solid state NMR and pulse field gradient NMR. Macromolecules, 2007. 40(5): p. 1529-1537.

11. G. Ye, N. Janzen, and G.R. Goward, Solid-state NMR study of two classic proton conducting polymers: Nafion and sulfonated poly(ether ether ketone)s. Macromolecules, 2006. 39(9): p. 3283.

12. J. Healy, et al., Aspects of the chemical degradation of PFSA ionomers used in PEM fuel cells. Fuel Cells, 2005. 5(2): p. 302.

13. E.D. Becker, in High resolution NMR: Theory and chemical applications 2000, Acdemic Press. p. 32-39,184, 220-222.

14. M. J. Deur, Solid State NMR Spectroscopy: Principles and Applications. 2002: Blackwell Science.

15. R.S. Macomber, A Complete Introduction to Modern NMR Spectroscopy. 1997: A Wiley Interscience Publication. 284-285.

16. A.D Bain, e.a., Nucl magn Reson. Spectrosc, 2003. 43: p. 63.

17. S.P. Brpwn, H.W.S., Chemical Reviews 2001. 101: p. 4125.

18. M. Feike, J Magn Reson A, 1996. 122: p. 214.

19. I. Schnell, J Magn Reson A, 2001. 151: p. 153.

20. S.P. Brown, prog Nucl Magn Reson Spectrosc 2007. 50: p. 199.

21. J.W.S. Hearle, J.T.S., P.M. Cross, in The Use of the Scanning Electron Microscope. 1972, Pergamon Press Ltd: Oxford.

22. B.L.Gabriel, in SEM: A User's Manual for Materials Science. 1985, American Scoiety For Metals.

23. Bell, A.J.G.-R.D.C., in Energy-Dispersive X Ray Analysis in the Electron Microscope. 2003, BIOS Scientific Publishers: Oxford.

24. D.A. Skoog, F.J.H., T.A. Nieman, in Principles of Instrumental Analysis. 1998. p. 381.

25. P.R Griffiths and J. A. de Haseth, Fourier Transform Infrared Spectrometry. 1986, New York: John Wiley.

26. L.G. Wade, J., Organic Chemistry. 1999, Uppers Saddle River: Pentice Hall International.

27. C. Rochiccioli-Deltcheff, M.F., R. Frank, R. Thouvrnoc, Inorg. Chem, 1983. 22: p. 207.

28. J.R. Selman, Y.P.L., Electrochimica Acta, 1993. 38: p. 2063.

29. Y. Sone, P.Ekdunge, D. Simonsson, Proton Conductivity of Nafion as Measured By a Four-Electrode AC Impedance Method. J of Electrochemical Society, 1996. 143: p. 1254.

30. A. K. Jonscher, Nature, 1977. 267: p. 673.

Chapter 3

Understanding of the Degradation Mechanism of Nafion/ Manganese and Cerium Oxide Composite Attacked by Hydroxyl Radical

This chapter describes sample preparation of potential metal oxide scavenger and Nafion composites as well as data acquisition procedures including NMR, SEM and XRD. Firstly the elemental composition of the metal oxide is characterized by XRD and SEM-EDS. The concentration of by-products from Nafion degradation of different Nafion composites was studied using ^{19}F *solution state NMR. Proton dynamic information was determined by high resolution solid state NMR from the Nafion composites.*

3.1 Introduction

Nafion is a well known Polymer Electrolyte Membrane (PEM) for fuel cell applications. However, the membrane is susceptible to attack by hydroxyl radicals generated during fuel cell operation. This causes a thinning of the Nafion membrane and a loss of efficiency in the device. Nanoparticles of manganese oxide and cerium oxide are considered as free radical scavengers and may offer protection to the membrane from free radical attack. In Table 3-1 and Table 3-2, the reaction rate between the radical scavenger candidates (Mn^{2+} and Ce^{2+}) and a free radical (•OH) is faster than the degradation rate between Nafion and hydroxyl radical. It indicates that the presence of the radical scavenger candidates in the Nafion can diminish the free radical attack by deactivation the free radical before attacking Nafion. Here, Fenton's test is used to simulate the conditions of Nafion under attack by radical species and also accelerates the degradation rate. ^{19}F solution state NMR is used to assess the level of protection by providing information on both the identity and quantify the abundance of Nafion's degradation products. $LiMn_2O_4$ and $K_{0.54}Mn_2O_4$ at 0.5 weight percent loading in Nafion composites both show excellent levels of protection. Solid state ^1H NMR is used to determine proton dynamics within the Nafion composites. ^1H MAS NMR spectra show changes in line width during variable temperature experiments that are comparable to similar experiments on Nafion that has not been exposed to free radicals. This data demonstrates that the activation energy for proton transport is unchanged before and after exposure to •OH, thus strongly suggesting that the Nafion is protected by the additives used. This protection is attributed to delocalized electrons reacting with the free radicals before damage can take place. As well, the reduction in the number of available unpaired electrons ($H^+ + Mn^{3+} + \bullet OH \rightarrow H_2O + Mn^{4+}$) causes the ^1H NMR line width to narrow following Fenton's test. Despite the challenges posed by the paramagnetic ions, solid state NMR provides definitive evidence of the quantity and role of the free radical scavengers as a function of •OH exposure.

Table 3-1 Degradation mechanism and degradation rate of non-chemical stable Nafion membrane under a free radical attack

Degradation Mechanism	Degradation rate
$-CF_2CO_2H + \bullet OH \rightarrow -CF_2CO_2\bullet + H_2O$	$k < 1.0 \times 10^6\ M^{-1}s^{-1}$
$-CF_2H + \bullet OH \rightarrow -CF_2\bullet + H_2O$	$k < 1.0 \times 10^7\ M^{-1}s^{-1}$

Table 3-2 Protection mechanism and protection rate of potential radical scavenger react with a free radical.

Protection mechanism	Protection rate
$Ce^{3+} + \bullet OH + H^{+} \rightarrow Ce^{4+} + H_2O$	$k = 3 \times 10^{8}\ M^{-1}s^{-1}$
$Mn^{2+} + \bullet OH + H^{+} \rightarrow Mn^{3+} + H_2O$	$k = 4 \times 10^{7}\ M^{-1}s^{-1}$
$Mn^{3+} + H_2O_2 \rightarrow Mn^{2+} + \bullet OOH + H^{+}$	$k = 7 \times 10^{4}\ M^{-1}s^{-1}$

3.2 Experimental

3.2.1 Sample Preparation

The methods use to synthesize cerium oxide, manganese oxide and $K_{0.54}Mn_2O_4$ are described in this section.

3.2.1.1 Preparation of Cerium Oxide

Cerium (III) Nitrate $6H_2O$ was mixed with solution of cetyl trimethyl ammonium bromide (CTAB), 1-butanol and n-octane. This was followed by addition of NaOH [1]. After magnetic stirring for one hour, yellow CeO_2 nanocrystals formed. Triplicate methanol washes and centrifuging steps were applied to ensure purity of the samples.

3.2.1.2 Preparation of Manganese Oxide

$KMnO_4$ was dissolved into de-ionized (DI) water along with fumaric acid in a mole ratio of 3:1. The solution was first stirred for an hour and then was vacuum degassed for another hour in order to remove the CO_2 and obtain a homogeneous solution. After stirring for 24 hours, 3 M H_2SO_4 was added drop wise until the pH of the solution reached. This was then followed by another 24 hours of stirring. To obtain powdered manganese oxide, several rinses with DI water followed by centrifugation was necessary. The powder was oven-dried at 70 °C for two hours. In addition, two types of manganese oxides are used in this experiment. They are Mn_2O_3 and MnO_2, which were purchased from Wako and Aldrich. Synthesized manganese oxide powder was heated up to 300 °C, 400 °C, 500 °C, 600 °C, 700 °C and 800 °C at a rate of 5 °C /min under Ar gas for 5 hours before cooling at room temperature [2].

3.2.1.3 Preparation of $K_{0.54}Mn_2O_4$

A mixed solution containing 3% H_2O_2 and KOH was added to 0.3 M $Mn(NO_3)$. The reaction occurred immediately at room temperature. After aging for one hour, the product was washed with water, filtered, and dried [3].

3.2.1.4 Casting Nafion Membrane

Manganese/cerium oxide powders were mixed with a Nafion solution in a supersonic bath for several hours until suspension of the powder occurred. The solution was poured into a petri dish which stabilized at room temperature leading to the formation of the Nafion-composite film.

3.2.2 Durability Test of Nafion

Fenton's test is the most common and simple method to test Nafion durability [4, 5]. Fenton's test [6] is used to accelerate the level of Nafion degradation by immersing Nafion into a Fenton solution (containing mainly H_2O_2 with M^{2+} ions). Fenton's test simulates the conditions of an operating fuel cell where the different kinds of harmful radicals known to attack Nafion are generated (Equation 3-1, 3-2 and 3-3). In this study, Nafion membranes were immersed in 15 ml of a Fenton solution comprised of 30 % H_2O_2, 50 μL of $FeCl_2$ solution (to achieve $[Fe^{2+}]$ of ~ 9 ppm). After placing a given mass of the Nafion membrane into the solution, the solution was stored in a High-density polyethylene (HDPE) wide mouth bottle which was then heated to 88 °C for 24 hours to facilitate the Nafion degradation in relatively short time. Fenton's test solution is unstable over long term storage therefore; fresh Fenton's solution is required for each heat treatment.

1.$H_2O_2 + Fe^{2+} \rightarrow HO\bullet + OH^- + Fe^{3+}$ Initiation (Eq 3-1)

2. $H_2O_2 + HO\bullet \rightarrow HO_2\bullet + H_2O$ Chain propagation (Eq 3-2)

3.$Fe^{3+} + HO_2\bullet \rightarrow Fe^{2+} + H^+ + O_2$ Termination and Catalyst regeneration (Eq3- 3)

3.2.3 NMR Spectroscopy

All NMR experiments were performed at Larmor frequencies of 500.13 MHz for ^1H NMR and 475 MHz for ^{19}F NMR. ^1H NMR spectra were acquired under MAS conditions (25 kHz) using a 2.5 mm HX probe.

3.2.3.1 ^1H NMR

^1H solid state NMR experiments were performed on a Bruker AV500 spectrometer at a ^1H Larmor frequency of 500.13 MHz. A 2.5 mm diameter rotor was used for Nafion samples and was spun at 25 kHz. A recycle delay of 3 s and a pre-scan delay of 4.5 μs were used. The spectra were referenced to adamantane (1.63 ppm for ^1H). Solid state ^1H NMR spectra were acquired with a 90° pulse length of 2.5 μs. ^1H NMR variable temperature experiments were carried out on the same Bruker 2.5 mm MAS probe over a temperature range of 300 K to 360 K

3.2.3.2 ^{19}F NMR

^{19}F solution state NMR experiments were performed on a Bruker AV 500 spectrometer at a ^{19}F Larmor frequency of 475 MHz. The ^{19}F NMR spectra were acquired with a 90° pulse length of 3.5 μs, and referenced to $CFCl_3$ (0 ppm for ^{19}F NMR). The spectra were collected with 512 scans. The sweep width is 100000 Hz and recycle delay is 1s.

3.2.4 Regeneration Acid form Nafion

Nafion is well known as an ion exchange membrane; therefore, after treatment in ionic solution the protonated form must be regenerated. In the Fenton's test bath, ferric and ferrous ions exist, which leads to cation-exchange between the Nafion protons and iron ions. This is problematic for the materials, as the proton conductivity is diminished by the loss of H^+ but also for ^{1}H MAS NMR experiments as the poor proton intensity of was revealed. Furthermore, iron ions possessing unpaired electrons leads to broad NMR lineshapes thus also increasing the difficulty for NMR analysis. In order to have a H^+ conducting membrane as well as viable NMR spectra, a H_2SO_4 wash is used to restore the Nafion protons.

3.2.5 X-ray powder diffraction

Powder x-ray diffraction experiments were performed on a Bruker D8 powder diffractometer. The step was 0.04° /s. 2θ =10-60°.

3.2.6 Scanning Electron Microscope

Scanning electron images were taken using (JEOL 7000F) with working voltage at range of 5-15 Kv. Samples were place on carbon tape which attached to Cu sample holder. A thin layer of Au (Au particles' diameter are around 5nm) was sputtered over the sample to improve the electrical conductivity to reduce the sample charging.

3.3 Result and Discussion

3.3.1 CeO_2 Composite in Nafion [7]

Figure 3-1 shows a ^{19}F solution state NMR spectrum of Nafion doped with different weight percentages (5 %, 1 % and 0.5 %) of CeO_2. The product from Nafion degradation is shown in the Figure 1-6 which was completely assigned to ^{19}F solution state NMR [4]. The intensity of three main characteristic peaks at -82, -118 and -126 ppm is used to quantity the amount of the product of Nafion degradation. This is determined from the relative intensity of characteristic peaks from ^{19}F solution state NMR for degradation product where the best protection is indicated by an absence of peaks. These results show that Nafion with a high loading weight percent (5 %) of CeO_2 exhibits less intensity than a low weight percent sample (0.5 %), which is consistent with the observed increase in protection from radical attack.

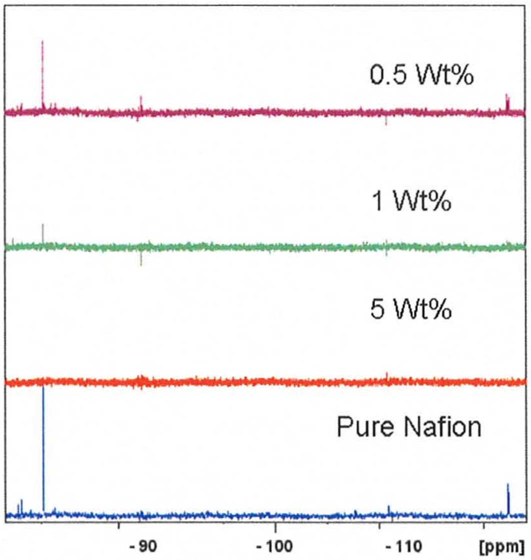

Figure 3-1 ^{19}F NMR of Nafion membranes protected by variable loading Wt% of CeO_2, ns=500, pulse length= 8.5 μs, power level= -4 dB and delay time=1 s

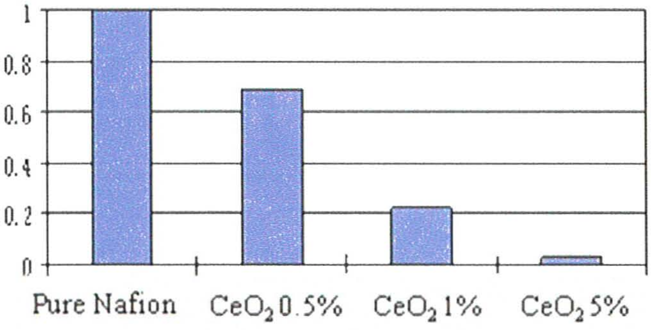

Table 3-3 Relative intensity of -82 ppm signal for different loading % of CeO_2 in the Nafion membrane

The unzipping reaction is considered to be the main Nafion degradation mechanism. The rate of the unzipping reaction is 100 times slower than the protection rate meaning that aggressive hydroxyl radicals are consumed by Ce^{3+} before Nafion degradation can occur. The Ce^{3+} ions are present in CeO_2 act as radical scavengers.

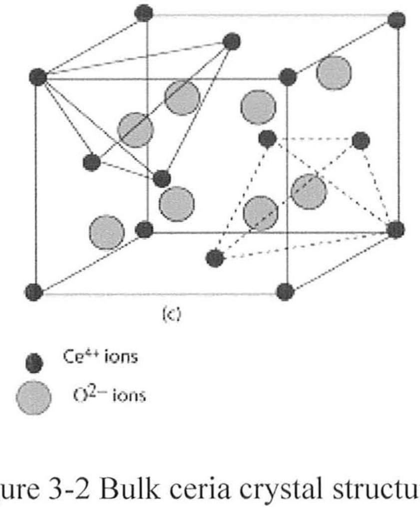

Figure 3-2 Bulk ceria crystal structure [8]

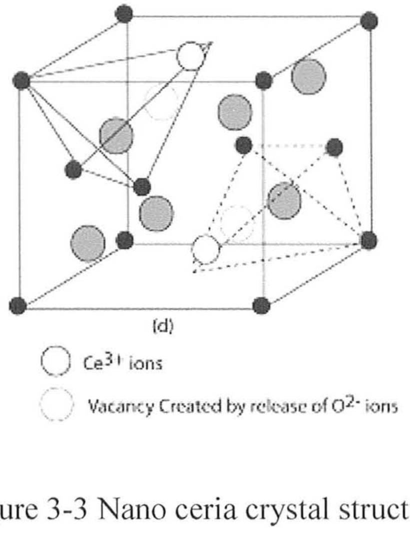

Figure 3-3 Nano ceria crystal structure [8]

However, Ce^{3+} is unstable in nature, which is easily oxidized and prefers to stay as Ce^{4+} state (CeO_2). Small amounts of Ce^{3+} are present in CeO_2 means that higher weight percentages of loading are needed to afford membrane protection. One way of generating higher Ce^{3+}/Ce^{4+} ratios is through use nano particles. Desphande and Zhang [8, 9] report that there is an increase in the CeO_2 lattice parameter with decreasing particle size. The lattice parameter is 0.5401 nm in 5 μm CeO_2 particles (Figure 3-2) but then increases to

0.5433 nm in 6 nm CeO_2 particles (Figure 3-3). Zhang [9] shows that the increase in lattice parameter is due to oxygen vacancies resulting in the formation of Ce^{3+} ions. Using the oxygen vacancy as well as the higher ionic radius of Ce^{3+} (which is 0.1143 nm as compared to Ce^{4+} ions 0.092 nm) the increase in the lattice parameter of the 6 nm CeO_2 particles, 0.5433 nm is found. It is consist with results from XRD calculations. Therefore, CeO_2 nanoparticles are preferred.

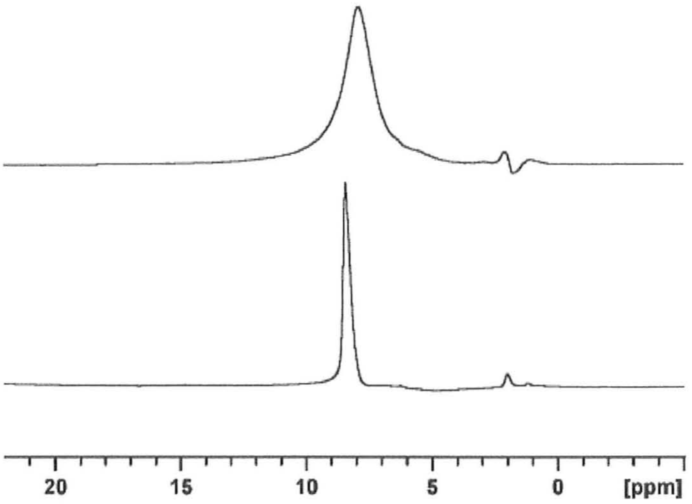

Figure 3-4 ^1H MAS NMR of 5 Wt% dried CeO_2/ Nafion (top) and pure Nafion (bottom) before free radical attack, MAS= 25 khz, ns=32, pulse length= 8.5 μs, power level= -4 dB and delay time=1 s

^1H Solid-state NMR

Figure 3-4 shows the ^1H solid state NMR spectrum of 5 % CeO_2/Nafion and pure Nafion. It is worth noting that the line width of CeO_2/Nafion is 650 Hz, which is considerably broader than pure Nafion. The Ce^{3+} has one unpaired electron which contributes to a wide line width. Because 5 % CeO_2 was required to achieve good protection, this composite was not further persued.

3.3.2 MnO_2, Mn_2O_3 and Mn_3O_4

Andrews [10] suggests that MnO_2 is able to reduce the Nafion degradation rate when added into Nafion. As such, MnO_2 may function as a hydrogen peroxide decomposition agent ($2MnO_2 + H_2O_2 \rightarrow Mn_2O_3 + O_2 + H_2O$). Moreover it also indicates performance loss at high loading of MnO_2 on Nafion. Therefore, particles added at a low weight percent are preferred. Several patents [10-12] indicate that added manganese compound with divalent and trivalent into Nafion is able to maintain fuel cell efficiency during long-term operation. The reason is that Mn^{2+} and Mn^{3+} react with free radicals and are oxidized to Mn^{3+} and Mn^{4+}, respectively. Therefore, less free radicals are available to contribute to damage of the Nafion membrane.

Table 3- 4. Oxidation state of different Manganese oxide

Manganese oxide	MnO_2	Mn_2O_3	Mn_3O_4	$K_{0.54}Mn_2O_4$
Oxidation state	4^+	3^+	3^+ and 2^+	4^+ and 3^+

MnO_2, Mn_2O_3 (Aldrich 325 mesh) and Mn_3O_4 (Heat treatment from MnO_2), are chosen as additives in order to compare how differences in the oxidation state of manganese oxide affects the Nafion protection capability. The oxidation state of additives is summarized in Table 3-4. Particle size of these additives also affects the performance capabilities. Overall, higher surface area will offer better protection. The particle sizes of the different metal oxides are observed by scanning electron microscopy (SEM).

Figure 3-5 shows the MnO_2 particle size being less than 10 nm. Figure 3-6 shows that after heat treatment (800 °C), MnO_2 particles are converted into Mn_3O_4 particles with substantially increased sized particles comprised of two different morphologies (round-shaped and rectangular-shaped particles). The round-shaped particles are approximately 100 nm in diameter while the rectangular-shaped particles may be up to 1um in length. The particle size for Mn_2O_3 particles is less than 44 μm.

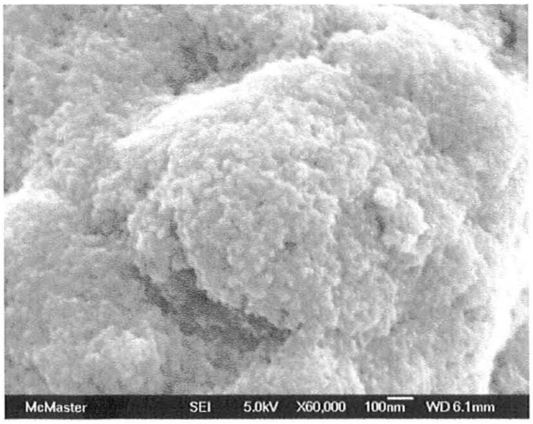

Figure 3-5.SEM image of MnO_2 particles

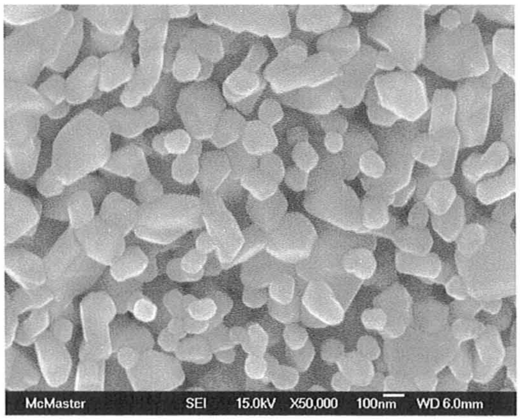

Figure 3-6. SEM image of Mn_3O_4 particles

Each of these particle types are combined separately with a Nafion solution of varying weight percentages. The ^{19}F NMR is used to determine the degree of protection offered by a given additive after undergoing Fenton's test. This is determined from the relative intensity of characteristic peaks where the best protection is indicated by an absence of peaks. The ^{19}F NMR (Figure 3-7 to 3-9) data shows that Nafion with lower weight percent (<1%) of MnO_2, Mn_2O_3 and Mn_3O_4 700 °C particles have similar intensity at -82, -118, -126 ppm in spectra as Nafion without any protective additives. These additives therefore, are not able to achieve a high level of protection at low loading. In contrast, particle loading of greater than 5% in Nafion is able to achieve significant protection. However, in Figure 3-10, Nafion with Mn_3O_4 800 °C at low weight percent (<0.5%) shows the best protection level.

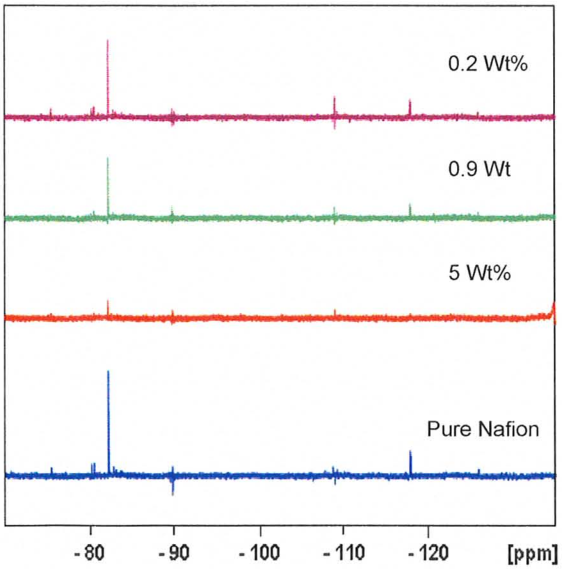

Figure 3-7. ^{19}F NMR for Nafion composite with different weight % (0.2 %, 0.9 % and 5 %) MnO_2 oxide particles

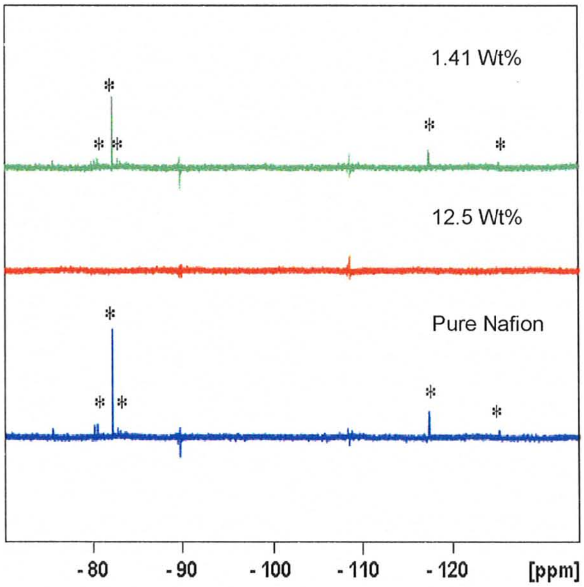

Figure 3-8. ^{19}F NMR for Nafion composite with different weight % (1.41 % and12.5 %) Mn_2O_3 oxide particles.

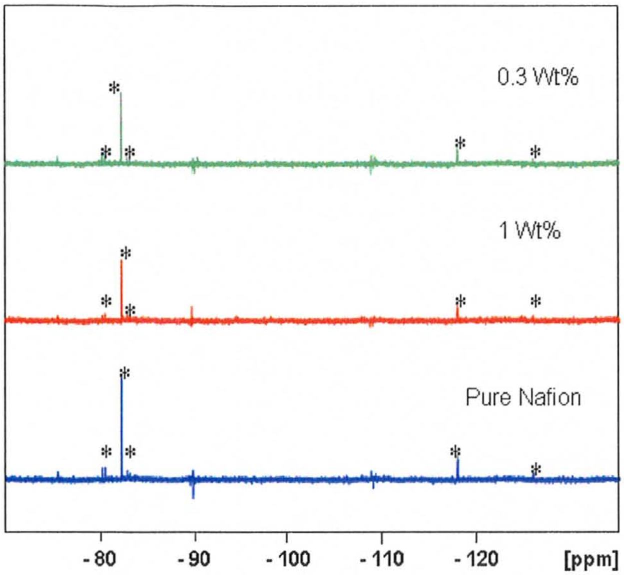

Figure 3-9. ^{19}F NMR for Nafion composite with different weight % (0.3 % and 1 %) Mn_3O_4 particle preparation at 700 °C

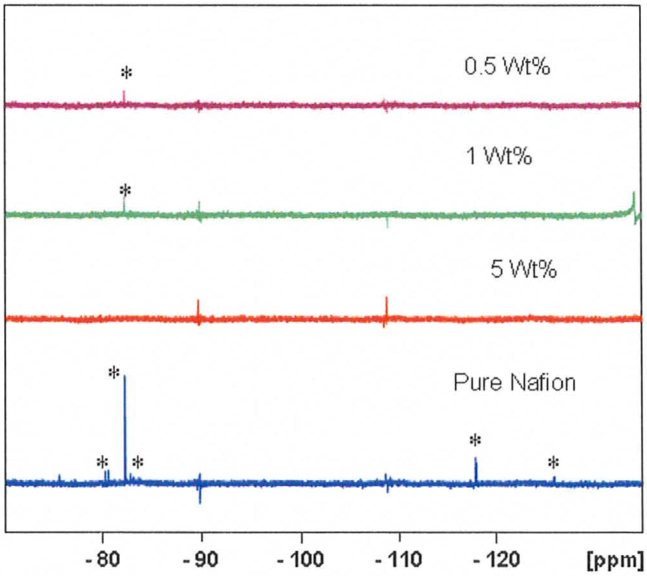

Figure 3-10. ^{19}F NMR for Nafion composite with different weight % (0.5 % 1 % 5 %) Mn_3O_4 particle preparation at 800 °C

Composites are prepared by using particles treated at different temperatures. These composites were therefore further investigated using powder XRD and TEM. Figure 3 11and 3-12 show XRD result on these particles where the Mn_3O_4 under 800 °C has a more obvious $K_{0.54}Mn_2O_4$ content than the 700 °C treated sample. This is in agreement with the TEM results in Figure 3-13.

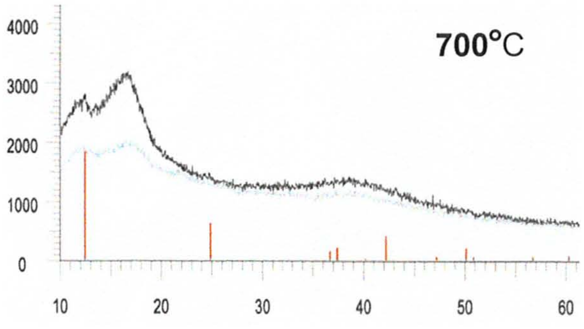

Figure 3-11. XRD for Nafion composite with Mn_3O_4 particle preparation at 700 °C

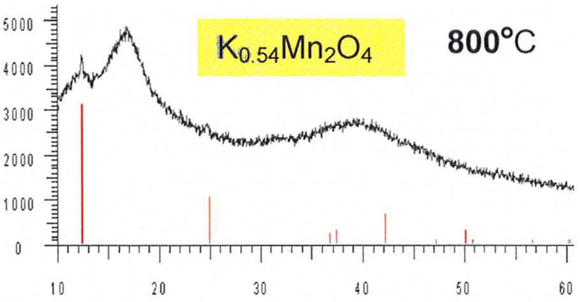

Figure 3-12. XRD for Nafion composite with Mn_3O_4 particle preparation at 800 °C

Figure 3-13 TEM shows the conspicuous bar-shaped particles from Mn_3O_4 treated at 800 °C. TEM-EDX (Figure 3-14) was then used to detect for any possible potassium content in this particular morphology. As a result, the bar-shaped particles were classified as $K_{0.54}Mn_2O_4$.

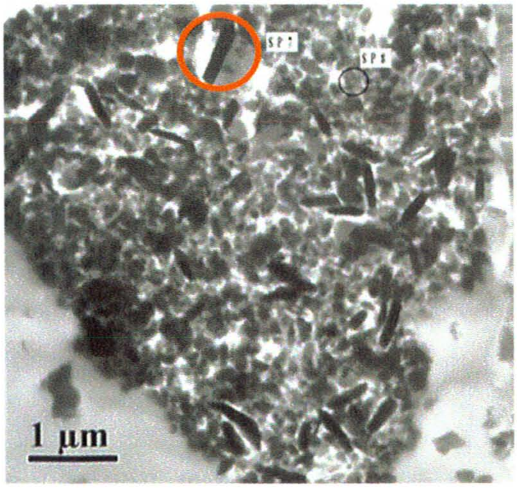

Figure 3-13. TEM for Nafion composite with Mn_3O_4 particle preparation at 800 °C

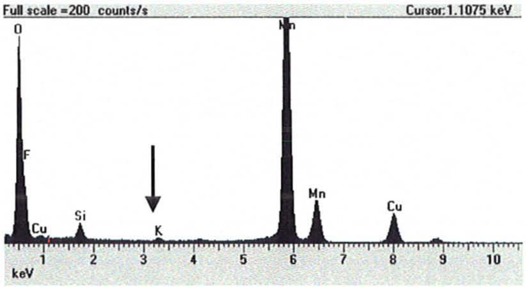

Figure 3-14. TEM-EDX on rectangular particles from Mn_3O_4 particle preparation at 800 °C

It is noteworthy that the Nafion / Mn composite (700 °C) containing only Mn_3O_4 does not perform well. It can be concluded that better radical scavenger ability is attributed to additional $K_{0.54}Mn_2O_4$ found in the 800 °C Mn_3O_4 powders. It is also noteworthy that the observed results show that free radical attack is better prevented by the oxide with fewer unpaired electrons, counter to our original hypothesis. Therefore, we propose a role for the hopping semiconductor, such as $K_{0.54}Mn_2O_4$ in which the $K_{0.54}Mn_2O_4$ may contribute delocalized electrons to react with the free radicals. A method to prove this hypothesis is to prepare composite membranes using $K_{0.54}Mn_2O_4$ directly or alternatively, $LiMn_2O_4$. $LiMn_2O_4$ is mixed valence compound and also well known as a hopping semiconductor where the electrons are delocalized over e_g orbitals of manganese metal centers [13]. This is possible because all Mn ions (regardless of oxidation state) are on octahedral sites. In contrast, Mn_3O_4 is also mixed valence compound but there is no electron transfer between Mn^{3+} and Mn^{2+} because the different Mn oxidation state have different geometries (Mn^{3+} ions are on octahedral sites and Mn^{2+} ions are on tetrahedral sites) [14]. In order to prove oxidation state change occurs in manganese oxide during the free radical attack, a TEM-EELS investigation is proposed for future work.

3.3.3 $LiMn_2O_4$ and $K_{0.54}Mn_2O_4$

Figure 3-15 and 3-16 show that $LiMn_2O_4$ and $K_{0.54}Mn_2O_4$ particles are as much as 10^6 times larger than all the aforementioned manganese oxide particles.

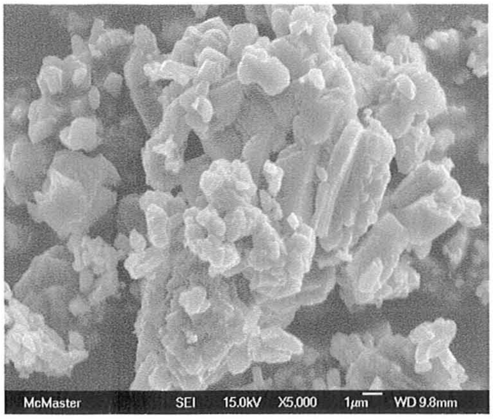

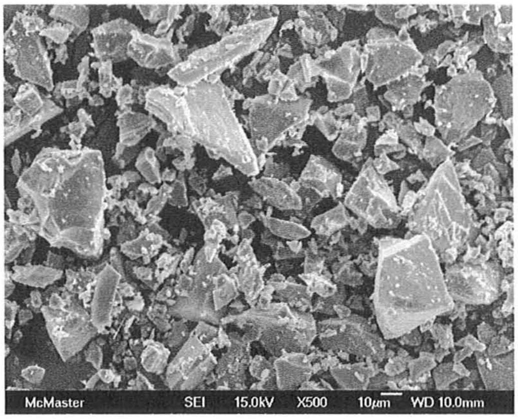

Figure 3-15 SEM image $LiMn_2O_4$ particle

Figure 3-16 SEM image $K_{0.54}Mn_2O_4$ particle

Figure 3-17 and 3-18 show ^{19}F NMR spectrum of Nafion, doped with 0.5 Wt% of $LiMn_2O_4$ and 0.5 Wt% $K_{0.54}Mn_2O_4$, following Fenton's test. Both spectra have relatively low intensity peak (approximately 15-20% intensity relative to pure Nafion) at characteristic positions (-82, -118, -126 ppm). This indicates that delocalized electrons react with free radical before Nafion degradation occurs. Therefore, there is lower concentration of Nafion degradation by-products.

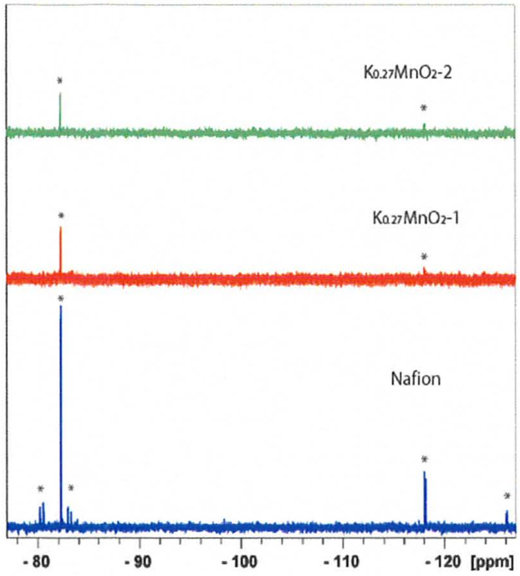

Figure 3-17 ^{19}F NMR of Nafion Membranes Protected by 0.5 Wt% $K_{0.54}Mn_2O_4$

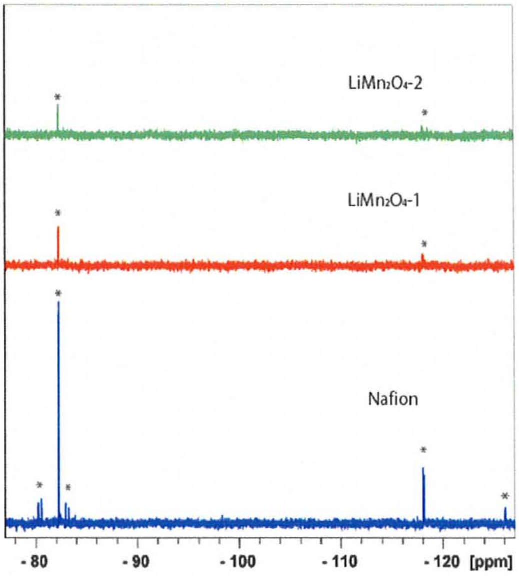

Figure 3-18 ^{19}F NMR of Nafion Membranes Protected by 0.5 Wt% $LiMn_2O_4$

3.3.3.1 ^1H NMR for Nafion $LiMn_2O_4$ and Nafion $K_{0.54}Mn_2O_4$

Figure 3-19 show ^1H MAS spectra of the respective samples before Fenton's test. The spectra from $LiMn_2O_4$ and $K_{0.54}Mn_2O_4$ have broad peaks compared to that of pure Nafion. This is due to the paramagnetic effect. Table 3-5 shows the average oxidation for Mn ions in $K_{0.54}Mn_2O_4$ and $LiMn_2O_4$, which can explain why the linewidth (2600 Hz) for the $LiMn_2O_4$ doped Nafion, is wider than linewidth (520 Hz) of the $K_{0.54}Mn_2O_4$ doped Nafion. The Mn oxidation state of $LiMn_2O_4$ is 3.5 whereas the Mn oxidation state for $K_{0.54}Mn_2O_4$ is 3.75. This means that there is 50% Mn^{3+} and 50%Mn^{4+} ions in $LiMn_2O_4$ but for $K_{0.54}Mn_2O_4$ only 25% of the Mn ions are in the 3+ state. Less Mn^{3+} ions (having 4 unpaired electrons) in $K_{0.54}Mn_2O_4$ means there is a weaker paramagnetic effect. As a result, the line width of (520 Hz) $K_{0.54}Mn_2O_4$ is narrower.

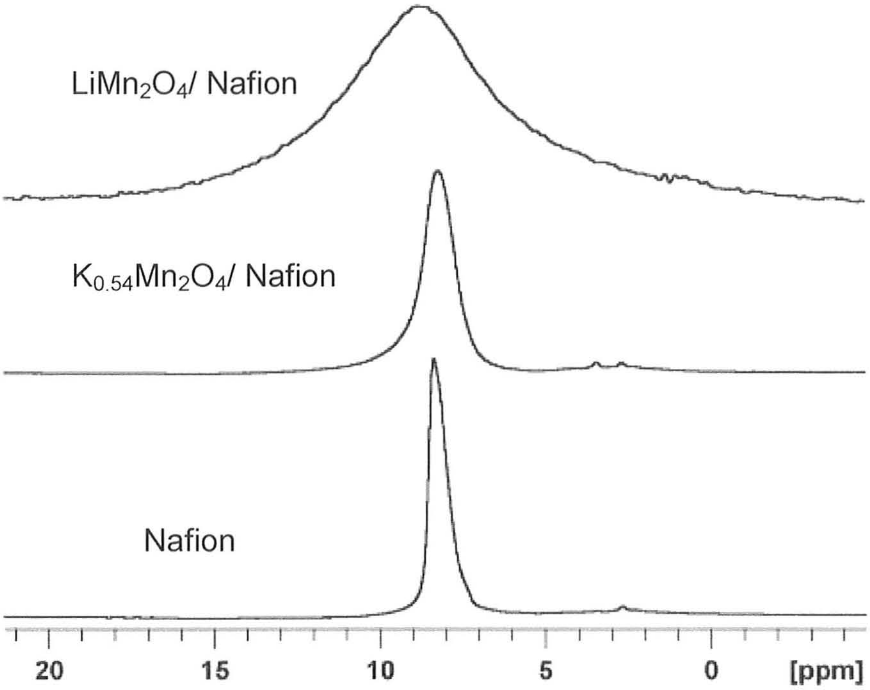

Figure 3-19. ^{1}H NMR of Nafion Membranes doped with: 0.5% $K0._{54}Mn_2O_4$ (middle) 0.5% $LiMn_2O_4$ (top) and pure Nafion (bottom).The peaks at 2 ppm are probe background. All the Nafion was Sulphuric acid wash before Fenton's test, ns= 32, pulse length= 2.5 μs, power level= 4.88 dB and delay time=3 s.

Table 3-5 Average oxidation and line width for $K_{0.54}Mn_2O_4$ and $LiMn_2O_4$.

Additives	Nafion	$LiMn_2O_4$	$K_{0.54}Mn_2O_4$
Average Oxidation state	0	3.5	3.75
Line width (Hz)	170	2600	520

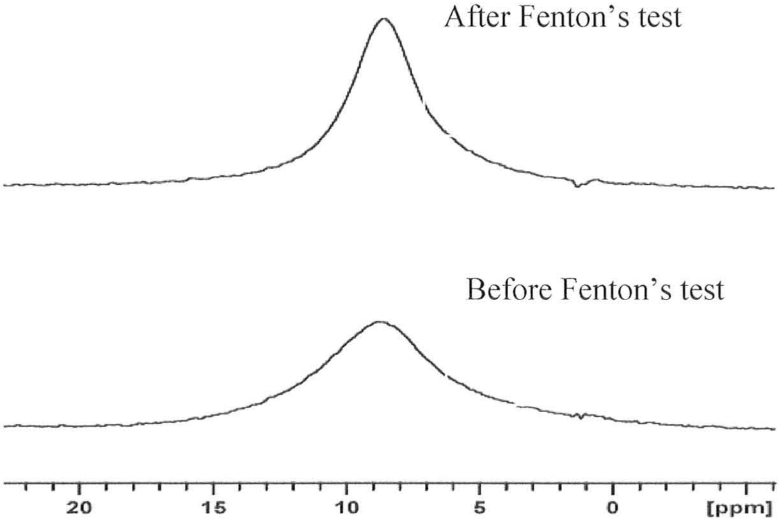

Figure 3-20. ^{1}H MAS NMR of Nafion membranes doped with 0.5% $LiMn_2O_4$ After free radical attack, FWHM is 1600 Hz. Before free radical attack, FWHM is 2700 Hz, ns= 32, pulse length= 2.5 μs, power level= 4.93 dB and delay time=3 s.

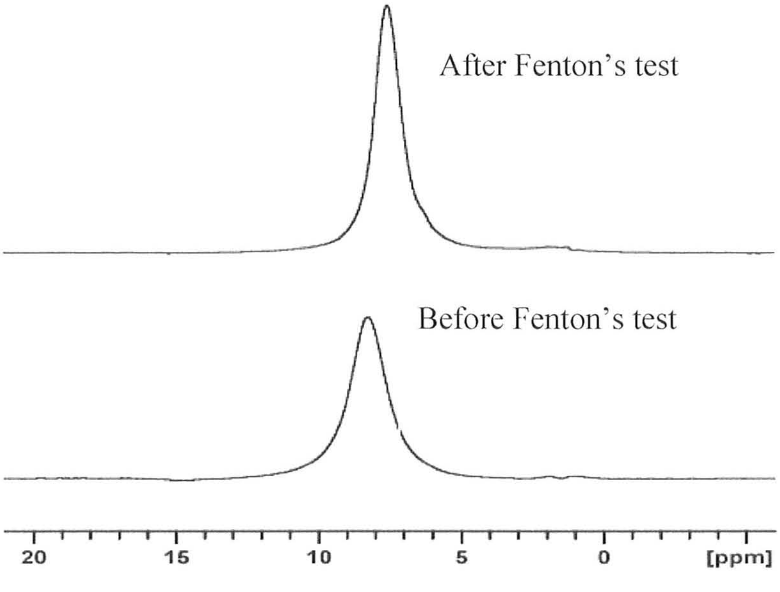

Figure 3-21. ^{1}H MAS NMR of Nafion Membranes doped with 0.5% $K_{0.54}Mn_2O_4$ After free radical attack, FWHM is 540 Hz. before free radical attack, FWHM is 760 Hz, ns= 32, pulse length= 2.5 μs, power level= 5.12 dB and delay time=3 s.

Figure 3-20 and 3-21 show the spectra before and after Fenton's test with different additives. An obvious trend that is observed is that Nafion, following Fenton's test, has a narrower peak. For example, $LiMn_2O_4$ Nafion undergoing Fenton's test obtains 1600 Hz at FWHM. When looking at $LiMn_2O_4$ Nafion without Fenton's test, the FWHM is 2700 Hz. A similar trend was observed in the $K_{0.54}Mn_2O_4$ Nafion composites. This trend can be explained by the reduction in the number of unpaired electrons following Fenton's test. The unpaired electron (Mn^{3+}:[Ar]$3d^4$) reacts with the hydroxyl radical. Less unpaired electrons (Mn^{4+} : [Ar]$3d^3$) exist in Nafion following Fenton's test. ($H^+ + Mn^{3+} + {\bullet}OH \rightarrow H_2O + Mn^{4+}$) The paramagnetic effect is proportional to the number of unpaired electrons. Therefore, the fewer the number of unpaired electrons, the weaker the paramagnetic effect. The narrower peak occurs with a weaker paramagnetic effect. Figure 3-22 shows the plot of $\ln(1/T_2^*)$ versus inverse temperature energy for three 0.5% $LiMn_2O_4$ Nafion composites (one before and two after Fenton's test). Energy barriers were determined using an Arrhenius analysis. The activation energy for Nafion undergoing free radical attack is 12 ±1 kJ/mol. This value is consistent with Nafion before free radical attack. It shows that proton mobility is not affected by free radical attack.

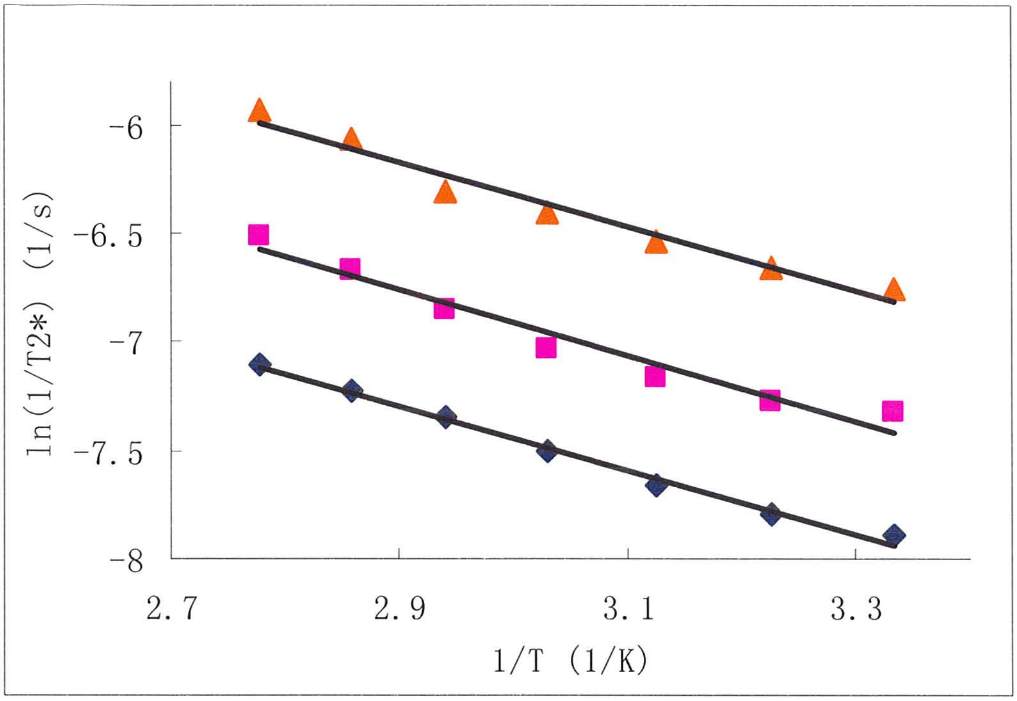

Figure 3-22. The activation energy from two dried 0.5% $LiMn_2O_4$ Nafioncomposites (before and after Fenton's test).

◆:0.5% $LiMn_2O_4$ Nafion composite before free radical attack, the activation energy is 12.3±0.5 kJ/mol.

■:Trial-1 for 0.5% $LiMn_2O_4$ Nafion composite after free radical attack, the activation energy is 12±1 kJ/mol.

▲:Trial-2 for 0.5% $LiMn_2O_4$ Nafion composite after free radical attack, the activation energy is 12±1 kJ/mol.

3.4 Conductivity test

From ^{19}F solution NMR studies, $LiMn_2O_4$ is a promising radical scavenger, which prevents Nafion from free radical attack. $LiMn_2O_4$ (0.5 Wt%) is so effective such that only minimal amounts are sufficient for excellent radical scavenging ability. However,

$LiMn_2O_4$ is not a good conductor (10^{-6} S cm^{-1}) which may reduce the Nafion conductivity. It is important to understand how the Nafion conductivity is impacted when the $LiMn_2O_4$ is present in the Nafion composites. Table 3-6 shows the conductivity data of $LiMn_2O_4$ Nafion composites was measured under different temperature when relative humidity was 95%. Compared with the pure Nafion [15, 16], the conductivity from $LiMn_2O_4$ Nafion composites do not drop by more than a magnitude. Therefore, $LiMn_2O_4$ can assume the role of radical scavenger and limit the negative impact on proton conductivity at low level of loading.

Table 3-6 Conductivity of $LiMn_2O_4$ Nafion composites under variable temperature, RH 95%

Temp (±2 °C)	**0.5 Wt % $LiMn_2O_4$ Nafion composites Conductivity (10^{-2} Scm^{-1})**	**Pure Nafion conductivity (10^{-2} Scm^{-1})**
35	**4.61± 0.25**	**6.8 [15]**
45	**5.98± 0.86**	
55	**7.41± 0.03**	
65	**9.10± 1.08**	**14.4 [16]**

3.5 Conclusion

Different free radicals are produced during the operation of fuel cells, which diminishes the lifetime and impacts efficiency of fuel cell. The goal of introducing additives (cerium oxide and manganese oxide) into Nafion is to achieve long operation time of fuel cell by avoiding free radical attack. The CeO_2 is able to protect Nafion but a high loading amount is necessary. Various manganese oxide nanoparticles do not provide good protection except the Nafion/ Mn_3O_4 particle preparation at 800 °C. In contrast, Nafion / Mn composite (700 °C) containing only Mn_3O_4 does not perform well. It can be concluded that better radical scavenger ability is attributed to the presence of the $K_{0.54}Mn_2O_4$ phase. The results show that free radical attack is prevented by the oxide with fewer unpaired electrons, counter to our original hypothesis from Table 3-2. Therefore, we propose a role for the hopping semiconductor, such as $K_{0.54}Mn_2O_4$ in which the $K_{0.54}Mn_2O_4$ may contribute delocalized electrons to react with free radical. The delocalized unpaired electrons pair up with the free radicals before Nafion degradation takes place. A method to prove this hypothesis is to prepare composite membrane using $K_{0.54}Mn_2O_4$ directly and $LiMn_2O_4$. $LiMn_2O_4$ is mixed valence compound and also well known as a hopping semiconductor which means that the electrons are capable of hopping between e_g orbital of manganese. The low loading of $K_{0.54}Mn_2O_4$ or $LiMn_2O_4$ are selected and presents good protection from free radical attack as characterized by ^{19}F NMR. The explanation is that all Mn ions are on octahedral site in $LiMn_2O_4$. In contrast, Mn_3O_4 is also mixed valence compound but there is no electron transfer between Mn^{3+} and Mn^{2+} because the different Manganese (Mn^{3+} and Mn^{2+}) ions are not on similar sites. Mn^{3+} ions are on octahedral sites and Mn^{2+} ions are on tetrahedral sites in Figure 3-23 [14]. Therefore, the average oxidation state of the manganese ions is not the primary driving force for good free-radical scavenging. Moreover, this data demonstrates the likely role of a surface-reaction at the particle-solvent interface, promoted by the electron-transfer within the oxides, rather than a simple dissolution of the metal ions into solution, followed by reaction with hydroxyl. These new finding enable us to explain the improved performance of the $LiMn_2O_4$ –Nafion composites over the lower oxidation state manganese oxides. The linewidth change following free radical attack in ^1H NMR indicates that the number of unpaired electrons decrease, which suggest the Mn^{3+} reacts with hydroxyl and is converted to Mn^{4+}.

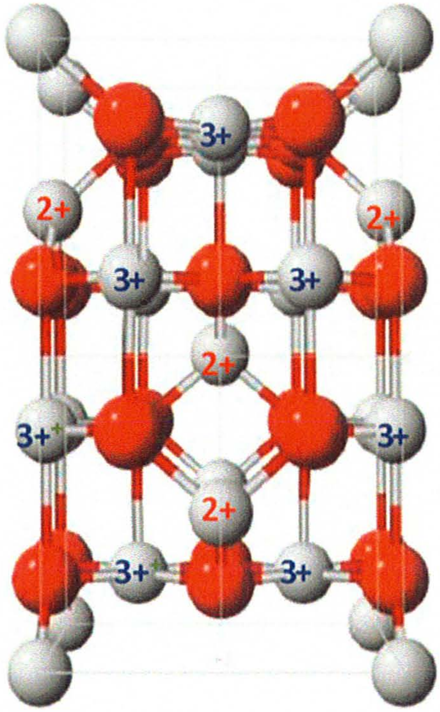

Figure 3-23 Structure of Mn_3O_4 [14]

^1H MAS variable temperature NMR experiments for Nafion $LiMn_2O_4$ composites reveals that the proton activation energy does not change following free radical attack. The proton remains the similar level of activation energy proves that the Nafion was protected by $LiMn_2O_4$. In addition, the $LiMn_2O_4$ does not have averse influence on Nafion conductivity.

3.5 References

1. S. Sathyamurthy, et al., Reverse micellar synthesis of cerium oxide nanoparticies. Nanotechnology, 2005. **16**(9): p. 1960-1964.

2. R.N. Reddy, R.G. Reddy, Synthesis and electrochemical characterization of amorphous MnO_2 electrochemical capacitor electrode material. Journal of Power Sources, 2004. **132**(1-2): p. 315-320.

3. Q. Feng, K. Yanagisawa, and N. Yamasaki, Synthesis of birnessite-type potassium manganese oxide. Journal of Materials Science Letters, 1997. **16**(2): p. 110-112.

4. Healy, J., et al., Aspects of the chemical degradation of PFSA ionomers used in PEM fuel cells. Fuel Cells, 2005. **5**(2): p. 302-308.

5. S.Kundu, L.C.S., M.W. Fowler, Comparison of two accelerated Nafion degradation experiments. Polymer Degradation and Stability, 2008. **93**: p. 214.

6. W.C. Schumb, C.N.S., R.L. Wentworth, Hydrogen Peroxide,American Chemical Society Monograph Series. 1955: p. 492.

7. E. Endoh, Development of Highly Durable PFSA Membrane and MEA for PEMFC Under High Temperature and Low Humidity Conditions ECS Transactions, 2008. **16**(2): p. 1229-1240.

8. S. Deshpande, et al., Size dependency variation in lattice parameter and valency states in nanocrystalline cerium oxide. Applied Physics Letters, 2005. **87**(13).

9. Feng Zhang, S.W.C., Jonathan E. Spanier, Ebru Apak, Qiang Jin, and a.I.P.H. Richard D. Robinson, Cerium oxide nanoparticles: Size-selective formation and structure analysis. APPLIED PHYSICS LETTERS, 2001. **80**: p. 127-129.

10. N.R.Andrews, S.D.K., K.A. Murray, S.J. Mcdermid,S.M. Mackinnon, S. Ye,, Reduced Degradation of ion-Exchange Membranes in Electrochemical Fuel Cells, B.P.S. Inc, Editor. 2003.

11. H. Kawazoe, Liquid composition. Method for producing same, and method for producing a membrane electrode assembly for a solid polymer fuel cell, A.G. company, Editor. 2005: United States of America.

12. G. Wakefield, et al., Metal Oxide Particles Useful As Free Radical Scavengers In Sunscreen And Cosmetic Compositions, O. LTD, Editor. 2005: UK.

13. C.P. Grey, N.D., NMR Studies of Cathode Material for Lithium-Ion Rechargeable batteries. Chem. Rev, 2004. **104**: p. 4493.

14. A. J. Moulson, J.M.H., Electroceramics: materials, properties, applications. 2 ed. 2003: John Wiley and Sons.

15. K. M. Nouel and P. S. Fedkiw, Electrochim. Acta, **43**, 2381 (1998)

16. A. V. Anantaraman and C. L. Gardner, J. Electroanal. Chem., **414**, 115 (1996).

Chapter 4

Studying the Influence of Doping PWA/ SiO_2 Inorganic Materials into Nafion Using Solid-State NMR

This chapter describes sample preparation of different PWA SiO_2 particles and the in-situ/ex situ Nafion PWA SiO_2 composites, and data acquisition procedures by NMR, and FTIR. Firstly, the local proton environment of different PWA Nafion composites was probed by ^1H MAS NMR. The presence of phosphotungstic acid in PWA SiO_2/ Nafion has been studied using ^{31}P solution state NMR and FTIR. Proton dynamic information is determined not only by high resolution solid state NMR under variable temperature conditions but also by different pulse sequences - Back-to-Back, EXSY and Selectively Inversion experiment for Nafion composites.

4.1 Introduction

A proton exchange membrane fuel cell is a promising, environment friendly energy source. The lower operating temperature of fuel cells however, limits its performance. Higher operating temperature is preferred in order to increase electrode kinetics and to decrease the CO poisoning on Pt electrode. The presence of carbon monoxide reduces the efficiency of fuel cell by deactivation of the Pt catalyst. However, the consequence of high operating temperature is that the water uptake of Nafion dramatically decreases. The performance of Nafion is impaired under low relative humidity. Adding various hydrolytic inorganic materials is a strategy used to address these difficulties. Recently, 12-phosphotungstic acid (PWA), a heteropolyacid, has been attracting attention due to its high proton conductivity. In the structural single unit (keggin-type), a central PO_4 is surrounded by 12 edge sharing WO_6 units. The negative charge in the PWA structure is neutralized by three protons. PWA/ SiO_2 particles are used as additives in this research. Under anhydrous condition, the Grotthuss mechanism dominates the proton transportation. Even proton conductivity of heteropolyacids is dependent on the degree of hydration [1]. The protons from PWA surface may hop between PWA and SO_3H groups [2]. In the PWA-Nafion composites, the movement of the protons at the interface between PWA and SO_3H contributes to high proton conductivity at relative low humidity environment. It attributes to the three protons from PWA and absorbed water molecular at PWA surface. The PWA with multiple protons is introduced into Nafion, which has been shown proved to enhance the Nafion conductivity [3]. The transportation between the Nafion proton s and protons from PWA SiO_2 or PWA is probed by solid state NMR. The exchange reaction is observed by 2D EXSY and selective-inversion experiments.

4.2 Experimental

4.2.1 Sample Preparation

The methods to synthesize PWA SiO_2 Nafion and PWA SiO_2 Nafion are described in this section.

4.2.1.1 Preparation of Nafion/PWA Composites

The pretreated Nafion membrane 112 was used to prepare PWA Nafion composites. The Nafion 112 has the equivalent weight (EW): 1100 g/mol and its thickness is 0.002 in. The purified Nafion membrane 112 were swollen in a 10 ml $V_{MeOH}:V_{water}$ solution (1:1) for 24 hrs at 80 °C. These swollen Nafion membranes were placed in solutions with different 12-Phosphotungstic acid concentration (0.1 M, 0.01 M and 0.001 M) to allow PWA to permeate into the Nafion membrane.

Another Nafion PWA composite was prepared by adding 12-Phosphotungstic acid particles directly into the Nafion solution with weight percentages of either 10 wt%, 20 wt% or 30 wt %. These PWA Nafion solutions were poured into a petri dish where they stabilized at 105 °C in the oven for 8 hours.

4.2.1.2 Preparation of PWA SiO_2 and Nafion/PWA SiO_2 Composites

A mixture of 2 ml TEOS, 4.7 ml water and 0.1 M HCl was added into the 1 ml PWA solution (TEOS/PWA mole ratio= 40) [4]. The solution was stirred overnight at 80 °C, allowing the PWA SiO_2 particles to form. The PWA SiO_2 particles were then blended with a Nafion solution and were sonicated for several hours until the particles were distribute evenly in the Nafion solution. The PWA SiO_2 Nafion solution was then poured into a petri dish which stabilized at 105 °C over 8 hours. The Nafion membrane composites did not require further purification.

4.2.1.3 Preparation of in-situ and ex-situ PWA/SiO_2 Nafion Composites

The *ex-situ* PWA/SiO_2 Nafion were prepared by adding the PWA SiO_2 particles from section 4.2.1.2 to the Nafion solution and sonicated for several hours until the particles were well distributed in the Nafion solution. The PWA-Nafion solution was poured into a petri dish which stabilized at 105 °C over an 8 hour period. The formed Nafion membrane then went through the Nafion purification process.

The *in-situ* PWA SiO_2 Nafion was prepared by mixing PWA particles with a TEOS solution. The well stirred PWA/TEOS solution was mixed with Nafion solution and the Nafion solution was poured into a petri dish which stabilized at 105 °C in the oven for 8 hours to form the Nafion membrane composite. The formed Nafion membrane composite was then subjected to Nafion purification.

4.2.1.4. Nafion/ PWA SiO_2 –Butanol membrane

A mixture of water (2.0 mol), 1-butanol (0.2 mol) and $H_3PW_{12}O_{40}$ ($5x10^{-4}$ mol) was added into Si $(OC_2H_5)_4$ (0.2 mol), and stirred at 80 °C for 3 hrs (TEOS/PWA mole ratio = 400). The solution was dried at 80 for 48 hours leading to the formation of the PWA SiO_2 particles. A given amount of PWA/SiO_2 particles were added to the Nafion solution which was then sonicated for several hours until the particles were distributed into the Nafion solution. The PWA Nafion solution was then poured into a petri dish which stabilized at 105 °C in the oven for 8 hours. The newly formed Nafion membrane composites are now denoted as Nafion/ PWA SiO_2 –butanol.

4.2.1.5 Nafion purification

The Nafion membrane was first washed in DI water for 1 hour and then washed in boiling 3 % hydrogen peroxide solution for 1 hour in order to remove the metals and other organic impurities. The Nafion was then washed in water for another hour, during which time the water was refreshed three times. Subsequently, the Nafion was washed in 1M H_2SO_4 solution. Finally, the acid form Nafion was washed repeatedly in DI water until the residual H_2SO_4 was removed.

4.2.2 NMR Spectroscopy

All NMR experiments were performed at 500.13 MHz for ^1H MAS NMR and 202 MHz for ^{31}P solution state NMR. ^1H MAS NMR spectra were acquired under MAS conditions (25 kHz) with a 2.5 mm HX probe.

4.2.2.1 ^{1}H MAS NMR

^{1}H solid state NMR experiments were executed on a Bruker AV 500 spectrometer at a ^{1}H Larmor frequency of 500.13 MHz. A 2.5 mm diameter ZrO_2 rotor was used for Nafion samples spun at 25 kHz. A recycle delay of 2 s and a pre-scan delay of 4.5 μs were used. The spectra were referenced to adamantane (1.63 ppm for ^{1}H). Solid state ^{1}H NMR spectra were acquired with a 90° pulse length of 2.5 μs. ^{1}H MAS NMR variable temperature experiments were carried out over a temperature range of 300 K to 370 K. The rotor-synchronized double quantum filter (DQF) MAS spectra were recorded by using Back-Back (BaBa) pulse sequence with τ equal to one rotor period with the number of scans equal to 32. ^{1}H 2D EXSY NMR spectra were record by EXSY pulse sequence with mixing time range of 1 ms to 150 ms. The selective-inversion experiments (SI) were performed using a $\pi/2$-τ-$\pi/2$ excitation sequence. The transmitter frequency was placed on the resonance of the major sites. The value of τ is set as the half of the frequency difference between two exchange sites $1/2(\Delta V_{AB})$. Data were collected within mixing time from 1 ms to 250ms.

4.2.2.2 ^{31}P NMR

^{31}P solution state NMR experiments were performed on a Bruker DRX500 spectrometer at a ^{31}P Larmor frequency of 202.47 MHz. ^{31}P NMR spectra were acquired with a 90° pulse length of 4.1 μs, and referenced to 85% H_3PO_4 (0 ppm for ^{31}P NMR). The number of scans used was 128.

^{31}P-^{1}H heteronuclear correlation (HECTOR) NMR experiments were performed on a Bruker AV500 spectrometer to determine the correlation between phosphorus and the proton. The number of slices in the indirect dimension was 256 with 32 scans.

4.2.3. FTIR

Infrared absorption spectra were recorded on Bio- Rad FTS-40 Fourier transform IR spectrometer with a resolution of 4 cm^{-1} between 4000-400 cm^{-1}. The powder and membrane were ground into fine powder with KBr.

4.2.4 Impedance Spectroscopy for proton conductivity measurement

Measurements were taken on an AUTOLAB PGSTAT30 impedance analyzer and a BekkTech four-probe conductivity cell with two platinum mesh outer electrodes and two platinum wire inner electrodes. The instrument was used in potentiostatic mode with AC potential amplitude of 0.01 V. A frequency range of 10000 Hz to 10 Hz is chosen. The potential is 0.5 V. The hydrated membranes were placed in to the four–probe conductivity cell and then reaching the equilibrium of desired temperature and humidity by keeping the cell in a humidity chamber for at least 4 hours. For the dried samples, membranes were dried at 105 ^{o}C overnight before measuring. The thickness of membranes was measured by a micrometer at different level of humidity.

4.3 Results and Discussion

4.3.1 PWA Nafion membrane

4.3.1.1PWA Nafion membrane made from Nafion membrane 112

The pure Nafion 112 membranes were immersed into different concentrations of PWA solutions (0.1 M, 0.01 M, and 0.001 M). The local proton environment of the PWA Nafion membrane was probed by ^{1}H MAS NMR technique. The peak at 7.1 ppm in the proton spectrum is the only resonance recorded in Figure 4-1. It implies that only one proton environment exists in the PWA Nafion membrane. PWA and Nafion both carry protons in different proton environments. Therefore, the single resonance observed can be interpreted as a result of the uniform distribution of PWA or fast exchange among enviroment in the Nafion membrane. The existence of the Nafion-H_2^+ state is due to the rapid proton exchange between Nafion-H and PWA-H. The spectra from the Nafion in different solutions of varying PWA concentrations show a trend of line narrowing with increasing PWA concentration. The Nafion with the highest concentration of PWA (0.1 M) shows the narrowest line width, which is attributed to weak dipole coupling. This result is shown in Figure 4-1 and indicates that the corresponding protons in this sample are relative more mobile. The trend of narrowing line widths with increasing PWA content is evidence of PWA facilitating proton transport. Nafion with low PWA content shows comparatively broad lines.

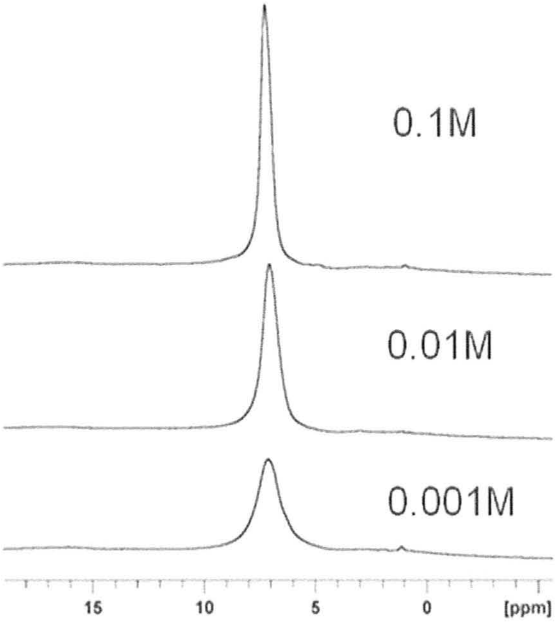

Figure 4-1 ^{1}H MAS NMR for Nafion 112 dried overnight at 105 °C following immersion in different concentrations of PWA solutions, (0.1M, 0.01M and 0.001M), MAS=25 kHz, ns=32, pulse length=2.5 μs, power level=6.0 dB and delay time=2 s.

Information about proton activation energy is measured using variable temperature ^{1}H experiments, which are presented in Fig 4-2. Figure 4-2 (a) shows a series ^{1}H MAS NMR spectrum recorded from the dried Nafion composite at different temperatures. The temperature range is from 300-360 K. High temperature leads to a fast proton exchange rate between the sulfonic acid groups or the adjacent water molecules and narrower peaks. The same trend was also observed for the Nafion PWA composite in Figure 4-2 (b) and Figure 4-2 (c).

Figure 4-3 and Table 4-1 shows that the lowest activation energy (3.7 kJ/mol) comes from the Nafion immersed in 0.1 M PWA solution while the highest activation energy is acquired from the Nafion immersed in 0.001 M PWA solution. The proton dynamic results are consistent with the observation of the change in line width of Nafion PWA composites in Figure 4-1. The enhancement of proton mobility with the addition of PWA into Nafion is confirmed by ^{1}H MAS NMR.

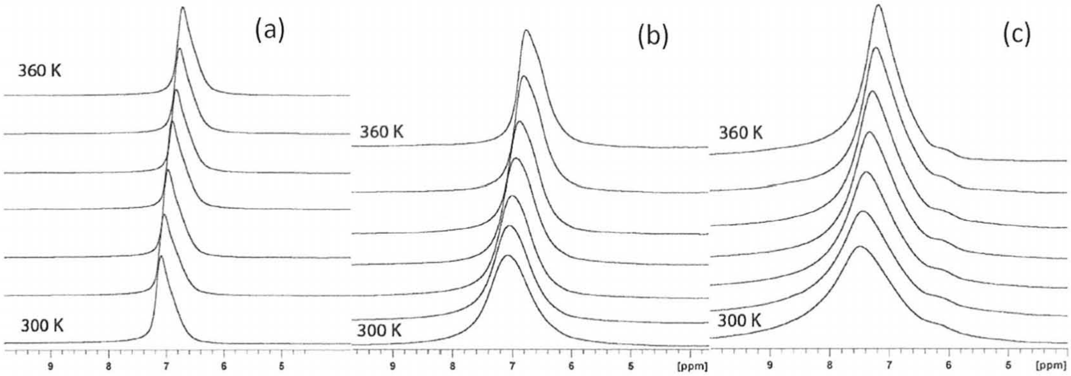

Figure 4-2 Dependence of the T_2* on temperature for fitting activation energy of Nafion PWA membranes (a) Nafion 112 (0.1M PWA) (b) Nafion 112 (0.01M) (c) Nafion 112 (0.001M), MAS=25 kHz, ns=32, pulse length=2.5 μs, power level= 6.0 to 6.4 dB and delay time=2s.

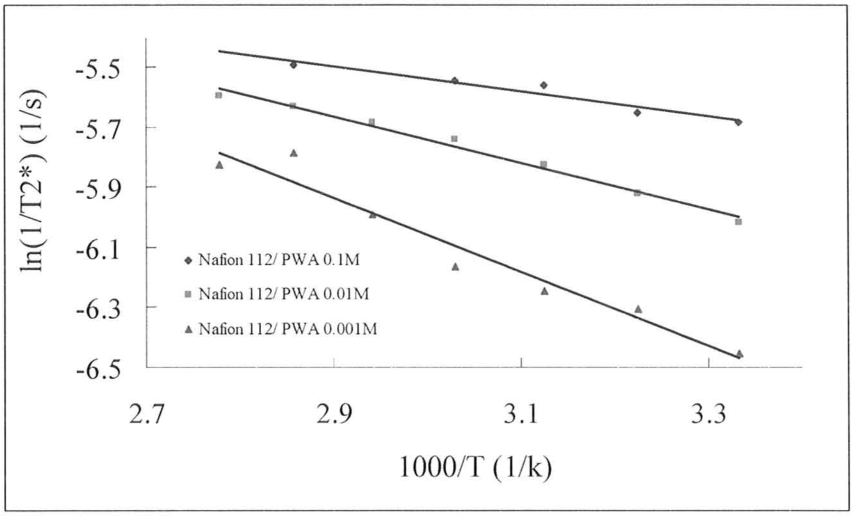

Fig 4-3 Dependence of T_2* on the temperature for fitting activation energy of Nafion 112/ PWA composites. The T_2* was calculated from the Figure 4-2. From the plot of T_2* versus temperature, the activation energy of the Nafion-H dynamic is 3.7 ± 0.6 kJ/mol, 6.4 ± 0.3 kJ/mol and 10.21 ± 1.3 kJ/mol for 0.1M, 0.01M and 0.001M respectively.

Table 4-1 Activation energies of proton transport in Nafion 112/PWA composites

Nafion composite	**Nafion (0.1 M)**	**Nafion (0.01 M)**	**Nafion (0.001 M)**
Ea (kJ/mol)	**3.7 ± 0.6**	**6.4 ± 0.3**	**10.8 ± 1.3**

In Table 4-2, the highest conductivity comes from Nafion PWA (0.1 M). The conductivity of Nafion can be improved with higher content of PWA. The conductivity of Nafion PWA (0.1 M) is 2-3 times higher than the conductivity of Nafion at relative humidity range of 30-90%.

Table 4-2 Conductivities of the PWA Nafion composites with varying [PWA] under different level of humidity

	Conductivity of PWA Nafion Composites (S cm^{-1})	
RH (%)	**0 M PWA**	**0.1 M PWA**
0	**Not measured**	**$2.7 \times 10^{-4} \pm 0.8 \times 10^{-4}$**
30	**$2.4 \times 10^{-3} \pm 1.0 \times 10^{-3}$**	**$6.0 \times 10^{-3} \pm 0.6 \times 10^{-3}$**
60	**$1.8 \times 10^{-2} \pm 0.3 \times 10^{-2}$**	**$4.3 \times 10^{-2} \pm 1.1 \times 10^{-2}$**
90	**$0.6 \times 10^{-1} \pm 0.01 \times 10^{-1}$**	**$1.6 \times 10^{-1} \pm 0.2 \times 10^{-1}$**

4.3.1.2 Nafion solution blend with different amount of PWA particles

Another PWA Nafion membrane is made by blending the Nafion solution into different amounts of PWA particles. A similar trend is also observed in the Nafion membranes shown in Figure 4-4. The Nafion membrane with the higher amount of PWA shows a narrow peak while the Nafion membrane with a lower amount of PWA has a broader peak. It is interesting to note that a shoulder appears in the ^{1}H MAS NMR spectra of Nafion/ PWA 30 %. This may be interpreted as the possible presence of excess isolated PWA.

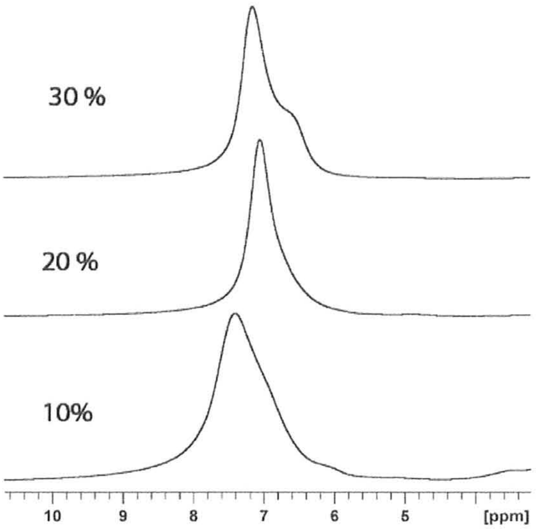

Figure 4-4 ^{1}H MAS NMR spectra for Nafion /PWA at various PWA composites dried at 105 °C overnight. A shoulder appears from the Nafion with the highest amount of PWA may belong to the excess PWA proton, MAS=25 kHz, ns=32, pulse length=2.5 μs, power level= 6.6 dB and delay time=2 s.

4.3.2 PWA SiO_2 particles and PWASiO_2 membrane

4.3.2.1 PWA SiO_2 particles

Figures 4-5 and 4-6 show the ^{1}H and ^{31}P NMR spectra of PWA/SiO_2 particles. The ^{1}H spectrum shows that there are two proton sites (6.4 ppm and 2.3 ppm) from the PWA SiO_2 particles. The ^{31}P spectrum consists of one peak at -14.9 ppm, related to the hydrated PWA molecule [5, 6]. The peak at -14.9 ppm also indicates the homogeneous distribution of PWA in SiO_2 particles and the presence of the Keggin structure.

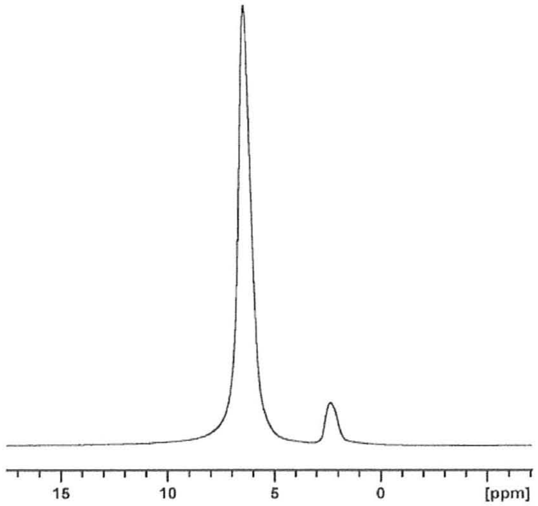

Figure 4-5 ^{1}H MAS NMR spectrum under for PWA SiO_2 particles, MAS=25 kHz, ns=32, pulse length=3.5 μs, power level=4.8 dB and delay time=2 s.

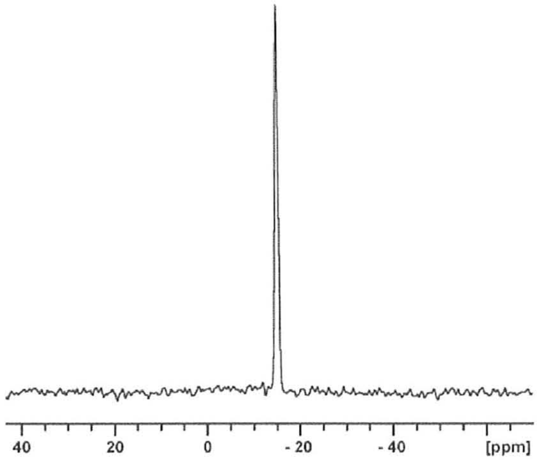

Figure 4-6 ^{31}P MAS NMR spectrum for PWA SiO_2 particles, MAS=25 kHz, ns=1k, pulse length=4.1 μs, power level=3.0 dB and delay time=5 s.

By acquiring dipolar coupling between the two proton sites and the central phosphorus in the Keggin structure, useful information is provided. For example, we are able to distinguish the phosphotungstic protons from the possible OH groups in the SiO_2 surface. The ^{31}P-^{1}H correlation experiment is applied to obtain this information. The spectrum is shown in the Figure 4-7. Both proton sites have dipolar coupling with the phosphorus nuclei in the PWA. The proton at 6.4 ppm has stronger dipolar coupling which indicates the greater proximity to the phosphorus atom. Therefore, the peak is assigned to the phosphotungstic acid proton. The proton at 2.3 ppm may represent the OH group from the SiO_2 surface, which is relatively far from the central phosphorus of the Keggin structure. The Back–to-Back pulse [7] sequence is used to study the proton mobility. Compared to the spectrum from the regular MAS experiment, a clear contrast was observed. The peak which represents the phosphotungstic proton disappears from the DQF MAS NMR spectrum in Figure 4-8. The resonances with weak dipolar couplings are not observed in DQF MAS NMR spectra. Therefore, phosphotungstic proton (6.4 ppm) is relatively mobile.

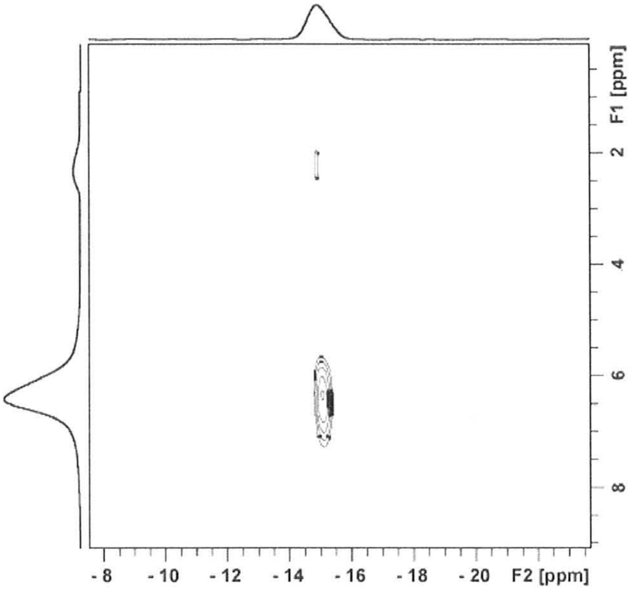

Figure 4-7 ^{31}P-^{1}H HECTCOR NMR for PWA/SiO_2particles, MAS=25 kHz, contact time= 3 ms.

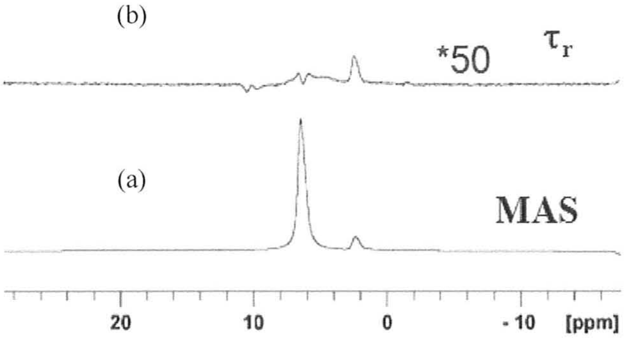

Figure 4-8 ^{1}H MAS NMR of the PWA/SiO_2 (a) MAS (b) DQF, MAS=25 kHz, ns=32, pulse length=3.5 μs, power level=4.8 dB and delay time=2 s.

The proton activation energy is evaluated using ^{1}H NMR variable temperature experiments. The results are shown in Figure 4-9 and Figure 4-10, which are analyzed using the Arrhenius equation. The activation energy of the mobile phosphotungstic acid proton is 3.6 ± 0.1 kJ/mol. The PWA proton is still mobile after blending with the SiO_2 matrix. This is indicative of that PWA proton remains conductive within SiO_2 framework.

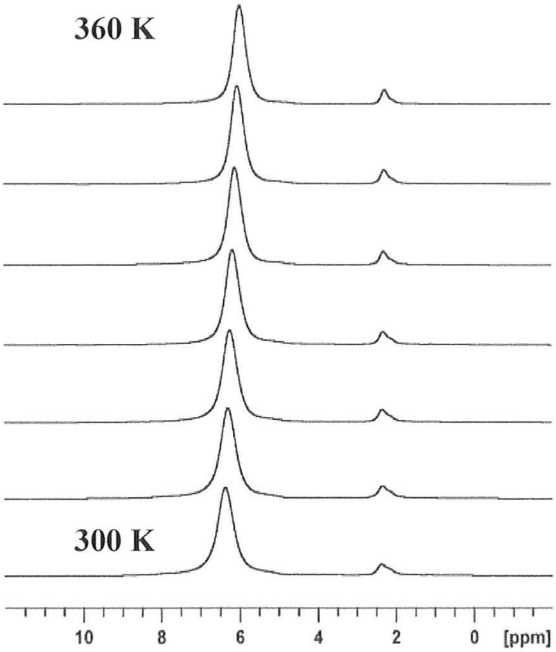

Figure 4-9 ^{1}H MAS NMR of PWA/SiO_2 over a variable temperature range of 300 to 360 K, MAS=25 kHz, ns=32, pulse length=2.5 μs, power level=5.25 dB, delay time=2 s.

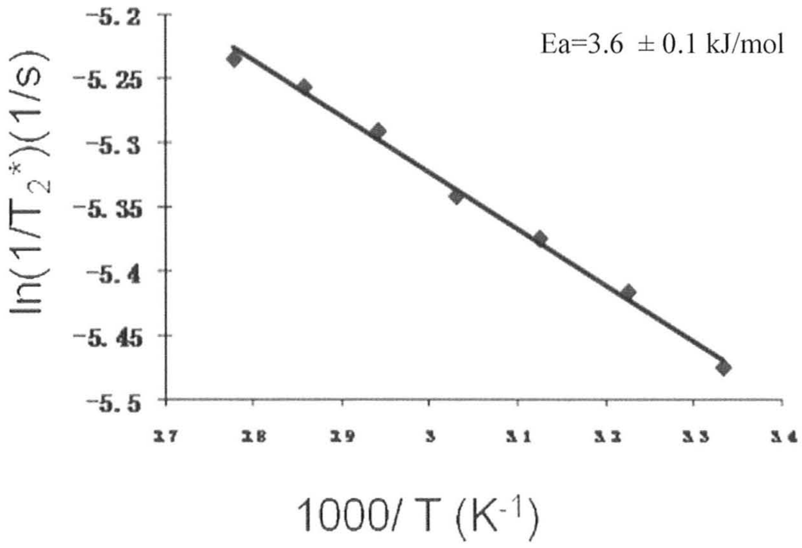

Figure 4-10 Dependence of T_2* on the temperaturefor fitting activation energy of PWA/SiO_2 particles

4.3.2.2PWA SiO_2 Nafion composites

^{1}H MAS NMR spectrum is shown in Figure 4-11 where two proton sites are observed. The signal (7.5 ppm) at higher frequency corresponds to sulfonic acid proton and the signal (4.8 ppm) at low frequency is related to phosphotungstic acid proton. The cross peaks between two acid protons in Figure 4-12 result from chemical exchange between the two proton sites. The exchange of two different protons is observed as cross peak in 2D EXSY spectra at a mixing time of 10 ms. Due to the short T_1 value of the sulfonic acid proton, the evolution of the cross peak intensity as a function of mixing time is limited meaning that rate information cannot be determined through use of EXSY experiments. In order to determine the timescales of proton exchange, Selectively-inversion experiments (SI) were applied.

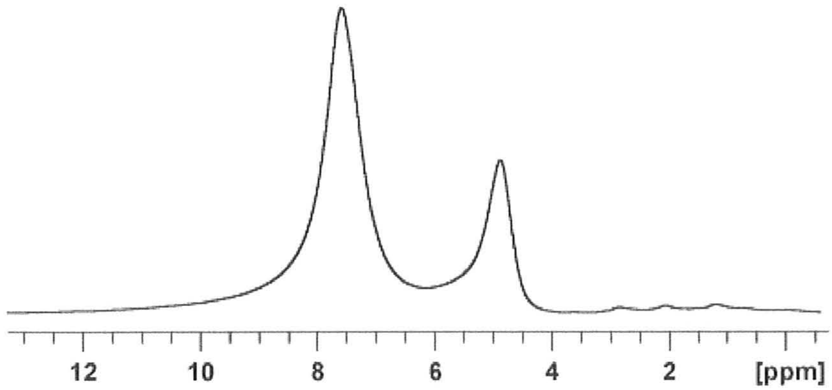

Figure 4-11 ^{1}H MAS NMR for PWA SiO$_2$ Nafion composites, MAS=25 kHz, ns=32, pulse length=2.5 μs, power level=6.6 dB, delay time=2 s.

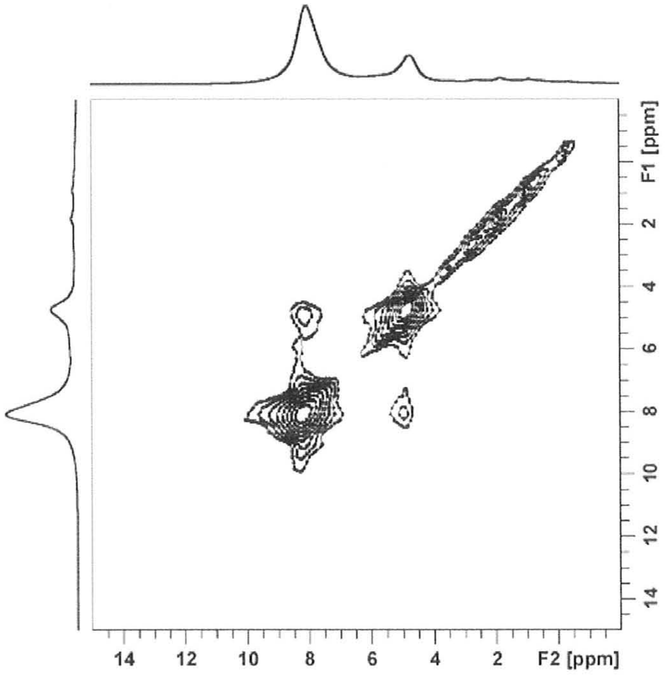

Figure 4-12 ^{1}H EXSY NMR for PWA/SiO$_2$ Nafion Composites, MAS=25 kHz, mixing time is 10 ms and 300 K.

The series of results of 1D selectively inverted experiment with varying mixing time are shown in Figure 4-13. In Figure 4-13, the proton at high frequency is chosen as the site to be selectively inverted which was achieved by placing the transmitter frequency on-resonance to this site. The magnetization of the proton can relax back to equilibrium through both inherent relaxation properties or by chemical exchange with the non-inverted proton resonance at low frequency [8].

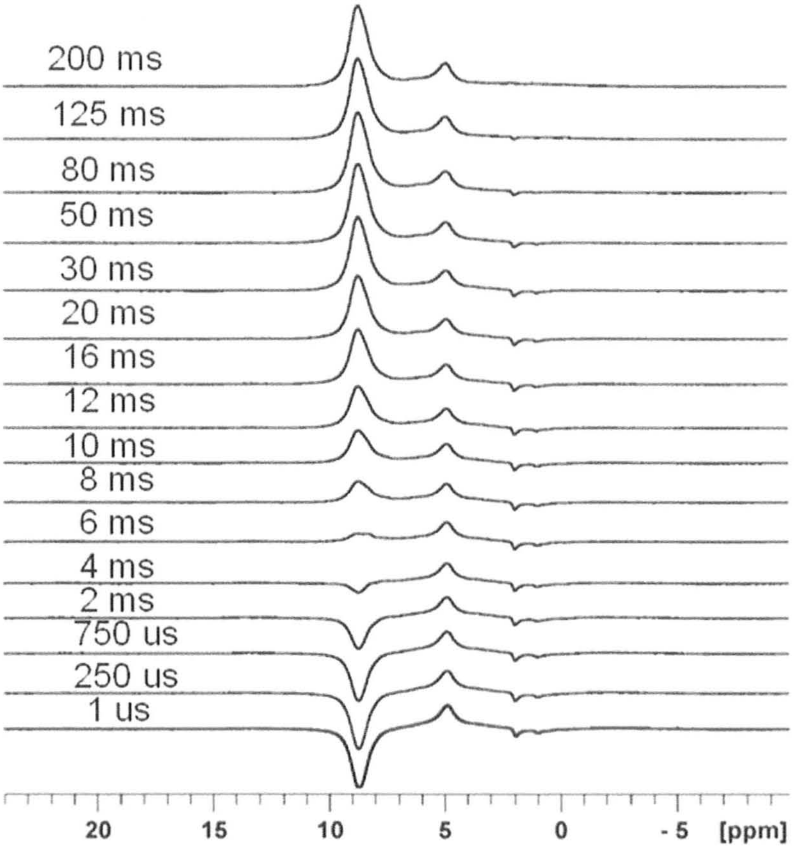

Figure 4-13 Selectively inverted experiment, MAS=25 kHz, ns=32, pulse length=2.5 μs, power level=6.6 dB, delay time=2 s and 300 K.

If there is direct exchange reaction between two sites, the initial slope of the non-inverted peak should be considerably steep. This phenomenon is observed in the Figure 4-14 at different temperatures, which confirms the exchange taking place between the two proton resonances presents. However, the unresolved background signal at the transient peak prevent determine the exchange rate from CIFIT program [9].

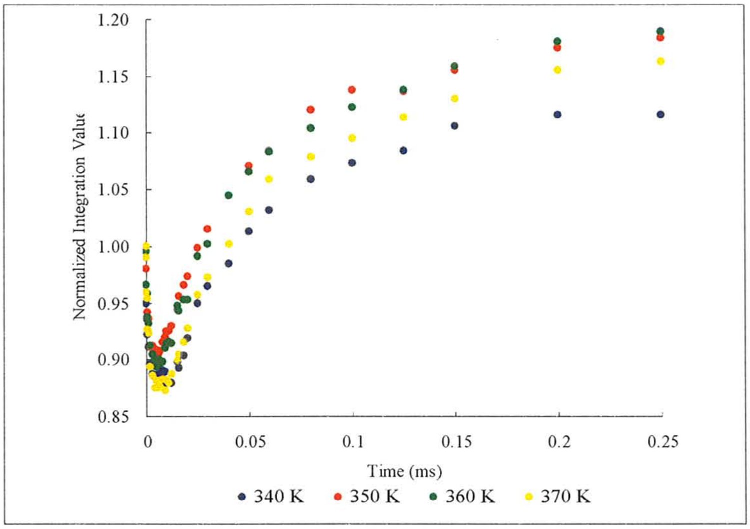

Figure 4-14 Relative intensity of selectively inverted transient peak asfunction of time under variable temperatures

Moreover, combinations of the non-selective-inversion and selective inversion can provide the visible view of the proton exchange by comparing the relative intensity change as a function of temperature. In Figure 4-15, the non-selective inversion studies (regular T_1 variable temperature experiments) show that relative intensity of the peak is independent of temperature change. In the contrast, the selective inversion studies show that relative peak intensity of the inverted resonance is dependent on temperature. This difference in the observation from the selective-inversion studies is attributed to the thermodynamic proton exchange between sulfonic acid proton and phosphotungstic acid.

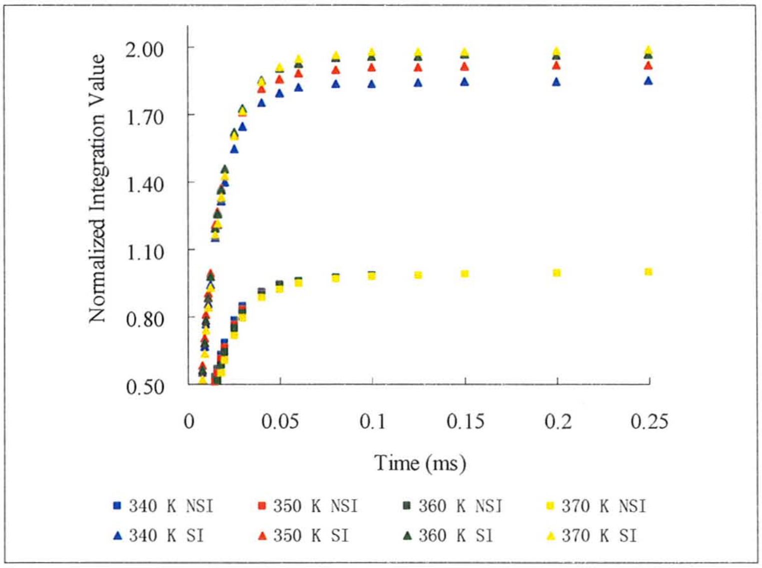

Fig 4-15 Variable Temperature SI (Selective-Inversion) and NSI (Non Selective Inversion). The triangles correspond to SI, and the squares to the NSI.

4.3.3 Ex-situ and In-situ Nafion membrane (purified)

A series of ^1H MAS NMR spectra of *ex-situ* PWA/SiO_2 is shown in Figure 4-16. The spectrum is taken as a function of temperature between 300-360 K. The low frequency proton resonance shown in Figure 4-16 is assigned to the presence of residual TEOS, owing to the incomplete hydrolysis reaction [10]. The chemical shift appears to be temperature dependent as it moves to lower frequency as the temperature is increased. The activation energy for proton dynamics is established by fitting the built-up curve as a function of temperature in Figure 4-17. The activation energy of the Nafion proton at 7.5 ppm is 10.0 ± 0.1 kJ/mol. However, the activation energy of the Nafion proton from the *in-situ* PWA/SiO_2 Nafion composites is reduced to 4.8 ± 0.2 kJ/mol in Figure 4-20 and Table 4-3. The reason for the reduction of activation energy is related to the presence of Si-C_2H_5 from the unfinished TEOS hydrolysis reaction.

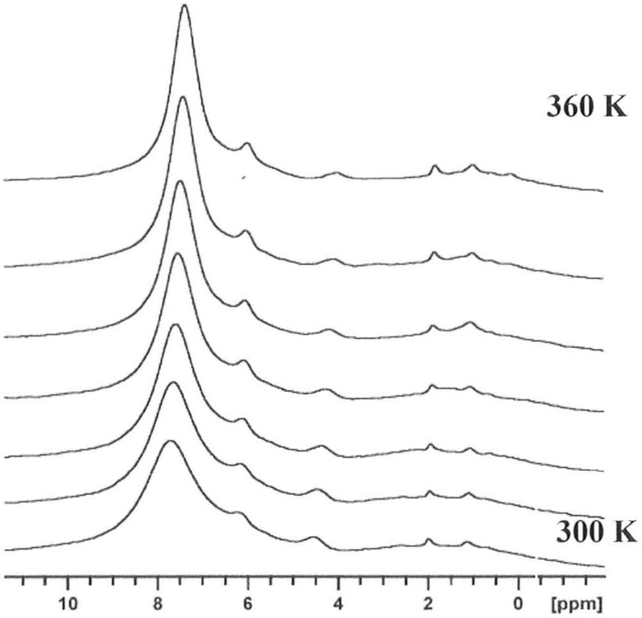

Figure 4 -16 ^{1}H MAS NMR spectra for ex situ PWA/SiO_2 Nafion composite under various temperatures, MAS=25 kHz, ns=32, pulse length=2.5 μs, power level=5.25 dB, delay time=2 s.

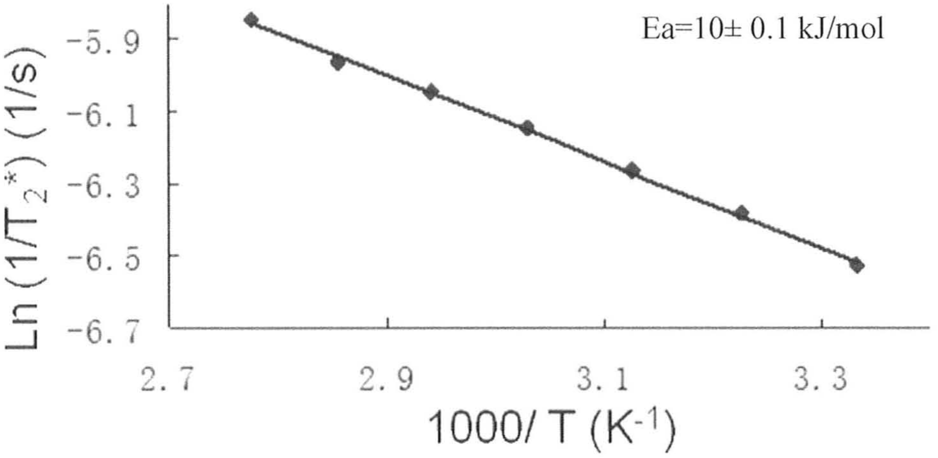

Figure 4-17 Dependence of T_2* on the temperature for fitting activation energy of ex-situ PWA/SiO_2 Nafion composites

Table 4- 3 Activation energies of proton transport for in-situ and ex-situ PWA SiO_2/Nafion conposites

Nafion composites	Ex-situ	In-situ
E_a (kJ/mol)	10.1± 0.1	4.8± 0.2

The presence of the ethyl group hinders proton transport as shown in Figure 4-18 The pathway of proton movement is spatially blocked by ethyl groups. Therefore, higher activation energy is required to carry out proton transport in this case.

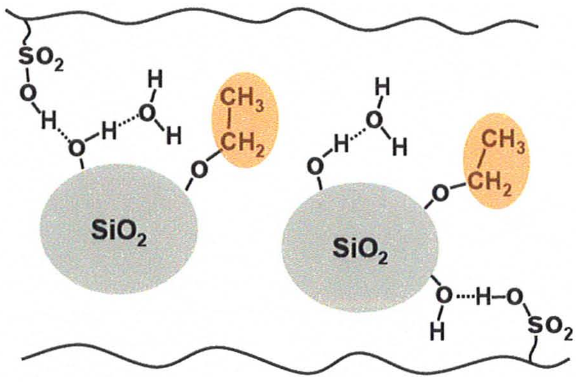

Figure 4-18 Schematic representation of the structure of PWA SiO_2/ Nafion composite prepared from the ex-situ method [10].

Figure 4-19 shows that proton resonance from the Si-C_2H_5 group is not observed at low frequency. This is indicative of the absence of ethyl groups in the *in-situ* PWA SiO_2 Nafion composites, which is due to TEOS being completely hydrolyzed. All ethyl groups from the TEOS reacted with OH during the hydrolysis reaction. Therefore, the SiO_2 particles are bonded to these OH groups. Without the presence of ethyl groups, protons are easily transported to other proton sites. The required activation energy of *in-situ* is therefore decreased.

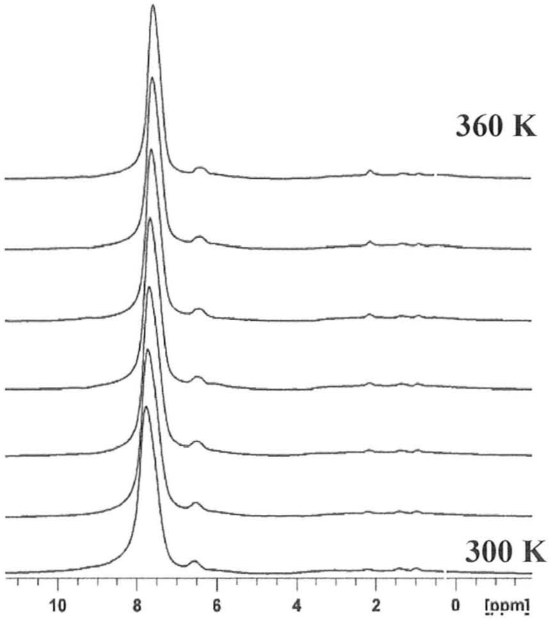

Figure 4 -19 ^1H MAS NMR spectra for in-situ PWA/SiO_2 Nafion composites over a variable temperature range, MAS=25 kHz, ns=32, pulse length=2.5 μs, power level=6.3 dB, delay time=2 s.

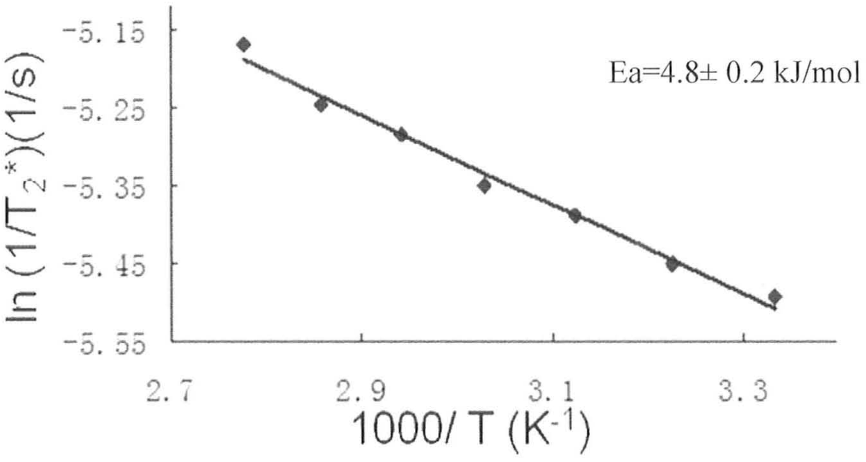

Figure 4-20 Dependence of T_2* on temperature for fitting activation energy of *ex-situ* PWA/SiO_2 Nafion composites

In Figure 4-16 and Figure 4-19, the main proton resonance at high frequency is assigned to sulfonic acid from the Nafion. The proton resonance from phosphotungstic acid is missing in both spectra. The waste water that was produced from the purification and rinsing of *ex-situ* and *in-situ* PWASiO_2/ Nafion composites was collected to investigate the possible leaching of PWA from the Nafion composites. ^{31}P solution state NMR was used to analyze the waste water. Pure PWA solution is used as a reference standard. The data in Figure 4-21shows that all of the samples possess a clear phosphorus resonance. This suggests that the water soluble phosphotungstic acid is washed out during the purification process in both Nafion composites, with and without SiO_2. This observation is consistent with those reported in literature [11, 12].

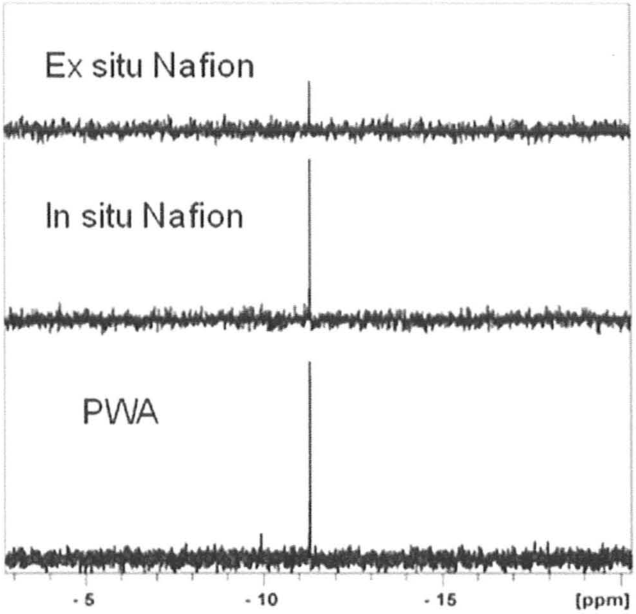

Figure 4-21 ^{31}P solution state NMR for waste water which is used to purify, *in-situ* and *ex-situ* Nafion composites and phosphotungstic acid solution, ns=128, pulse length=12.5 μs, power level=-0.5 dB, delay time=2 s.

4.3.4 PWA/SiO_2-butanol Particles and Nafion Membrane Composites

4.3.4.1 PWA/SiO_2-butanol Particles

Figure 4-22 shows ^1H spectra of the PWA/ SiO_2-butanol particles and pure SiO_2 dried at 100 °C and 200 °C, respectively. Figure 4-22 (a) and Figure 4-22 (b) reveal an identical proton resonance at 4.6 ppm, thus indicating good thermal stability of the proton. On the other hand, the 4.6 ppm peak is not observed in the spectra of Figure 4-22(c) and (d). This is evidence that the peak is not from physisorbed water from SiO_2 surface because 170 °C removes water from the SiO_2 surface [13, 14]. Therefore, the new proton environment is in the PWA/ SiO_2-butanol. The thermally stable protons (4.6 ppm) show mobility via their absence in the DQF NMR spectrum in Figure 4-23.

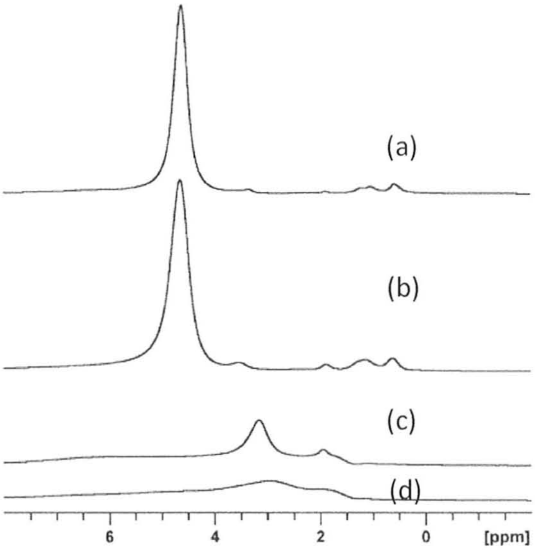

Figure 4-22 ^1H MAS NMR of PWA/SiO_2- but Nafion and SiO_2 dried at 100 °C and 200 °C, MAS=25 kHz, ns=32, pulse length=2.5 μs, power level=6.6 dB, delay time=2 s.

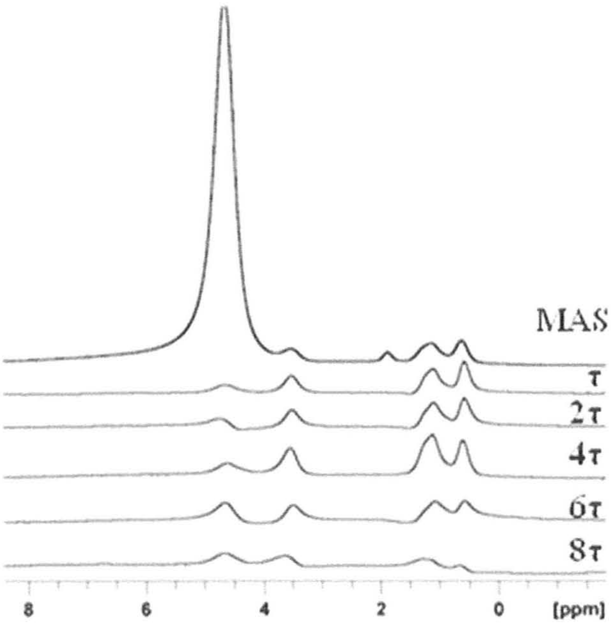

Figure 4-23 ^{1}H MAS NMR and ^{1}H MAS DOF NMR spectra of Nafion/PWA SiO_2-butanol, τ indicate the number of rotor periods of recoupling time, MAS=25 kHz, ns=32, pulse length=2.5 μs, power level=6.6 dB, delay time=2 s.

4.3.4.2 Nafion/ PWA SiO_2–butanol membrane

Figure 4-24 shows the ^{1}H MAS NMR of PWA SiO_2–butanol powder and the Nafion which contains 50% of this powder before and after the purification process. In Figure 4-24, the peak revealed at 4.6 ppm from *ex-situ* PWA SiO_2–butanol powders is attributed to the PWA SiO_2 particles. After loading this powder into Nafion by mixing the powder and Nafion solution directly, two peaks appear in the spectrum of non-purified sample at 6.8 ppm and 4.6 ppm in Figure 4-24 (b). The former peak belongs to Nafion-H while the latter peak is assigned to protons from PWA SiO_2 particles. In comparison, after purification, the two peaks are retained as seen in Figure 4-24 (c). It is indicative of the absence of changes to the proton environment following purification.

The proton from PWA SiO_2 remains after Nafion purification. However, the intensity change of the Nafion-H in Figures 4-24 (b) and 4-24 (c) is noticeable. Figure 4-24 (c) shows higher intensity of the Nafion proton, which is a result of the conversion of SO_3-X (X= impurities) to SO_3-H by H_2SO_4 washing. In addition, the ability of the proton from PWA SiO_2 particles to retain intensity following polar solution washing suggests that PWA particles are stably entrapped within the silica.

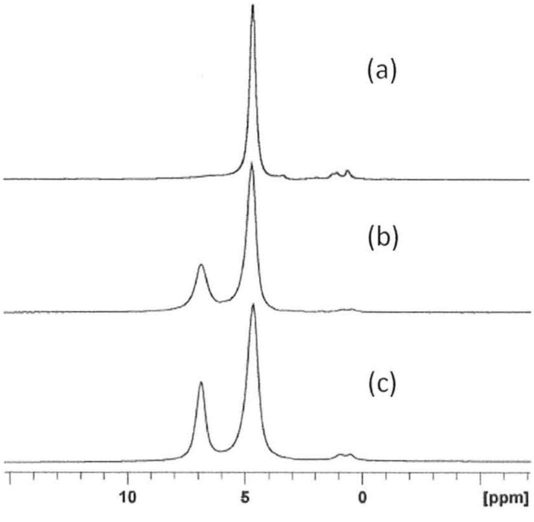

Figure 4-24 shows the ^1H MAS NMR for (a) PWA SiO_2 powder and the Nafion which contain 50% of this powder (b) before and (c) after the purification process. MAS=25 kHz, ns=32, pulse length=2.5 μs, power level=6.6 dB, delay time=2 s.

The investigation of the proton dynamics can be achieved through use of 2D EXSY. The evolution of the cross peak intensity as a function of mixing time can be used to measure the rate of the exchange between the two proton sites. The exchange between two types of protons is clearly observed in the Figure 4-25. Correlation times were determined from the buildup curve of the relative cross peak intensity as a function of mixing time between 1 ms and 100 ms. An example buildup curve of cross peak as function of mixing time at 300 K is shown in the Figure 4-26. The data was fitted using a double exponential function [15]. The proton exchange correlation time is between 0.878 and 0.613 ms over a temperature range of 300 to 330 K. The result is shown in Table 4-4.

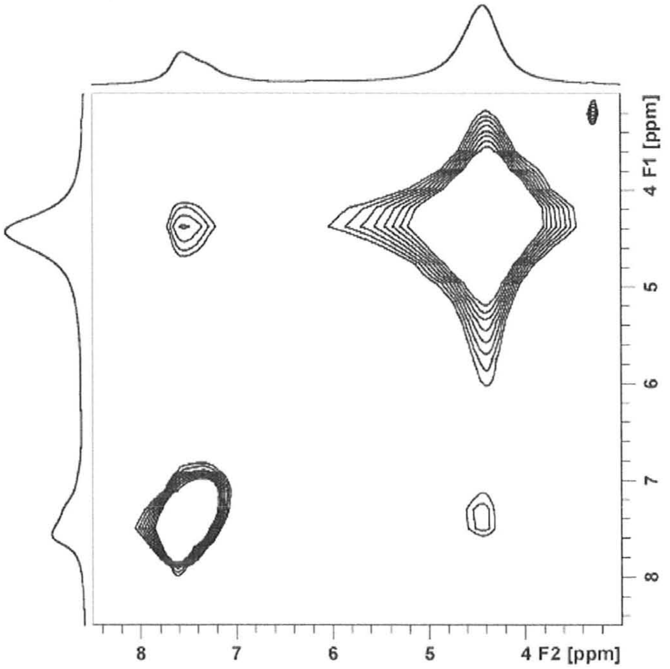

Figure 4-25 ^{1}H EXSY NMR for PWA/SiO$_2$ Nafion-butanol composites. Mixing time is 30 ms at 300 K, MAS=25 kHz.

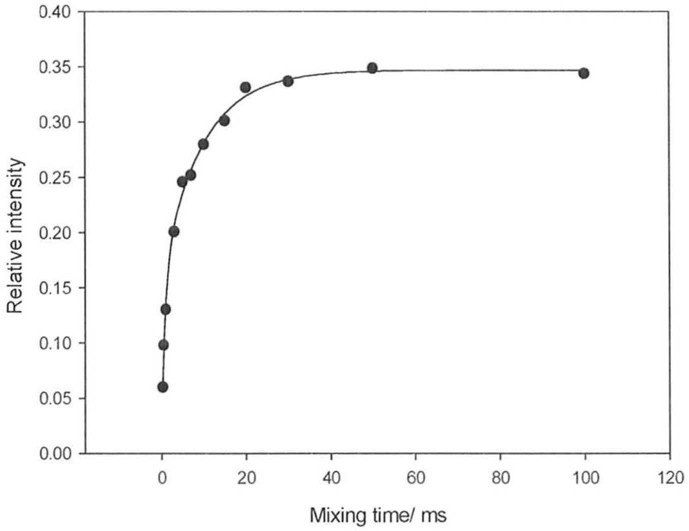

Figure 4-26 Quantization of ^{1}H EXSY data of PWA/SiO$_2$ sample: build-up curve of the integration volume of the cross peaks as a function of mixing time (1ms-100 ms at 300 K).

Table 4-4 proton exchange correlation time constant at temperature 300- 330 K

Temperature (K)	**300**	**310**	**320**	**330**
Correlation time (ms)	**0.878**	**0.781**	**0.722**	**0.613**

An activation energy of 9.5 ± 1.0 kJ/mol was determined for this exchange process from Figure 4-27. Other reports have also determined the activation energy of proton transport for Nafion and Nafion composites using solid state NMR [10, 15, 16]. The activation energy of proton transport between the Nafion and PWA SiO$_2$ proton is lower than the activation energy of dried Nafion (Ea=16.4 kJ/mol) and Nafion SiO$_2$ (Ea=12.2 kJ/mol) [16]. In this case, a new pathway of proton migration is formed in the

PWA SiO_2 Nafion, which requires less energy to achieve the proton migration under dry conditions. The movement between PWA-H and Nafion-H can be the main mechanism of proton migration in dry membranes.

.

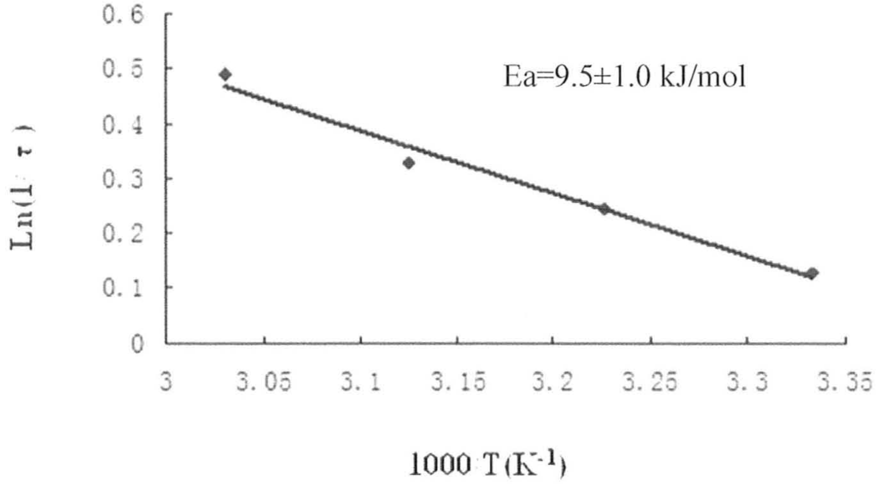

Figure 4-27. Arrhenius analysis of correlation times as function of temperature, activation energy for proton mobility by linear fitting to the Arrhenius equation

4.3.5 FTIR Measurment on the PWA SiO_2 particles and PWA SiO_2 Nafion composites

FTIR is used to confirm the presence of PWA in Nafion. For pure PWA in Figure 4-28 (a), four bands appear around 1080, 983, 893 and 809 cm^{-1} , which are assigned to stretching vibrations of P-O, W=O (terminal sharing), W-O-W (corner sharing) and W-O-W (edge sharing), respectively [17]. Figure 28 (b) is Nafion immersed in the 0.1 M PWA solution, which has clear 4 strong bands as a spectra from pure PWA sample. However, the intensity of the four characteristic bands deacreases fom the spectrum Figure 28 (c) and (d) where the Nafion was immersed in lower concertration PWA (0.01 M and 0.001M).

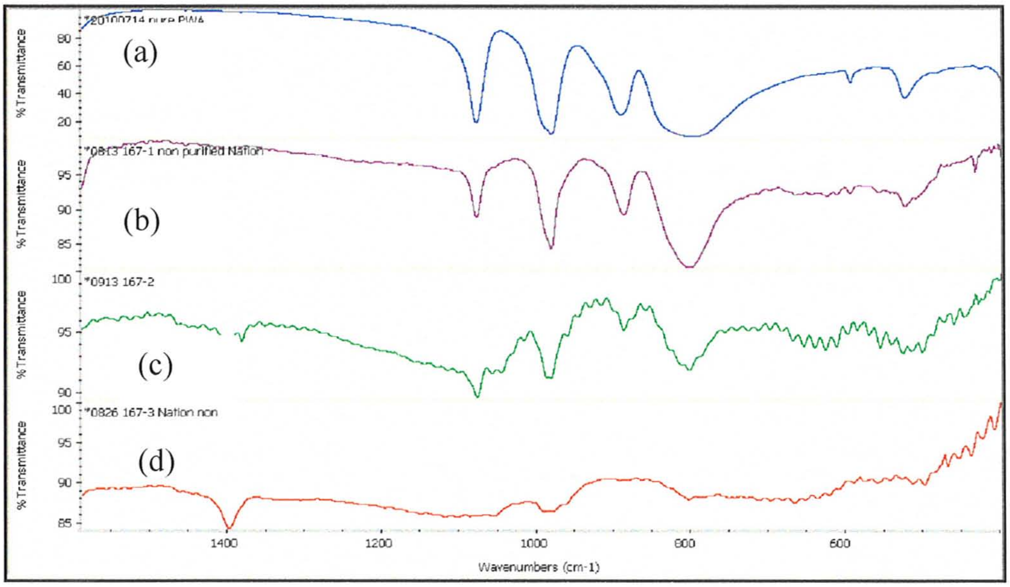

Figure 4-28 FTIR (a) pure PWA (b) Nafion 112 (0.1M PWA) (c) Nafion 112 (0.01M PWA) (d) Nafion 112 (0.001M PWA)

The existence of PWA in the PWA SiO_2 or PWA SiO_2 Nafion can be affirmed using FTIR. Figure 4-29 represents the FTIR spectra for SiO_2, pure PWA and *ex-situ* silica supported PWA particle with different TEOS/ PWA ratio. In Figure 4-29 (a), the extra two bands around 1110 and 806 cm^{-1} represent Si-O vibrations in the silica-supported PWA particle. For pure PWA in Figure 4-29(b), four bands appear around 1080, 983, 893 and 809 cm^{-1}. Figures 4-28 (c, d, e and f) are *ex-situ* silica supported PWA particle with low TEOS/ PWA ratio (40 and 80) before and after the purification process. In Figure 4-29 (c and e), all the characteristic peaks appear in the data, which can be explained as the successful loading of PWA into the membrane and very weak interactions between silica and PWA. The dramatic decrease in intensity of the P-O band accompanying the W=O band shift is observed in Figure 4-29 (d and f). This phenomenon is a result of the large amount of PWA particles leaching out from the silica particle. This type of PWA SiO_2 is not able to trap PWA with SiO_2 matrix.

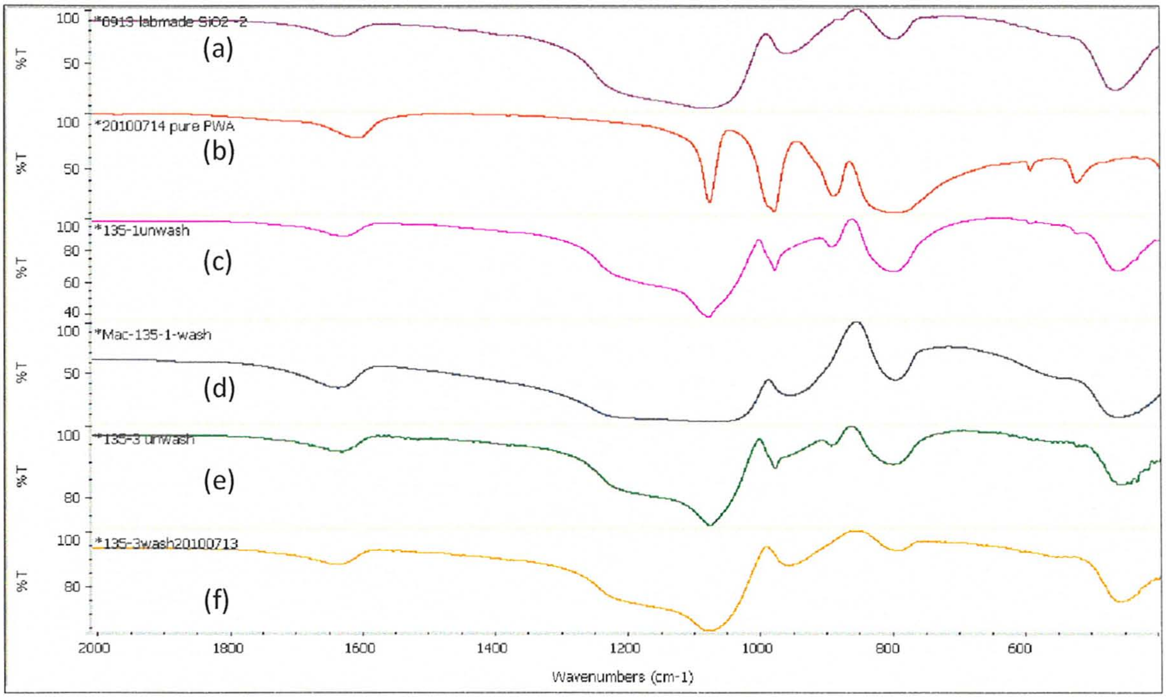

Figure 4-29 FTIR on (a) SiO_2 (b) PWA (C) PWA SiO_2 particles-40 (d) PWA SiO_2 particles -40-water wash (e) PWA SiO_2 particles-80 (f) PWA SiO_2 particles -80-water wash

In comparison, the FTIR data of *ex-situ* silica-supported PWA particle with high TEOS/PWA ratio (400) before the purification process is shown in Figures 4-30 (c). All four characteristic bands of PWA were not observed in the FTIR data. Instead, the two bands of SiO_2 appear. It means that the concentration of PWA is not large enough to be detected by FTIR. Therefore, there is no reference for PWA SiO_2 Nafion composites to confirm the presence of PWA particle after the water wash. Because there is no PWA present then no signal can be measured in FTIR. However, the presence of PWA for low ratio (TEOS/ PWA) PWA SiO_2 particles is proved by the four characteristic bands of PWA in Figure 4-30 (c).

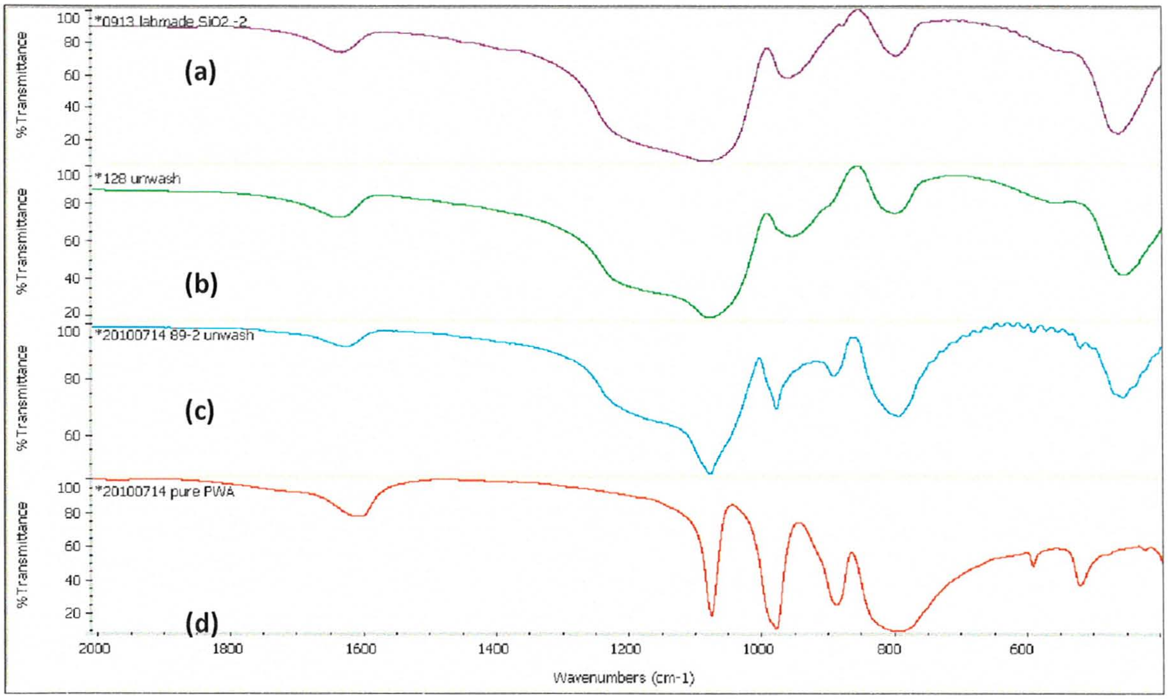

Figure 4-30 FTIR on (a) SiO_2 (b) PWA SiO_2-but particles -400 (C) PWA SiO_2 particles 32 (d) PWA

4.4 Conclusion

Proton mobility and proton conductivity strongly correspond to the amount of PWA in the Nafion membrane, which were determined using ^1H MAS NMR and impendence spectroscopy. The FTIR is used here to confirm the presence of PWA in the

Nafion and also provide the basic quantitative information of PWA content. Having high amounts of PWA in the Nafion 112 yields low activation energy and high conductivity. PWA and Nafion have two different proton environments. However, the PWA Nafion composites show only one proton resonance which implies fast rate of exchange between protons on PWA and those of Nafion itself.

The issue of PWA leaking from the membrane should be resolved by having a SiO_2 matrix. The PWA-SiO_2 matrix is made but the proton is able to retain its mobility. This is based on the results of ^1H MAS NMR under variable temperature conditions as well as the DQF NMR studies. PWA-SiO_2 particles were introduced into the Nafion membrane. Both 2D EXSY and selective inversion experiments show thermally activated chemical exchange is taking place between the two proton sites. The increasing proton mobility is due to proton exchange between the PWA and Nafion.

In *ex-situ* PWA-SiO_2 Nafion, the ^1H MAS NMR shows the resonance from the incomplete hydrolysis of TEOS which gave the higher E_a compared to the *in-situ* PWA SiO_2 Nafion samples. This result is consistent with literature from the doctoral work of Eric Ye. ^{31}P solution state NMR shows the PWA is washed out in both *in-situ* Nafion and *ex-situ* Nafion samples.

Previous work has shown that a high TEOS/PWA ratio can help PWA remain trapped in SiO_2. This information leads to the preparation of another PWA SiO_2 –butanol sample. The presence of PWA in the sample cannot be confirmed by FTIR due to the low concentration of PWA. The ^1H MAS NMR did reveal a new proton environment in this new batch PWA SiO_2-butanol particles. The proton site is thermally stable as it exists after 200 °C treatment. It also shows mobility as observed from DQF MAS NMR. The exchange reaction took place and was observed by 2D EXSY and activation is acquired from a series of EXSY as function of mixing time and temperature. The activation energy was determined as 10 kJ/mol. This result is lower than pure Nafion in dry conditions which means that a new potential pathway for protons to migrate under dry conditions has been provided.

4.5 References

1. V.Ramani, H.R.K., J. M. Fenton, , Investigation of Nafion (R)/HPA composite membranes for high temperature/low relative humidity PEMFC operation. Journal of Membrane Science, 2004. 232(1-2): p. 31.

2. M. Yamada, I.H., Heteropolyacid-Encapsulated Self-Assembled Materials for Anhydrous Proton-Conducting Electrolytes J of Physical Chemistry B, 2006. 110: p. 20486.

3. Z. G. Shao, H.X., M. Li, I. M Hsing,, Hybrid Nafion–inorganic oxides membrane doped with heteropolyacids for high temperature operation of proton exchange membrane fuel cell Solid state Ionics, 2006. 177: p. 779.

4. K. T. Adjemian , S.J.L., S. Srinivasan , J. Benziger , and A. B. Bocarsly, Silicon Oxide Nafion Composite Membranes for Proton-Exchange Membrane Fuel Cell Operation at 80-140°C. J of Electrochemical Society, 2002. 149(3): p. A256.

5. S. Uchida, K. Inumaru, and M. Misono, States and dynamic behavior of protons and water molecules in $H_3PW_{12}O_{40}$ pseudoliquid phase analyzed by solid-state MAS NMR. Journal of Physical Chemistry B, 2000. 104(34): p. 8108.

6. B. Sulikowski, J.H., A. Kubacka, K. Pamin, J. Ptaszynski, Catal Lett, 1996. 39: p. 23.

7. M.Feike, D.E.D., R. Graf, J. Gottwald, S. Hafner, H.W. Spiess, , J.Magn. Reson.A, 1996. 122: p. 214.

8. A.D. Bain, Chemical Exchange, in Modern Magentic Resonance G.A. Webb, Editor. 2006, Springer. p. 421.

9. A.D Bain, J. Magn. Reson, 1996. 118: p. 21.

10. G. Ye, C.A. Hayden, and G.R. Goward, Proton dynamics of nafion and Nafion/SiO_2 composites by solid state NMR and pulse field gradient NMR. Macromolecules, 2007. 40(5): p. 1529.

11. T. Uma, and M. Nogami, Structural and transport properties of mixed phosphotungstic acid/phosphomolybdic acid/SiO_2 glass membranes for H_2/O_2 fuel cells. Chemistry of Materials, 2007. 19(15): p. 3604.

12. A. Mahreni, A.B.M., A.A.H. Kadhum, W.R.W. Daud, S.E. Iyuke, Nafion/silicon oxide/phosphotungstic acid nanocomposite membrane with enhanced proton conductivity Journal of Membrane Science, 2009. 327: p. 32.

13. L. Hench, J.K.W., Chemical Reviews, 1990. 90: p. 33.

14. Q. Dong, R.B.M., K. Mauritz,, J. Appl. Polym. Sci., 1998. 68: p. 747.

15. G.Ye, et al., Probing proton mobility in polyvinazene and its sulfonated derivatives using H-1 solid-state NMR. Macromolecular Chemistry and Physics, 2007. 208: p. 2076-2084.

16. G. Ye, N. Janzen, and G.R. Goward, Solid-state NMR study of two classic proton conducting polymers: Nafion and sulfonated poly(ether ether ketone). Macromolecules, 2006. 39(9): p. 3283-3290.

17. C. Rochiccioli-Deltcheff, M.F., R. Frank, R. Thouvrnoc, Inorg. Chem, 1983. 22: p. 207.

Chapter 5

Summary and Outlook

Hydrogen fuel cells have become more relevant because they are environment-friendly and generate electricity with high efficiency. Unfortunately, two main disadvantages deter the commercialization of the fuel cells. These disadvantages are: degradation of the polymer electrolyte membrane and loss of conductivity at high operating temperatures. The degradation of the membrane diminishes the lifetime of the fuel cell and conductivity loss impairs the fuel cell performance. In order to resolve these issues, Nafion composites doped with CeO_2, MnO_2, Mn_2O_3, Mn_3O_4, $LiMn_2O_4$ and PWA-SiO_2 were prepared respectively. Multiple techniques (XRD, SEM-EDS, FTIR, impedance spectroscopy, solution state and solid state NMR) were utilized in this thesis to characterize these composites. Solid state nuclear resonance (SSNMR) was mainly used in this thesis as a valuable technique to investigate proton mobility in the Nafion/ metal oxide composites. The molecular dynamics in these samples were probed by ^{1}H MAS NMR variable temperature experiments, double quantum filter, and 2D exchange spectroscopy.

In order to deactivate free radicals, high loading level (> 5 wt %) of additives (CeO_2 , MnO_2, Mn_2O_3 and Mn_3O_4) were required. However, it was found that effective protection was attained in the Nafion /$LiMn_2O_4$ or $K_{0.54}Mn_2O_4$ composites at low loading levels (0.5 wt%). This result is due to the reaction between delocalized unpaired electrons and free radicals. Combining proton conductivity data with NMR data gave an overall view of proton dynamics in the Nafion/$LiMn_2O_4$ composite, revealing that $LiMn_2O_4$ does not significantly decrease Nafion conductivity.

As the lifetime of highly effective radical scavengers, such as $LiMn_2O_4$ and $K_{0.54}Mn_2O_4$, under free radical environments is currently unknown, future work can involve extending the timeframe of free radical attack and subsequently measuring the line width of samples in ^{1}H MAS NMR in order to gain insight into their lifetimes.

The second project in this thesis investigated the exchange interaction between PWA and Nafion in order to understand and enhance proton conductivity. 2D exchange spectroscopy and selective inversion experiments have shown that proton exchange interaction occurs between the sulfonic acid proton (Nafion-SO_3H) and PWA-H in PWA SiO_2 / Nafion composites (section 4.3.2). Furthermore, it was seen that the proton from sulfonic acid hops not only to adjacent sulfonic acid groups, but also to the PWA surface. Since the activation energy of proton-hopping to the PWA surface is currently unknown, the preferred proton transport pathway is not yet determined. On the other hand, a new proton environment was revealed in PWA SiO_2 Nafion butanol composites (section 4.3.4) through ^{1}H MAS NMR spectra, which is suggestive of an active proton at the PWASiO_2 surface. Variable temperature EXSY experiments have confirmed that the exchange interaction between this new proton and the sulfonic acid proton (Nafion-SO_3H) occurs with a relatively low activation energy requirement of 9.5 kJ/mol. This is evidence that a new proton transport pathway is created in the composite, leading to greater proton conductivity.

The enhancement of proton conductivity in anhydrous Nafion can be achieved by doping with phosphotungstic acid, however, the high solubility of phosphotungstic acid in water leads to its leakage from the fuel cell. Thus, SiO_2 was used as a matrix to stabilize PWA. Yet, a considerable amount of PWA was still detected by ^{31}P solution NMR in the waste water collected from the washing of PWA SiO_2 particles. Development of a suitable matrix to retain PWA continues to be a challenge in maintaining fuel cell performance. Also, selective inversion experiments performed in this thesis work have provided evidence of proton exchange occurring between PWA and Nafion. However, further work needs to be carried out to determine activation energies from these data.

In conclusion, the durability and proton conductivity of Nafion were shown to be improved by the addition of manganese/cerium oxide and PWA, respectively. Deeper understanding of proton dynamics for these Nafion-metal composites can be gained by solid state NMR. Further work to validate Nafion-metal composites will bring PEMFCs one step closer to being introduced to the consumer market, as opposed to only R&D industries.